Resistivity: Relationship to Penetrability of Concrete and Effect on Zinc Anodes in Repaired Concrete

By

Ahmed Gaber Rashwan Bediwy

A Thesis submitted to the Faculty of Graduate Studies of

The University of Manitoba

in partial fulfillment of the requirements of the degree of

Master of Science

Department of Civil Engineering

University of Manitoba

Winnipeg, MB, Canada

Abstract

Demands for using electrical resistivity techniques (surface and bulk resistivity) as an alternative to the rapid chloride penetrability test (RCPT) have been growing, for example by a number of transportation agencies in North America, to give an indication of the relative penetrability of concrete. While resistivity measurements may reflect the quality of pore structure in the cementitious matrix, their accuracy might be affected by a multitude of parameters including the concentration of ionic species in the pore solution, particularly when supplementary cementitious materials (SCMs) are incorporated in the binder. Hence, a systematic investigation on the resistivity of concrete and its corresponding physical penetrability is warranted.

Zinc sacrificial anodes are considered an effective and economical method to prevent the electrochemical corrosion of steel bars by providing cathodic current to bars, which can provide corrosion protection at low galvanic current densities in the range of 0.2 to 2 mA/m^2. Sacrificial anodes are commonly used in RC structures particularly in bridge decks to mitigate a critical phenomenon that occurs in the original concrete beside the repaired patches, which is known as the 'halo effect'. One of the key factors affecting the efficacy of zinc anodes is the resistivity of concrete or cementitious repair material in which these anodes are embedded. There is a general notion that the higher the electrical resistivity of concrete or repair material, the less likely that zinc anodes produce the target galvanic current for optimum protection of steel bars. However, no systematic data are available on the maximum allowable electrical resistivity of repair materials/concretes beyond which zinc anodes cannot properly function to prevent corrosion.

In the first part of this thesis, a tripartite relationship (nomogram) to correlate surface resistivity with penetrability (migration coefficient) and porosity of concrete using a wide range

of concrete mixtures, taking into account the effect of key mixture design parameters (water-to-binder ratio, air-entrainment, SCMs and type of cement) was established. Relationships between surface and bulk resistivity as well as migration coefficient and porosity of concrete were also introduced. In addition, a penetrability classification of concrete based on the corresponding ranges of surface resistivity, migration coefficient and porosity has been proposed. The nomogram and penetrability classification provided reasonable assessment for the condition of field cores extracted from newly constructed and aging concrete pavement.

In the second part of this thesis, the functionality of zinc anodes at mitigating patch accelerated corrosion (halo effect) in repaired concrete was explored. Concrete slabs were cast to simulate the patch repair configuration in the field, and the main parameters in this study were changing the resistivity of the repair section in the slabs (5,000, 15,000, 25,000, 50,000 and 100,000 Ω-cm), and anode spacing (25, 100, and 250 mm) inside the repair patch. Analysis of current and potential data shows a high level of effectiveness of the anodes at controlling corrosion in this slab configuration up to 52 weeks under a wetting-drying exposure.

To Mom and Dad,

I hope this achievement gets me a step closer to making you proud of me.

Acknowledgements

I would like to express my sincere gratitude and appreciation to my supervisor Dr. Mohamed T. Bassuoni, P.Eng., Associate Professor, Department of Civil Engineering, University of Manitoba, for his unremitting guidance and cordial support in all stages of this research accomplishment. I do also deeply convey my sincere thanks to him for his encouragement and help to organize my ideas and interests, and also express my deep appreciation for what I have learned from him during my study.

I highly appreciate the financial support from Natural Sciences and Engineering Research Council of Canada (NSERC), University of Manitoba, Canada and sponsorship from Vector Corrsion Technologies Ltd. The new IKO Construction Materials Testing Facility at the University of Manitoba in which these experiments were conducted has been instrumental to this research.

Many thanks to Chad Klowak, P.Eng., W.R. McQuade Heavy Structures Laboratory Manager, University of Manitoba, for his technical assistance and valuable guidance.

I would also like to thank my colleagues for their continuous support specially Ahmed Ghazy, Ahmed Hamed, Karam Mahmoud, Mohamed El Gendy and Mahmoud Amin whose comments and suggestions were remarkable.

Finally, I would like to thank my siblings “Mohamed” and “Marwa” for their invaluable efforts and support. Special thanks to my beloved wife “Esraa” for her endless support and patience throughout this significant part of our life. Thank you all, without your sincere support I would not be here to make this achievement.

Ahmed Gaber Bediwy

Table of Contents

List of Tables

List of Figures

Abbreviations/Nomenclature

$A =$ Specimen's cross-sectional area

$BR =$ Bulk resistivity

$D =$ Non-steady-state chloride migration coefficient

$L =$ Specimen's length

$MIP =$ Mercury intrusion porosimetry

$RCPT =$ Rapid chloride penetrability test

$R_i =$ Bulk Resistivity of Repair Section with an Average 5,000 Ω.cm

$R_{ii} =$ Bulk Resistivity of Repair Section with an Average 15,000 Ω.cm

$R_{iii} =$ Bulk Resistivity of Repair Section with an Average 25,000 Ω.cm

$R_{iv} =$ Bulk Resistivity of Repair Section with an Average 50,000 Ω.cm

$R_v =$ Bulk Resistivity of Repair Section with an Average 100,000 Ω.cm

$SCMs =$ Supplementary cementitious materials

$SR =$ Surface resistivity

$T =$ Average value of initial and final temperatures in the anolyte solution

$V =$ Applied voltage

$x_d =$ Average value of penetration depth

$l =$ Thickness of the specimen

$p =$ Porosity

$t =$ Time

Ω = Ohm

Chapter 1 : Introduction

1.1. Overview

Corrosion of steel reinforcement embedded in concrete structures is considered as 'bottle-neck' in the durability performance of reinforced concrete (RC) structures under harsh environments (Bentur *et al.*, 1997), resulting in significant social and economic losses. Propagation of chloride induced corrosion of embedded steel reinforcement and deterioration of concrete infrastructure by chloride-based de-icing salts are affected by a number of factors, including moisture and chloride ions ingress and pore system (total porosity, connectivity of pore structure, and concentration of ions in the pore solution) of the hydrated cement paste. The electrical resistivity of concrete is a quality control indicator, which may reflect the aforementioned factors, and it is defined as the parameter which quantifies the mobility of ionic species through concrete (Neville, 1995; Sengul, 2014). There are different methods for determining the resistivity of concrete; however, these methods may yield different values depending on the technique applied. Resistivity of concrete can be expressed in terms of surface resistivity (SR) by Wenner's probe (AASHTO TP 95-14, 2014), bulk resistivity (BR) by an alternating current (AC) set-up, or BR by a direct current (DC) set-up (ASTM C1760, 2012), similar to that of the rapid chloride penetrability test [RCPT] (ASTM C1202, 2012).

There are various techniques which have been developed to mitigate/control the damaging effect of the corrosion of steel bars in concrete such as impressed current cathodic protection (ICCP), electrochemical realkalization, and chloride extraction. Sacrificial anodes are another effective and economical method to mitigate the deleterious effects of electrochemical corrosion of steel bars, with zinc anodes being the most common type of anode used in RC

structures. Sacrificial anodes are manufactured from a metal (e.g. zinc) which has a more negative electrochemical potential than that of the steel reinforcement. Due to the difference in potential between the anode and the steel, a current will be generated and flow through the electrolyte (pore solution in the case of concrete). The typical service life of sacrificial anodes is 10 to 30 years, depending on the severity of the service conditions (chloride ions loading, environmental conditions, saturation level, etc.). Aluminum, zinc, and magnesium are the most commonly used metals as sacrificial anodes. Zinc anodes have been adopted by many transportation agencies in North America due to their high efficiency in mitigating corrosion of steel and low rate of expansion when embedded into concrete elements. Typically, they are fabricated in three different shapes a puck, cylinder and small pellet (Whitmore and Abbott, 2003). Indeed, the functionality of zinc anodes in repaired concrete can be affected by its electrical properties of concrete, i.e. resistivity.

1.2. Need for Research

The RCPT is a common quality indicator for concrete that has been extensively adopted by many transportation agencies in North America, at least for the last two decades (e.g. Wee *et al.*, 2000; Bassuoni *et al.*, 2006; Riding *et al.*, 2008). Yet, there are a number of shortcomings that have been reported for this test, such as the significant increase of temperature of concrete (Joule effect), resulting in alteration of the microstructure of concrete and overestimation of its passing charges and penetrability class (Bassuoni *et al.*, 2006; Ramezanianpour *et al.*, 2011). In addition, incorporating special constituents in concrete such as supplementary cementitious materials (SCMs) and calcium nitrite admixtures may change the ionic concentration of the pore solution, which affects the results of RCPT (electrolysis bias). Hence, there has been a considerable and growing interest to utilize the electrical resistivity of concrete to gauge its quality based on the

notion that resistivity tests are easier to perform, faster, and more economic (Ghosh and Tran, 2015). Also, resistivity tests do not distort concrete specimens, and thus they can be reused for example to monitor the change of BR or SR with time. However, similar to most testing methods of concrete, there are limitations associated with resistivity tests. In addition, neither the BR nor SR tests directly assess the physical penetration of chloride ions, for instance from de-icing salt, into concrete, which is a critical factor to evaluate the chemical and physical degradation of vital transportation facilities such as concrete bridges and pavements.

Considering the extensive use of RCPT and growing interest in employing electrical resistivity methods to assess the quality of concrete mixtures, there is a need for establishing systematic and robust relationships among such tests based on practical and reliable indicators obtained from each test. Extensive research has been carried out to establish a correlation between the SR of concrete and the passing charges obtained from RCPT (Zhao, 1998; Chini, *et al.*, 2003; Ramezanianpour *et al.*, 2011; Ghosh and Tran, 2015). On the other hand, fewer studies (e.g. Sengul, 2014) have been done to establish a relationship between the BR [AC] of concrete and passing charges from RCPT [DC]. However, such relationships are primarily based on the mobility of multi-ionic species in the pore solution, rather than only the chloride ions penetrating from the exposed surface of concrete; moreover, electrolysis bias would affect the reliability of such relationships in the sense that they may not necessarily link to the true physical features of pore structure in concrete. Besides passing charges, Bassuoni *et al.* (2006) showed that a physical penetration depth can be obtained from the RCPT, which directly shows the chloride front through concrete, alleviates the effect of multi-ionic concentration in the pore solution and better correlates to the physical characteristics of pore structure in concrete assessed by techniques such as mercury intrusion porosimetry (MIP). Hence, the motive of this part of

research mainly aims at capturing the physical characteristics of the microstructure of concrete based on a simple and robust relationship with resistivity.

Using zinc anodes in patch repairs in a RC element prevents the onset of corrosion within a surrounding area and keeps the steel in a condition of 'imperfect passivity' by providing a cathodic current to the reinforcing steel. This can be fulfilled by low densities of galvanic current in the range of 0.2 to 2 mA/m^2 (Pedeferri, 1996). However, in many field cases, deterioration induced by reinforcement corrosion has been found in the original/parent concrete in the vicinity of repaired patches sometimes within a few months of repair operations; this critical phenomenon is known as the 'incipient anode' or 'halo effect' (Page and Sergi, 2000; Christodoulou *et al.,* 2013). One of the key factors affecting the efficacy of zinc anodes is the resistivity of concrete or cementitious repair material in which these anodes are embedded. There is a general notion that the higher the electrical resistivity of concrete or repair material, the less likely that zinc anodes produce the target galvanic current for optimum protection of steel bars. As a result, low to moderate resistivity repair materials/concretes have been specified with zinc anodes. In North America, a resistivity value of less than 15,000 Ω-cm has been arbitrarily specified for repair patches of RC structures comprising zinc anodes (ACI RAP-8, 2010). However, no systematic data are available on the maximum allowable electrical resistivity of repair materials/concretes beyond which zinc anodes cannot produce the target galvanic current to prevent corrosion (Andrade and Alonso, 1996; Otieno *et al.*, 2010; Hornbostel *et al.*, 2013; Ahmed, 2014). On the other hand, low resistivity repair materials/concretes generally have higher penetrability, which may facilitate chloride ions ingress in repaired patches and consequently aggravate the process of corrosion. Therefore, exploring the effect of concrete resistivity on the efficiency of zinc anodes at mitigating patch accelerated corrosion (halo effect)

is still controversial with more research data needed in this area. Thus, the other part of this research aims at providing such data, and thus contributing to identifying the range of resistivity of repair materials/concretes within which zinc anodes retain their functionality.

1.3. Objectives

The primary objectives of this thesis are to:

- Investigate the trends and relationships among surface resistivity (SR [AC]), bulk resistivity (BR [AC]) and RCPT (physical penetration depth) for a wide range of concrete mixtures made with different water/binder, air-contents, SCMs and types of cements.
- Establish the SR measurement as a non-destructive indicator for projecting the penetrability of chloride ions into concrete and porosity of concrete, by introducing a tripartite relationship (nomogram) among these parameters.
- Explore the effect of concrete resistivity on the efficiency of zinc anodes at mitigating patch accelerated corrosion (halo effect).
- Study the influence of changing the location of the zinc anodes in the repair patch on the functionality of those anodes to alleviate the halo effect phenomenon.

1.4. Scope of Work

To achieve the aforementioned objectives, this study was split into two experimental phases. Firstly, a fundamental study was conducted to evaluate the resistivity of the concrete, and to better understand the correlation between the resistivity of the concrete and the physical characteristics of the pore structure in the cementitious matrix which facilitated the analysis of the second phase of this program. Therefore, a wide range (more than forty) concrete mixtures was prepared with various proportions of SCMs such as silica fume and fly ash (Class F) with or without the incorporation of different dosages of nanoparticles (6% nano-silica or nano-alumina)

by mass of the total binder content at different w/b ranging from 0.3 to 0.7. The tests in this part of research included RCPT, SR, BR, and MIP.

In the second phase, mini-scale slabs were cast in three batches to simulate the patch repair configuration in the field. The bottom half (chloride free concrete), and the top half was split into two equal halves: one section (old concrete: contaminated with 3% calcium chloride by mass of cement), while the other section (repair patch-chloride free) had variable resistivity. Based on the results of the first phase, five different concrete mixtures were selected to produce BR ranging between 5,000 and 100,000 Ω-cm to prepare the simulated repair section for the purpose of evaluating the functionality of zinc anodes. The assessment criteria were based on several electrical measurements such as the current density, potential, and 100 mv depolarization decay.

1.5. Thesis Structure

The thesis is divided into six chapters:

- Chapter one contains introduction, overview of electrical resistivity of concrete and sacrificial anodes, problem definition/research significance, objectives and scope of work.
- Chapter two presents literature review of electrical resistivity of concrete, including factors affecting this property, and recent advancements of research in this area. Also, this chapter comprises description of the halo effect in repaired concrete containing zinc anodes and literature on the influential factors (including resistivity of concrete) of this phenomenon.

- Chapter three describes the methodology, materials and mixtures used in the test program. It elucidates test procedures implemented in both phases, and the details of the tests conducted to monitor the behaviour of concrete.
- Chapter four presents the results and discussion for the tripartite relationship among resistivity, penetrability and porosity of concrete, including the effect of key mixture design parameters (w/b, air contents, SCMs and type of cement) on such paramters.
- Chapter five describes the test results and discussion for assessing the efficiency of zinc anodes in repaired concrete taking into account the effect of changing the resistivity of the repair section in which these anodes are embedded, as well as changing the location of the zinc anodes.
- Chapter six provides a summary of the research findings, concluding remarks based on the test results and recommendations for future research.

Chapter 2 : Literature Review

In this chapter, a review of the literature pertinent to resistivity of concrete, corrosion of steel bars embedded in concrete structures, and incipient anode is presented. The corrosion mitigation techniques are also discussed herein.

2.1. Overview

Corrosion of steel is normally a consequence of loss of passivity due to carbonation of concrete or chloride contamination. Chloride-induced corrosion of the reinforcement is considered the main deterioration cause of (RC) structures (Bentur *et al.*, 1997). Patching is a common repair technique conducted by removing the deteriorated concrete, cleaning the steel, and finally restoring the concrete integrity with a new repair material which will make the steel passive within the repair area. However, the redistribution of anodic and cathodic sites subsequent to concrete repair affects future corrosion risk (Christodoulou *et al.*, 2013). In other words, the corrosion cell moves to areas adjacent to those that have been repaired. This phenomenon is known as the incipient anode which was first introduced by Page and Treadaway (1982). Galvanic anodes have been extensively used to limit the extent of concrete replacement and to extend the service life of patch repairs to RC structures. Furthermore, concrete resistivity of the repair concrete in which those anodes are embedded is considered as one of the most important parameters that can affect the propagation of steel corrosion because it implicitly represents other parameters such as moisture and chloride ions ingress, temperature, and pore system (total porosity, connectivity of pore structure, and concentration of ions in the pore solution) of the hydrated cement paste (Hornbostel *et al.*, 2013).

2.2. Resistivity of Concrete

Corrosion of steel bars is considered one of the essential concerns in concrete durability evaluation because of the penetration of chloride ions into concrete. This single factor is the most important variable influencing the initiation and the propagation of the corrosion of steel bars embedded in concrete. Vast cracking and spalling of concrete always correspond to corrosion, which in turn will accelerate the deterioration of bridge decks leading to expensive repairs. There are several testing procedures to assess/measure the chloride ion penetration; however, the challenge is to measure this variable with a simple and quick method (Ryan *et al.,* 2014). The most direct method to measure chloride penetration is chloride/salt-ponding test (ASTM C1543, 2010); however, the testing period for specimens requires at least 3 months. Additionally, it may not allow sufficient time for low penetrability concretes (Savas, 1999). Consequently, many transportation agencies have adopted an alternative method to assess the penetrability of concrete which is referred to as the rapid chloride ion penetration (RCP) test as detailed in ASTM C1202 (ASTM C1202, 2012).

The chloride ions can be transported inside the concrete via three ways: hydrostatic pressure, capillary suction, and diffusion. The most common mechanism is through diffusion, which is the main concern when assessing chloride ion penetration risk. Diffusion takes place when the concentration gradient is presented. For bridge decks (real situation), chloride ions exists in the de-icing salts used during winter season, and it dissolves in the melted snow diffusing through the concrete deck surface leading to the steel corrosion. In the RCP test, a constant voltage is applied across a concrete specimen between the two test compartments to simulate the diffusion mechanism, and the amount of charge that passes through the specimen is measured. However, this test has several shortcomings where it is time-consuming and laborious.

In addition, the results obtained from RCPT may be biased when the chemical and mineral admixtures are presented in the cementitious matrix such as silica fume and calcium nitrate corrosion inhibitors (CNI) (Bassuoni *et al.,* 2006). In addition, the current passed is related to all ions in the pore solution not only the chloride ions (Stanish *et al.,* 1997). Thus, it is not accurate to use the passing charge as specified in ASTM C1202 to assess the rapid chloride penetrability of concrete with supplementary cementitious materials (SCMs). Finally, the temperature also increases in case of using low quality concrete leading to a higher coulomb value (Stanish *et al.,* 2000). Consequently, an alternative approach has been proposed by Bassuoni *et al.* (2006) to assess the actual chloride front through concrete (discussed in more details in Chapter three).

As a consequence, the research area has focused on using the electrical resistivity of concrete as an alternative to the RCPT (as an indicator of chloride ion penetrability). The electrical resistivity (ρ) [Ω-m] of a material describes the resistance against the flow of an electrical current. It is the ratio between applied voltage and resulting current multiplied by a cell constant and is thus a geometry independent property. The inverse of resistivity is conductivity (σ). The electrical resistivity of concrete may vary over a wide range, from 10 to 10^5 Ω m, and it is influenced by the moisture content of the concrete environment and the composition of the material (Whiting and Nagi, 2003). The resistivity of concrete has long been a concern because of its relation to the risk of corrosion of reinforcing steel. As Polder (2001) explains: Concrete ability to oppose an electric current, or resistivity, affects both the "initiation period (chloride penetration) and the propagation period (corrosion rate)". Electrical resistivity is non-invasive and non-destructive and can evaluate microstructure of concrete. It can be related to the volume fraction of the pores and conductivity of the pore solution and in addition, it can be utilized to predict the diffusion coefficients of chloride ions and water penetrability (Christensen *et al.,*

1994). Resistivity can be used for different purposes, one of which is condition surveying of concrete structures (Sengul and Gjørv, 2009; Hornbostel *et al.*, 2013; Andrade *et al.*, 2013). Evaluating concrete properties is possible with electrical resistivity (Chung, 2003; Ferreira and Jalali, 2010; Wanga *et al.*, 2013). In general, the resistivity of concrete can be used as an index for the water content and the connectivity of the micro-pores inside concrete and thus it can be also used as an index for the quality and durability of concrete. Resistivity for concrete with looser microstructure is generally lower. That means the chloride ion may penetrate faster into a concrete with lower resistivity and consequently the corrosion may happen more easily (Polder, 2001).

Numerous configurations have been proposed to evaluate the electrical resistivity of concrete. In general, metal electrodes are responsible to connect the circuit with the concrete. The electrical resistivity of concrete is determined with the aid of an equivalent circuit model. Based on such model, two different methods have been developed such as two-point uniaxial (bulk resistivity [BR]) and four-point (surface resistivity [SR]; Wenner probe) techniques, as shown in Figure 2.1 and 2.2, respectively. The uniaxial technique is a simple yet reliable method to measure the BR, and also this test takes only few seconds. However, it cannot be applied to field evaluation, as it requires coring the existing structure to take the samples. On the other hand, four electrodes are employed to measure the SR of concrete. One widely accepted method is the Wenner probe where the four electrodes are located in a straight line and equally spaced. The SR method is quick, non-destructive, simple, and it is suitable for on-site evaluation of concrete (Layssi *et al.*, 2015)

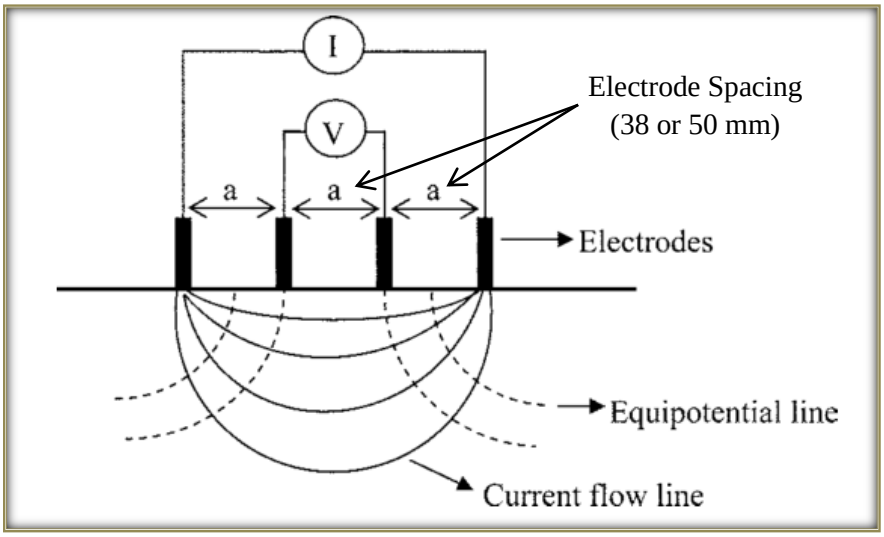

Figure 2.1: Schematic representation of four-electrode resistivity test (after Sengul and Gjørv, 2009).

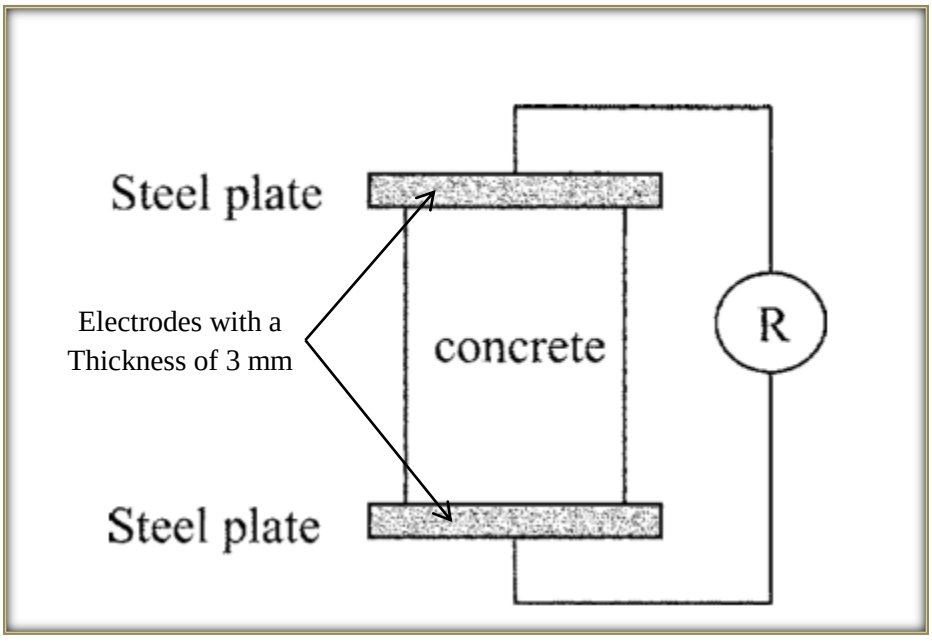

Figure 2.2: Schematic representation of two-electrode bulk test (after Sengul and Gjørv, 2009).

2.2.1. Factors affecting resistivity of concrete

The inherent electrical resistivity of concrete is affected by several factors such as:

- The degree of saturation has a direct effect on the resistivity of concrete as it would change the amount of fluid in pore network. Therefore, it is recommended to use a consistent curing method and to ensure that the test specimens are in saturated surface wet during testing.
- The ambient temperature around the specimens shall be maintained in the range of 20 to 25°C. The movement of free ions within the pore solution controls the electric current flows in concrete. Thus, increasing the temperature increases ionic mobility which, in turn, increases the electrical conductance and decreases the electrical resistivity (Zaccardi *et al.,* 2009)
- For constant moisture content, the resistivity is increased by a lower water-to-cementitious materials ratio (w/cm) and vice versa. The electrical resistivity decreases as a result of high amount of pore water (wet concrete) and wider pores as in the case of high w/cm.
- The presence of steel reinforcement embedded in concrete is not a situation that can be avoided in the field. Gowers and Millard (1999) reported that the errors in measurement were only significant if the probe positioning was directly over a reinforcing bar. If the reading was taken remote from a parallel bar, the error was not significant.
- The presence of chlorides in a concrete specimen encourages the concrete to retain water. Therefore, chlorides are wrongly considered to reduce concrete resistivity.

2.2.2. Research on resistivity of concrete

A summary of the research that has been carried out in the area of the electrical resistivity of concrete is presented in this section.

Zhao *et al.* (1998) studied the electrical conductance of various concrete mixtures with alternating current to reflect its permeability. The authors established a relationship between the passing charges obtained from ASTM C1202 and the electrical conductance for such mixtures, with the coefficient of 0.98. Furthermore, Sengul (2014) proposed the same relationship on the basis of the chloride diffusivity rather than the passing charge using twenty nine concrete mixtures. Both experimental results indicated a strong relationship between the two datasets, and a classification of chloride resistance based on resistivity is created. diffusivities using data from another work. However, Ryan et al. (2014) determined the same relationship based on cylinders collected from concrete bridge deck being constructed (Tennessee bridge). Moreover, Sengul and Ryan validated their relationship by comparing the aforementioned trends based on resistivity with other data extracted from another work

Ramezanianpour *et al.* (2011) proposed a relationship between concrete resistivity and several parameters such as water penetration specified by BS EN-12390-8 (2000), passing charges specified by ASTM C1202, and compressive strength based on fifty seven concrete mixtures. Also, two models were proposed to correlate SR with passing charges with a coefficient of determination (R^2) of 0.9 and 0.83, respectively. In addition, Ghosh and Tran (2015) tested the SR and BR of concrete cylinders for twenty three concrete mixtures at different testing ages, taking into account several parameters namely geometric size, probe spacing, replacement levels of silica fume and metakaolin in ternary based cementitious mixtures on the

SR of concrete. Furthermore, a new chloride ion permeability classification based on electrical resistivity has been suggested.

In 2002, the Florida Department of Transportation (FDOT) started to correlate results from both RCP and SR tests for more than 500 sample sets, and the two tests revealed a strong relationship with a coefficient of determination (R^2) of 0.95 for concrete specimens tested at 28 days. In 2007, the RCP test was eliminated from FDOT specification (FM 578, 2004) and replaced with the SR test. In addition, a rating table was created to clarify the interpretation of the surface resistivity based on the previous ranges provided in ASTM C1202 (2012).

Sengul and Gjørv (2009) investigated the effect of embedded steel bars on electrical surface resistivity for concrete structures. The surface resistivity was measured in two different directions relative to the embedded steel. The authors investigated the influence of cover thickness and curing condition on the resistivity. All measurements should be carried out as far as possible from all embedded steel, and if such situation cannot be avoided for field measurement, the electrode spacing should be kept small relative to the concrete cover depth.

2.3. Corrosion of Steel Bars Embedded in Concrete Structures

Reinforced concrete is considered as a relatively modern construction material which has been improved and utilized extensively only in the 20th century. The combination of reinforcing steel and concrete is known as an optimal scenario to enhance the mechanical performance as well as the long-term durability. Such combination should be highly durable, because the concrete cover provides a thick barrier to protect steel bars under harsh environment, and render the steel function effectively.

In spite of the theory regarding the long-term performance of RC structures, in the last three decades corrosion has become a significant durability problem in mild and severe climatic conditions, as shown in Figure 2.3. In the past, the researchers mainly focused on the performance of the concrete itself, e.g. resistance of concrete to sulphate attack typical of marine structures. However, it seems that the corrosion usually occurs before any noticeable sulphate attack, as corrosion is considered as 'bottle-neck' in the durability performance of RC structures at specific environment (Bentur *et al.*, 1997). However, chloride-corrosion of steel bars is the most common cause of the degradation of RC in North America. De-icing salts is frequently applied to remove snow/ice from roads surface during winter to accomplish safety and functionality goals. De-icing salts can penetrate into the concrete and breakdown of the passive film on the steel; consequently, initiating the corrosion. Some estimates refer that it would cost $78 billion to restore all structurally deficient bridges in the U.S. alone, where corrosion is a significant cause of this deterioration (Whitmore and Abbott, 2003).

Generally, the mechanism of the corrosion of steel involves the removal of iron atoms (Fe^{2+}) by an electrochemical reaction, and it is dissolved in the surrounding pore solution. As a result of this disintegration process, the cross-section of the steel bar will be reduced and

becomes smaller. The mechanism of the chloride induced corrosion will be discussed in detail in the next section.

Figure 2.3: Corrosion in a bridge structure.

The passive layer (protective layer) is self-formed on the outer surface of the steel bars during the hydration of the cement (Fe_2O_3), as shown in Figure 2.4. As long as the oxide film is presented, the steel remains intact; however, once the concentration of the chloride inside the concrete reaches a threshold limit, the oxide film on the surface of the steel will be destroyed. In addition, the presence of water and oxygen will stimulate the corrosion to take place. It also worth mentioning that not only the chlorides that can destroy the passivation layer around the steel but also the carbon dioxide has the capability to break down such layer.

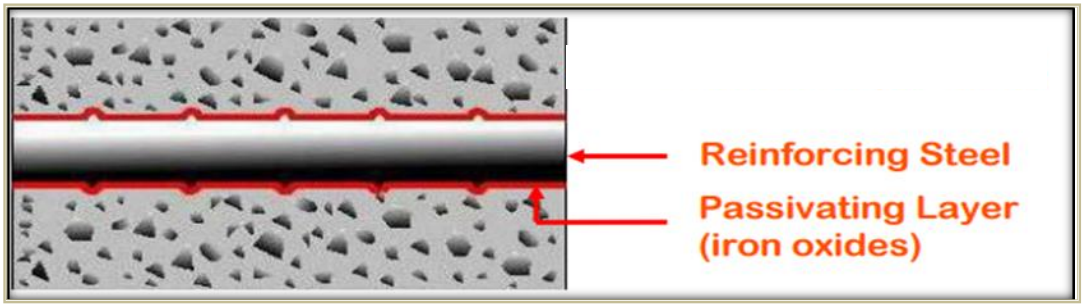

Figure 2.4: Iron oxide film (after Bargaheiser and Butalia, 2007).

There are many types of corrosion that can take place due to different reasons/sources will be illustrated as follows:

- ***Galvanic corrosion***: the process of the corrosion of steel usually involves two chemical reactions that take place at two different locations on the steel surface in addition to an electric current that should flow in a closed loop between the two locations. This process is similar to what happen in the ordinary dry battery. Technically, such batteries are described as "galvanic cell", so the corrosion process is sometimes called "galvanic corrosion". The two electrochemical reactions are known as "anodic" and "cathodic" reactions (see Equation 2.1 and 2.2), respectively,

and the areas on which they take place are called "anodic" and "cathodic" areas. Once a difference in the electrical potential along the steel occurs, an electrochemical cell will be created. Anodic and cathodic zones which are connected by the electrolyte in the pores of the cement paste will be formed. The atoms of iron are oxidized to ferrous ions (Fe^{2+}) at the anode leading to an increase in the concentration of the electrons, which will, in turn, increase the electrical potential up. Such electrons will start to move through the steel to the lower potential zone (cathodic). In addition, the electrons will merge with the oxygen molecules and the water in the pores at the cathode area forming hydroxide ions (OH^-). When the ferrous ions (Fe^{2+}) meet up with the hydroxide ions (OH^-), they will react together to form $Fe(OH)_2$ which is a metastable compound need to be stable. This will be obtained by reacting with additional oxygen to form insoluble product (rust). The rust always accompanied by distinctive color such as red rust (Fe_2O_3) black rust (Fe_3O_4).

Anodic reactions $(Eq. 2.1)$

$$Fe \rightarrow Fe^{2+} + 2e^-$$

$$Fe^{2+} + 2OH^- \rightarrow Fe(OH)_2$$

Cathodic reactions $(Eq. 2.2)$

$$4e^- + O_2 + 2H_2O \rightarrow 4OH^-$$

- ***Concentration cell corrosion***: the corrosion can also take place if there are differences in the local environment along the surface of the steel. Furthermore, this type of corrosion always associated with submerged structures, whereas the concentration of dissolved oxygen on the surface of the steel is increased, this zone

will behave as a cathode, and the zone with less dissolved oxygen will subsequently behave as an anode (Bentur *et al.*, 1997). Consequently, such difference will initiate the onset of the corrosion. Also, this type of corrosion is termed as "aeration cell corrosion".

- ***Micro and Macro cell***: Micro cell corrosion or can be also termed as "galvanic corrosion". Micro cell is the term given to a specific situation: when the anodic and cathodic reactions take place on the surface of the same bar, as illustrated in Figure 2.5. That's why this type occurs only in the laboratory specimens which are reinforced with a single steel bar or can occur in real structures with a single rebar mat (Hansson *et al.*, 2006). While, macro cell corrosion can occur when the corroding bars is connected with another bar which is passive or has lower corrosion rate, either because of its different composition or different environment. An example of the former situation is ordinary black steel in chloride-contaminated concrete and in contact with stainless steel; the later situation can occur when a top steel mat in chloride-contaminated concrete is coupled to a bottom steel mat in chloride-free concrete, as illustrated in Figure 2.6.

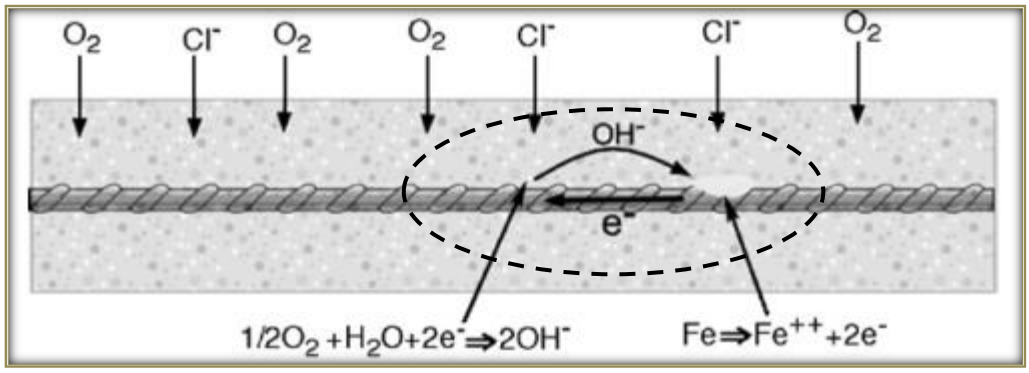

Figure 2.5: Schematic illustration of microcell corrosion (after Hansson *et al.*, 2006).

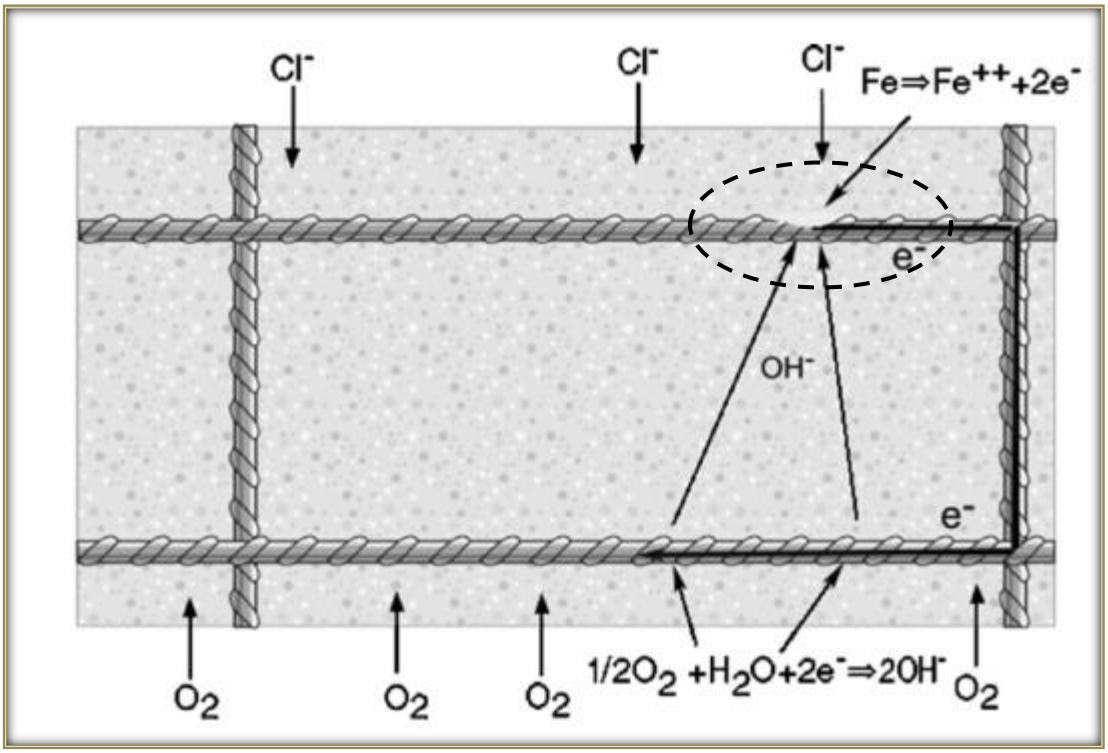

Figure 2.6: Schematic illustration of macro corrosion (after Hansson *et al.*, 2006).

- ***Pitting corrosion***: pitting corrosion is a localized form of corrosion due to localized breakdown of the passive films on the surface of the steel bars which can lead to accelerated failure of structures (Frankel, 1998), as shown in Figure 2.7. Pitting corrosion in more deleterious compared to uniform/ordinary corrosion, as it is difficult to predict and to design against. Whereas a small narrow pit can lead to an entire failure of any engineering system. The two possibilities to initiate pitting corrosion: localized damage in the protective oxide film due to the high concentration of chloride (as in sea water), or localized damage in the protective coating.

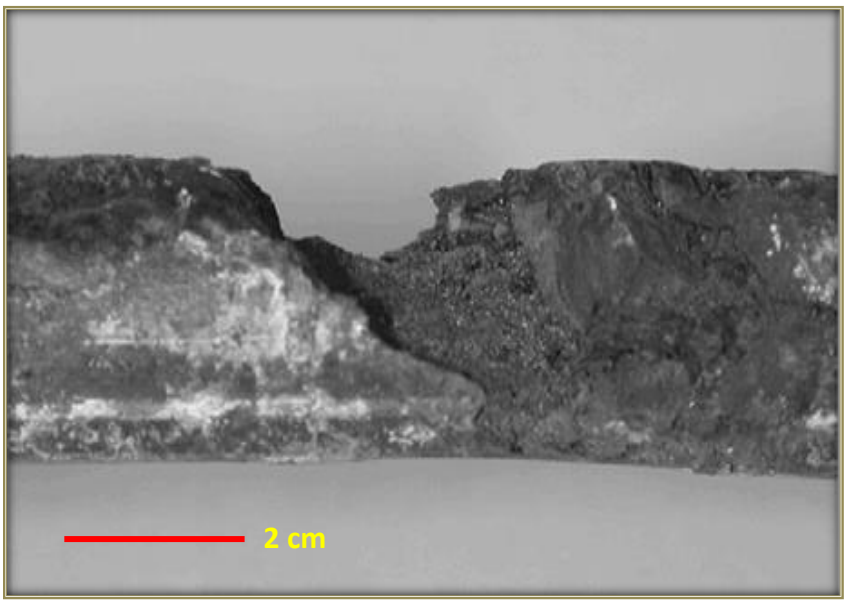

Figure 2.7: Pitting corrosion (localized form of corrosion).

2.4. Incipient Anode (Halo Effect)

This phenomenon occurs when the patching repair technique is carried out at any concrete structure. Such technique is a common repair approach which involves the removal of the chloride-contaminated concrete by any device (Jack hammer), cleaning the exposed steel, and reinstatement the concrete profile with a new fresh concrete. In addition, in many situations deterioration induced by corrosion has been noticed in the original/parent concrete adjacent to the repair patch, sometimes it happens within few months. Also, it is worth to mention that the macro cell activity causes the incipient anode phenomenon (Page and Treadaway, 1982).

The boundary line between the parent/original (chloride-contaminated) patch and the new repair (chloride-free) patch is considered as the most susceptible zone to initiate/provoke such phenomenon, as shown in Figure 2.8(a-b) (Page and Sergi, 2000; Christodoulou *et al.*, 2013). When the most anodic regions (corroded regions; Figure 2.8a) of the reinforcement are replaced

with passive steel in the repaired zones, the probability of initiating/stimulating corrosion is high because of the potential difference between the two zones (Figure 2.8b). The corrosion in such situation always takes place around the perimeter of the repair patch. Therefore, this phenomenon is known as "ring anode".

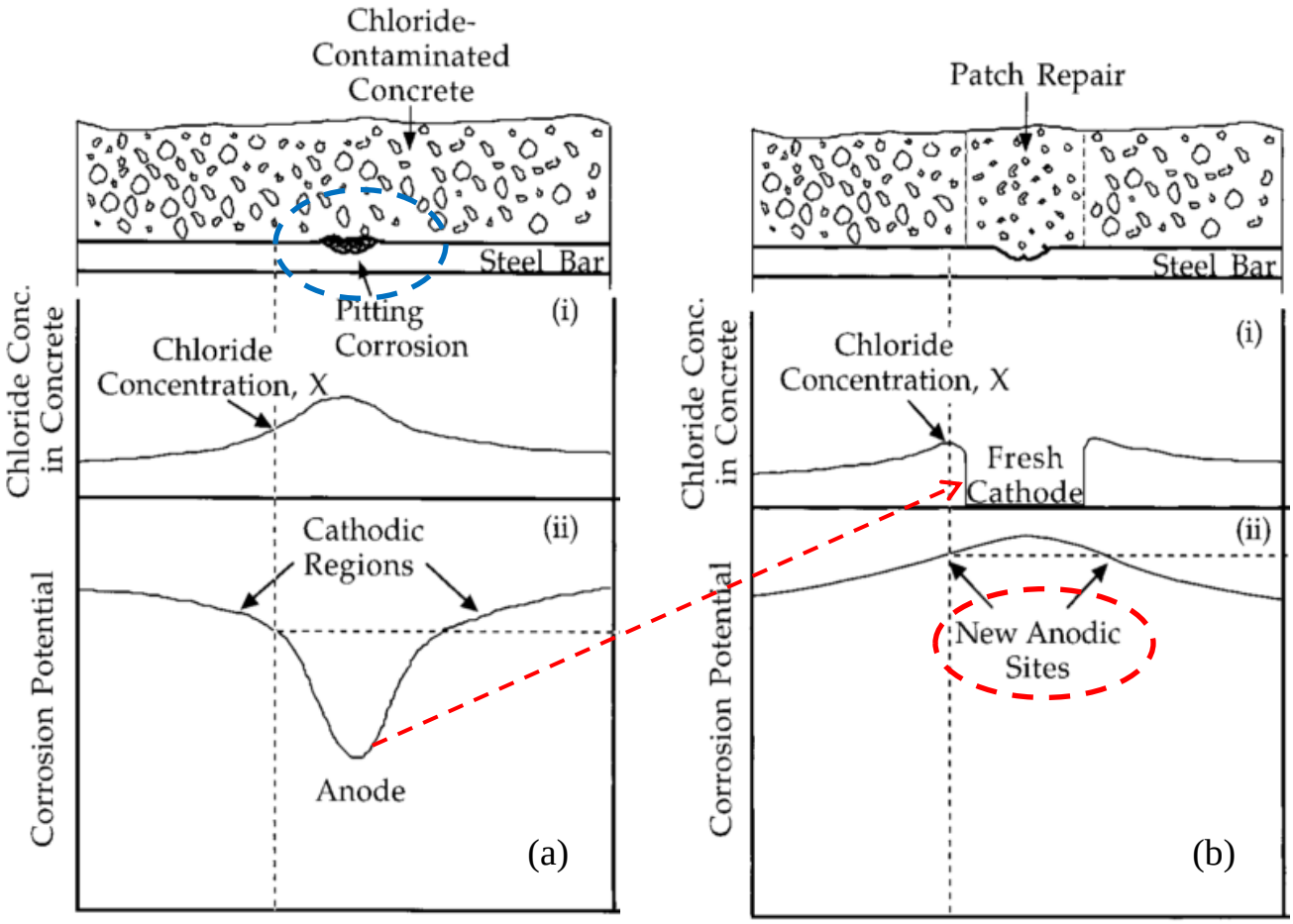

Figure 2.8: (a) condition of localized corrosion of steel in chloride-contaminated concrete (circled in blue) as reflect by the anode in the potential profile, and (b) conditions for incipient anode formation as reflected by the new anodic sites in the potential profile (circled in red) (after Page and Sergi, 2000).

2.5. Corrosion Mitigation Techniques

The need to rehabilitate RC structures has been extensively increased due to the widespread of the factors initiating/provoking corrosion of steel such as de-icing chemicals and marine-sourced chloride. The removal of the old chloride-contaminated concrete and restoring its integrity with a new concrete is considered the traditional method of repair. However, this technique does not satisfy the long-term durability needs. Consequently, electrochemical mitigation techniques are recently applied in order to avoid corrosion: by stopping it, by limiting it within reasonable/acceptable ranges or preventing it. Such techniques depend on directing the steel potential in the cathodic direction by applying direct current flow through concrete to the reinforcement. There are many techniques adopted to suppress corrosion of steel such as cathodic protection, cathodic prevention electrochemical chloride removal, and electrochemical realkalization.

2.5.1. Cathodic protection and cathodic prevention

The theory, which the cathodic protection is based on, is to shift the potential of the steel to values more negative than the corrosion value, which in turn will reduce the macrocell activity on its surface. Cathodic protection is applied to concrete structures which are already affected by corrosion. On the other hand, cathodic prevention is carried out by polarizing (directing) the rebar from the beginning to the cathodic direction and throughout the entire service life of the structure. The threshold chloride content is increased with respect to non-polarized structures so that it will not be reached during the service life of the structure. This can be fulfilled with low cathodic current density (Pedeferri, 1996). Pedeferri's diagram (1996) briefly and simply summarizes the theory behind the cathodic protection and cathodic prevention, as shown in Fig. 2.9(a and b). This figure shows the different domains/zones of potential and chloride contents

where corrosion can initiate and propagate. The boundaries between these zones are indicative, as they depend on several factors such as pH and temperature. Zone A (corrosion zone) indicates the conditions that cause initiation and stable propagation of corrosion. Zone B (imperfect passivity zone) indicates the conditions that do not allow the initiation of new pits but they do allow the propagation of pre-existing ones. Zone C (perfect passivity zone) represents the conditions that do not allow either the initiation or the propagation of corrosion. The path of the potential of steel reinforcement exposed to chlorides and then protected by a cathodic protection system (see Fig. 2.9a). The initial point 1 represents the condition at which the chloride content is nil and the steel is passive. When the chloride content is increased by time, the working point shifts to point 2 (within the corrosion region). Applying cathodic protections leads to point 3 so that the passivity is restored or to point 4 without fully restoring passivity. However, in all cases, the corrosion rate is reduced. On the other hand, the typical path for cathodic prevention is (1-5-6), as shown in Fig. 2.9b. Current densities in the range of 0.2-2 mA/m^2 results in a decrease in the potential of at least 100-200 mV from the beginning, which in turn increases the critical chloride content that is expected to be sufficient to avoid corrosion initiation throughout the entire service life.

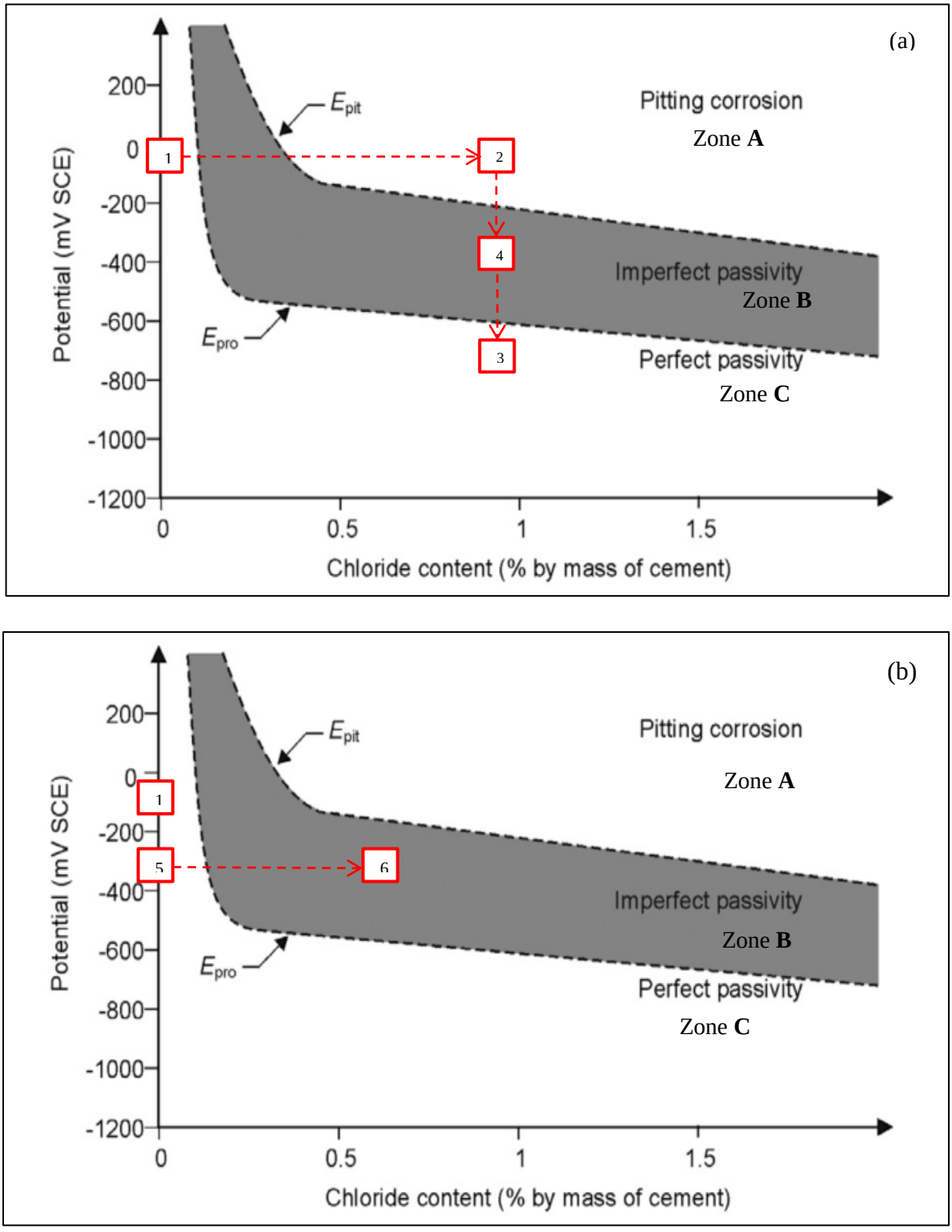

Figure 2.9: Schematic diagram of (a) cathodic protection, and (b) cathodic prevention (after pedeferri, 1996).

2.5.2. Types of corrosion mitigation systems

These are several types of corrosion mitigation techniques adopted by many agencies in North America such as:

- ***Sacrificial anodes***: Sacrificial anode is one of the efficient techniques adopted to mitigate corrosion which already took place or will occur in the near future. In general, sacrificial anode is manufactured from a metal which has an electrochemical potential more negative than the steel reinforcement in the galvanic series. Because of the difference in the potential between the sacrificial anode and the steel, a current will be generated and flow through the concrete from the anode to the steel in the sense that the anode will sacrifice itself instead of the steel (Shi *et al.,* 2011). Implementing sacrificial anodes in the repair applications for concrete structures has been widely adopted with respect to the other techniques due to many advantages. These advantages include 1) there is no need to external power source to generate current, and 2) the installment process of the sacrificial anodes in the concrete is very simple. Also, the output current from the anodes is low with respect to any other techniques which will lead to reduce the risk of hydrogen embrittlement of the steel. However, the lifespan of the sacrificial anode cannot be expected.

  The anodes are manufactured in three different shapes, a puck, a cylinder and small pellet. Aluminum, zinc, and magnesium are the most commonly used metals as sacrificial anodes. Zinc anodes have been adopted by many transportation agencies in North America due to their high efficiency in mitigating corrosion of steel and low rate of expansion when embedded into concrete elements (Wilson *et al.,* 2013; Volkan, 2013). In addition, the native potential of the zinc anode is not sufficient to generate hydrogen

atoms which, in turn, make it suitable for the prestressed concrete applications. To keep the zinc from passivating over time, zinc anode must be located in high alkalinity environment (Whitmore and ball, 2005). Therefore, zinc anode is encapsulated in precast mortar saturated with lithium hydroxide (LIOH) which will maintain a high pH (>14) around the zinc, as shown in Fig. 2.10.

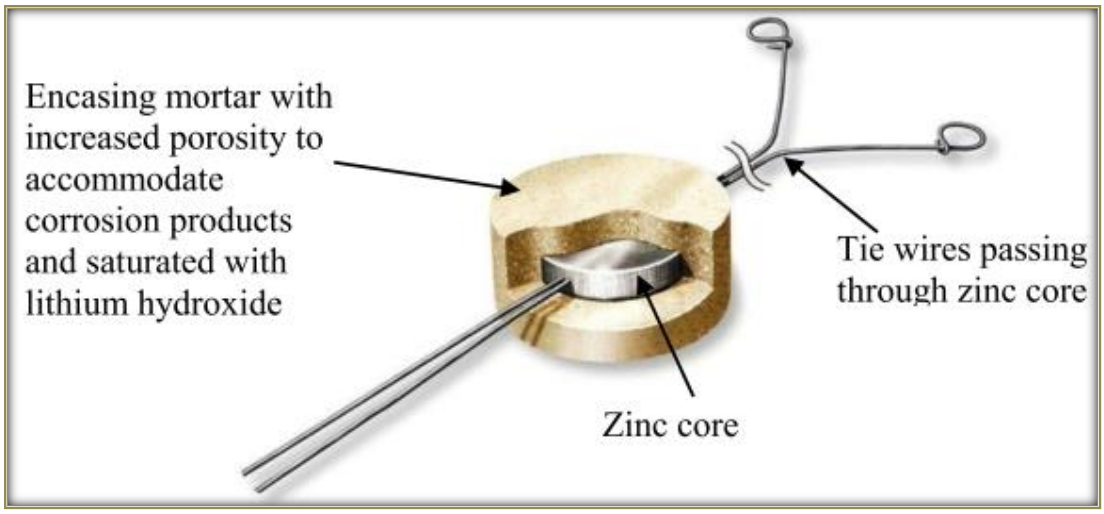

Figure 2.10: Cutaway of zinc anode for concrete repair (after Whitmore and ball, 2009).

- ***Impressed current***: This method depends on supplying a current from an external source to overcome the on-going corrosion current in the structure. Impressed current system consists of anode system, reinforcing steel, reference electrode and a direct current (DC) power supply. Such system can be installed on the surface of the concrete or in grooves or slots cut into the surface of the concrete. A permanent current is generated by a rectifier when the negative and the positive terminals are connected to the anode and the steel, respectively, as shown in Fig. 2.11.

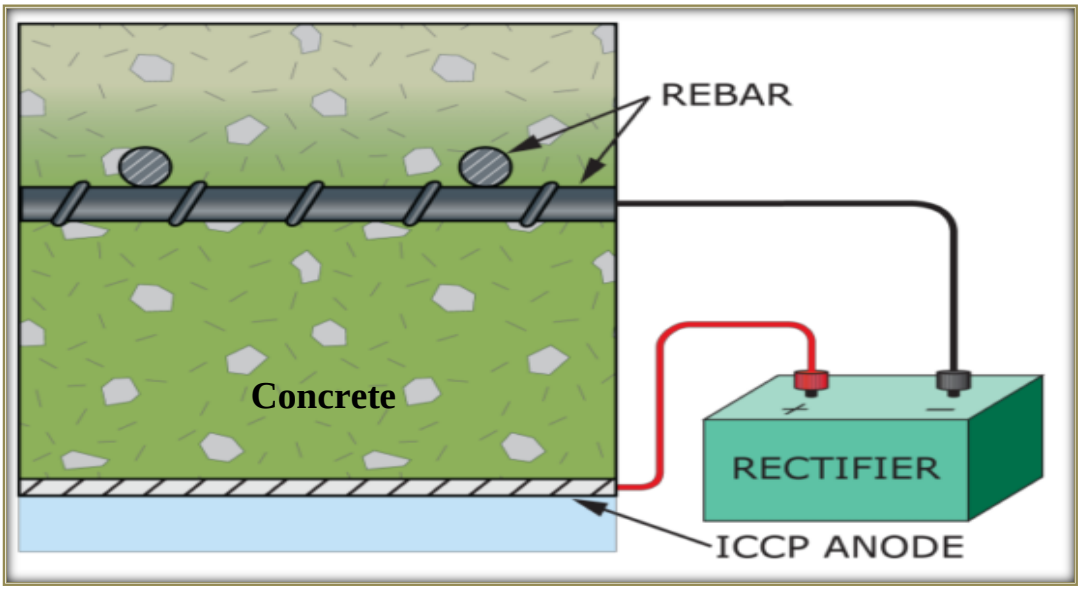

Figure 2.11: Impressed current system (after Tienna *et al.*, 2014).

- ***Electrochemical realkalization***: Realkalization is a technique that depends on increasing the alkalinity of the concrete above 11 to renew the passivity of the steel by transporting an alkaline solution into the pores inside the concrete using an external electric current. This method is very effective for carbonated concrete (Whitmore and Ball, 2009).
- ***Chloride extraction***: Chloride extraction depends on transporting the chloride ions away from the steel while generating a substantial increase in alkalinity around the reinforcing steel by using high level of direct current for a relatively short duration. As a result, the structure will be left in the non-corroding condition (Whitmore and Ball, 2009).

2.5.3. Research on sacrificial anodes

Using the zinc sacrificial anode to prevent the corrosion of the steel embedded in the concrete has been investigated by many researchers (Oladis *et al.*, 1997; Bertolini *et al.*, 2002; Sergi, 2011). However, there is dearth of research on the application of the sacrificial anodes to mitigate the deleterious effect of the ring anode phenomenon, except for Page and Sergi (2000). Page and Sergi (2000) have evaluated the performance of the sacrificial anodes when the patch repair takes place. Four RC slabs (1000 × 500 × 100 mm) were cast with two different dosages of sodium chloride (0.8% and 4% chloride by weight of cement). The sodium chloride was incorporated into the slabs at specific locations. Then, the authors applied a patch repair technique to the slabs after one year. The damaged concrete was removed to expose the corroded reinforcement and the bars were cleaned. Afterwards, fresh chloride-free repair concrete was cast reinstating the original case of each bar. In some slabs, a single disc of zinc anode was buried and electrically connected to the steel reinforcement externally. The authors concluded that the results have been encouraging where using the sacrificial anode was effective in keeping the anodic region within the repaired area.

During the corrosion process, there are four types of currents circulating inside the concrete:

1. Anodic current (I_a), represents the number of electrons migrating during the anodic reaction.
2. Cathodic current (I_c), represents the number of the electrons reacted within the cathodic reaction.
3. The current flow through the steel itself (I_m).
4. The current circulating inside the concrete through the electrolyte (I_{con})

If the corrosion of steel bars occurred, the four current should be equal. Corrosion current (I_{cor}), the rate of the overall process of corrosion, is a common value which represents the four types of currents.

To the best of the author's knowledge, no research data are currently available on the range of resistivity of repair materials/concrete within which zinc anodes were used to retain their functionality. Based on the aforementioned definitions, the author assumed that the corrosion current is equal to the current generated from the sacrificial anode. This assumption simplifies the assessment of the sacrificial anode when it is embedded in the high resistivity concrete. There are many studies that have been carried out to correlate the resistivity of the concrete and the corrosion current. For example, Hornbostel *et al.* (2013) reviewed existing research on the relationship between corrosion rate and concrete resistivity. It was concluded that current generated inside the concrete and flow through the electrolyte is within the range believed to be adequate for cathodic prevention, as shown in Fig. 2.12. Also, González *et al.* (2004) proposed a relationship between the resistivity and the corrosion rate of bars embedded in slabs. Also, it was concluded that the current is within the range for cathodic prevention, as shown in Fig. 2.13.

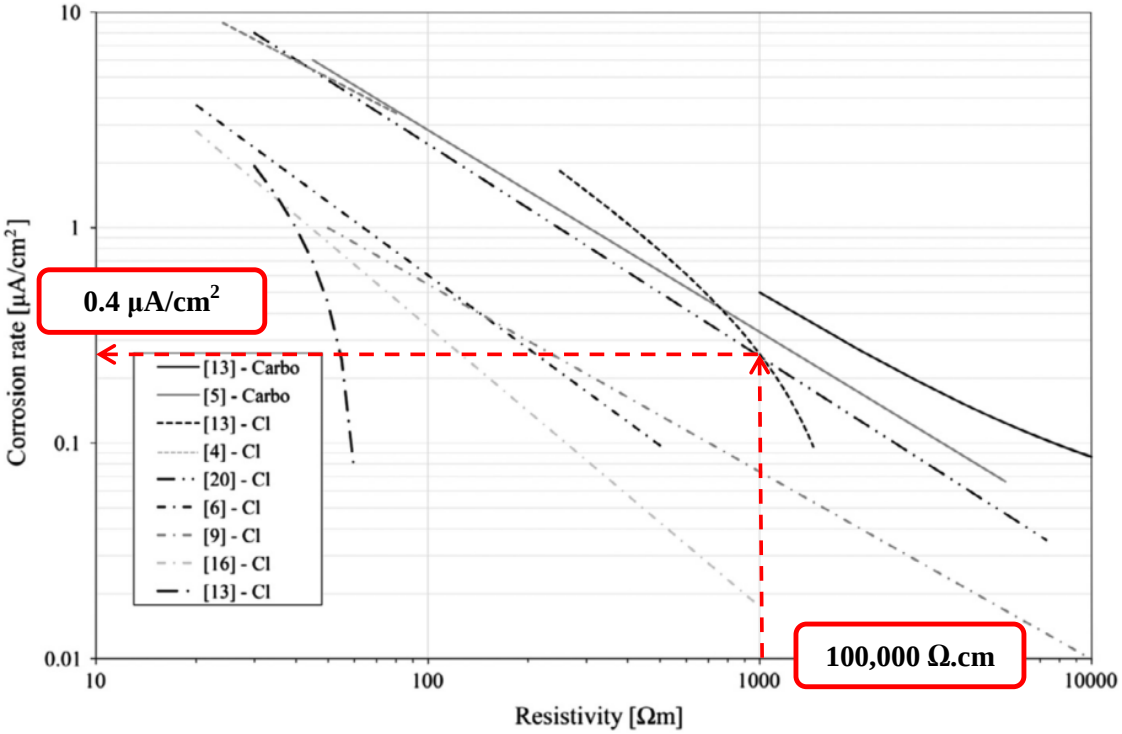

Figure 2.12: The relationship between corrosion rate and concrete resistivity (after Hornbostel *et al.*, 2013).

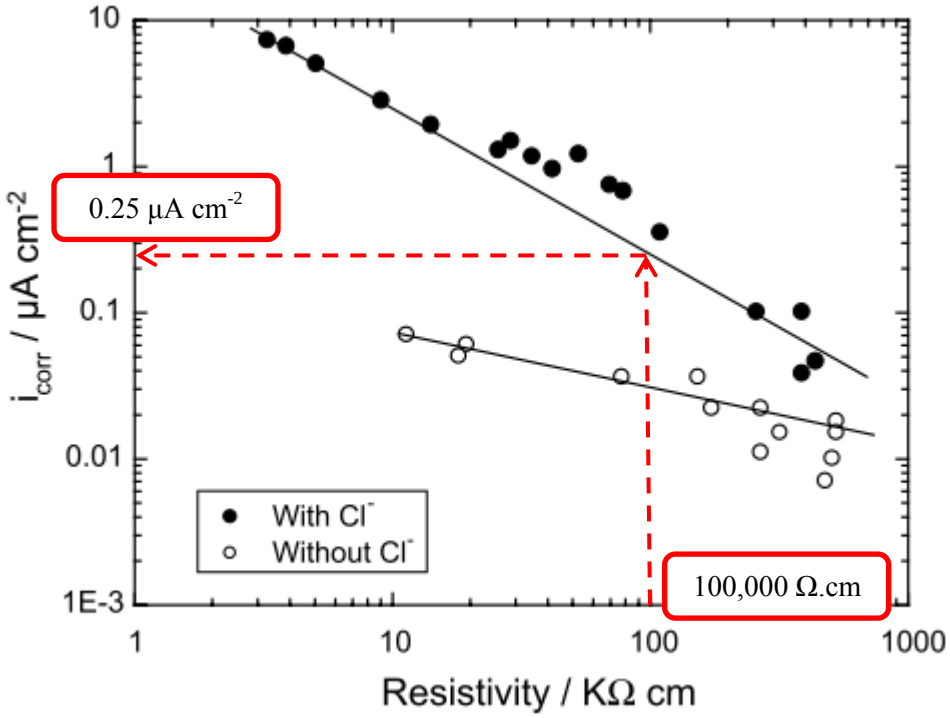

Figure 2.13: The relationship between corrosion rate and concrete resistivity (after González *et al,*. 2004).

2.6. Closure

Demands for using electrical resistivity techniques (surface and bulk resistivity) as an alternative to the rapid chloride penetrability test (RCPT) have been growing to give an indication of the relative penetrability of concrete. While resistivity measurements may reflect the quality of pore structure in the cementitious matrix, their accuracy might be affected by a multitude of parameters including the concentration of ionic species in the pore solution, particularly when supplementary cementitious materials (SCMs) are incorporated in the binder. Consequently, one of the main objectives of the first part of this thesis is to establish a tripartite relationship (nomogram) to correlate surface resistivity with penetrability (migration coefficient) and porosity of concrete and to evaluate its practicality for field applications.

In addition, to date, there is dearth of research data on the application of sacrificial anodes to mitigate the deleterious effect of the 'halo effect' phenomenon in repaired concrete. In particular, no published work has focused on investigating the effect of the resistivity of concrete, in which those anodes are embedded, on the response of sacrificial anodes to control corrosion activity of embedded reinforcement. Hence, the second part of this thesis mainly aims at identifying the range of resistivity of repair materials/concretes within which zinc anodes retain their functionality.

Chapter 3 : Experimental Program

This chapter describes the materials, mixture designs, procedures, and experimental methods adopted in this research program. The experiments were divided into two parts: characterizing the electrical resistivity of concrete, and studying its effect on the functionality of zinc anodes in repaired concrete.

3.1. Electrical Resistivity of Concrete

3.1.1. Materials and mixtures

In this part of the experimental program, general use (GU) Portland cement, Portland limestone cement (PLC, comprising 6 to 15% interground limestone powder with clinker), silica fume (SF), and Type F fly ash (FA), which meet the requirements of CAN/CSA- A3001 (CSA3001, 2013) [Cementitious Materials for Use in Concrete] standard were used as the main components of the binders. In addition, colloidal nano-silica (NS) [aqueous solution with 50% solid content] and colloidal nano-alumina (NA) [aqueous solution with 20% solid content] were incorporated in some mixtures to modify the binders. The chemical and physical properties of these materials are shown in Table 3.1, and the physical characteristics of nanoparticles are shown in Table 3.2. Locally available coarse aggregate (natural gravel with max. size of 9.5 mm) and fine aggregate (well graded river sand with fineness modulus of 2.9) were used. The specific gravity and absorption were 2.65 and 2%, respectively for gravel and 2.53 and 1.5%, respectively for sand. In order to achieve a good workability level, a high-range water reducing admixture (HRWRA) based on polycarboxylic acid and complying with ASTM C494/C494M (ASTM C494, 2012) [Standard Specification for Chemical Admixtures for Concrete] was added to all mixtures in the range of (0 to 2000 ml/100 kg binder), depending on the water-to-binder ratio (w/b) and binder

constituents, to maintain a slump range between 75 and 150 mm. In addition, an air-entraining admixture according to ASTM C233/C233M (ASTM C233, 2014) [Standard Test Method for Air-Entraining Admixtures for Concrete] was added (10 ml to 20 ml/100 kg binder depending on the w/b and binder constituents) in some mixtures to achieve a fresh air content of about 5-6%.

In total, forty three mixtures were prepared in this program; the total binder content in all mixtures was ranging between 270 to 400 kg/m^3. The mixture design variables were w/cm (0.3, 0.35, 0.4, 0.5, 0.6, and 0.7), type of binder (GU cement or PLC, and GU cement blended with SCMs or PLC blended with SCMs), air-entraining agent, and ultrafine particles (nano-silica or nano-alumina). The mixture IDs were coded according to the type of cement, w/b and SCMs. For example, mixture GU0.3FA30SF5 was prepared with GU cement, w/b of 0.30, 30% fly ash and 5% silica fume, and mixture PLC0.4FA30NA6 was prepared with PLC, w/b of 0.40, 30% fly ash and 6% nano-alumina. The proportions of the mixtures are listed in Table 3.3. Finally, to accomplish one of the aforementioned objectives in Chapter one, five-field cores extracted from newly constructed and aging pavement sections in Winnipeg, Canada, as shown in Figure 3.1,

Figure 3.1: Examples of the field cores used in this study.

were employed in the next Chapter to validate the tripartite relationship (nomogram).

Table 3.1: Chemical and physical properties of cement and SCMs.

	GU	**PLC**	**Fly Ash**	**Silica Fume**	**Nano-Silica**	**Nano-Alumina**
Chemical Composition						
SiO_2 (%)	19.8	19.2	56.0	92.0	99.2	--
Al_2O_3 (%)	5	4.4	23.1	1.0	0.38	99.5
Fe_2O_3 (%)	2.4	2.6	3.6	1.0	0.02	--
CaO (%)	63.2	61.5	10.8	0.3	--	--
MgO (%)	3.3	2.4	1.1	0.6	0.21	--
SO_3 (%)	3.0	3.4	0.2	0.2	--	--
Na_2O (%)	0.1	0.2	3.2	0.3	0.2	--
Physical Properties						
Fineness (m^2/kg)	390	460	290	20000	80000	160000
Specific Gravity	3.17	3.08	2.12	2.22	1.40	1.19

Table 3.2: Physical characteristics of nano-silica and nano-alumina.

	Nano-Silica (NS)	**Nano-Alumina (NA)**
Solid content, wt%	50	20
pH	9.5	--
Viscosity, cP	8	--
Density, g/cm3	1.40	1.19
Na_2O, wt%	0.2	--
Mean Particle Size (nm)	35	50

Table 3.3: Proportions of mixtures per cubic meter of concrete.

Mixture ID.	Description	Cement (kg)	Fly Ash (kg)	Silica Fume (kg)	Nano Silica (kg)	Nano-Alumina (kg)	w/b	Coarse Agg. (kg)	Fine Agg. (kg)
GU0.3	GU, single	400	--	--	--	--	0.3	946	948
GU0.35	GU, single	380	--	--	--	--	0.35	936	939
GU0.4	GU, single	400	--	--	--	--	0.4	1227	607
GU0.5	GU, single	300	--	--	--	--	.5	947	950
GU0.6	GU, single	315	--	--	--	--	0.6	891	893
GU0.7	GU, single	270	--	--	--	--	0.7	909	912
GU0.3SF8	GU, binary, SF	368	--	32	--	--	0.3	1130	755
GU0.3SF10	GU, binary, SF	360	--	40	--	--	0.3	1130	755
GU0.3+AIR	GU, single , air	400	--	--	--	--	0.3	894	897
GU0.35+AIR	GU, single , air	380	--	--	--	--	0.35	884	887
GU0.4+AIR	GU, single , air	400	--	--	--	--	0.4	1159	573
GU0.5+AIR	GU, single , air	300	--	--	--	--	.5	896	898
GU0.6+AIR	GU, single , air	315	--	--	-	--	0.6	839	842
GU0.7+AIR	GU, single , air	270	--	--	--	--	0.7	858	860
GU0.3SF8+AIR	GU, binary, SF, air	368	--	32	--	--	0.3	1067	714
GU0.3SF10+AIR	GU, binary, SF, air	360	--	40	--	--	0.3	1067	714
GU0.4FA20	GU, binary, FA	320	80	--	--	--	0.4	1077	580
GU0.4FA30	GU, binary, FA	280	120	--	--	--	0.4	1068	575
GU0.4SF5	GU, binary, SF	370	--	20	--	--	0.4	1212	606
GU0.4FA30SF5	GU, ternary, FA, SF	254	117	20	--	--	0.4	1184	592
GU0.4NS5	GU, binary, NS	370	--	--	39	--	0.4	1224	612
GU0.4NS6	GU, binary, NS	376	--	--	48	--	0.4	1091	587
GU0.4NA6	GU, binary, NA	376	--	--	--	120	0.4	1064	573
GU0.4FA20NS6	GU, ternary, FA, NS	296	80	--	48	--	0.4	1072	577

Table 3.3 (Cont'd): Proportions of mixtures per cubic meter of concrete

Mixture ID.	Description	Cement (kg)	Fly Ash (kg)	Silica Fume (kg)	Nano Silica (kg)	Nano-Alumina (kg)	w/b	Coarse Agg. (kg)	Fine Agg. (kg)
GU0.4FA30NS5	GU, ternary, FA, NS	253	117	--	39	--	0.4	1196	598
GU0.4FA30NS6	GU, ternary, FA, NS	256	120	--	48	--	0.4	1063	572
GU0.4FA20NA6	GU, ternary, FA, NA	296	80	--	--	120	0.4	1045	563
GU0.4FA30NA6	GU, ternary, FA, NA	256	120	--	--	120	0.4	1036	558
GU0.4FA30SF5NS5	GU, quaternary, FA, SF, NS	234	117	19.5	39	--	0.4	1180	590
PLC0.4	PLC, single	400	--	--	--	--	0.4	1096	590
PLC0.4FA20	PLC, binary, FA	320	80	--	--	--	0.4	1077	580
PLC0.4FA30	PLC, binary, FA	280	120	--	--	--	0.4	1068	575
PLC0.4SF5	PLC, binary, SF	370	--	20	--	--	0.4	1212	606
PLC0.4FA30SF5	PLC, ternary, FA, SF	254	117	20	--	--	0.4	1184	592
PLC0.4NS5	PLC, binary, NS	370	--	--	39	--	0.4	1224	612
PLC0.4NS6	PLC, binary, NS	376	--	--	48	--	0.4	1091	587
PLC0.4NA6	PLC, binary, NA	376	--	--	-	120	0.4	1064	573
PLC0.4FA20NS6	PLC, ternaty, FA, NS	296	80	--	48	--	0.4	1072	577
PLC0.4FA30NS5	PLC, ternaty, FA, NS	253	117	--	39	--	0.4	1196	598
PLC0.4FA30NS6	PLC, ternaty, FA, NS	256	120	--	48	--	0.4	1063	572
PLC0.4FA20NA6	PLC, ternaty, FA, NA	296	80	--	--	120	0.4	1045	563
PLC0.4FA30NA6	PLC, ternaty, FA, NA	256	120	--	--	120	0.4	1036	558
PLC0.4FA30SF5NS5	PLC, quaternary, FA, SF, NS	234	117	19.5	39	--	0.4	1180	590

3.1.2. Procedures

All the materials were mixed in a high-shear mixer according to ASTM C192 (ASTM C192, 2014) [Standard Practice for Making and Curing Concrete Test Specimens in the Laboratory]. A specific sequence of mixing was implemented based on experimental trials to achieve

homogenous dispersion of constituent materials. First, approximately 15% of the mixing water was added to the aggregate while mixing for 30 s. The cement and SCMs were then added to the aggregate and mixed together for 1 min. In case of using nanoparticles, the colloidal nano-silica or nano-alumina and the admixtures (air-entraining admixture, or HRWRA) were added to the remaining water while stirring vigorously for 45 s to obtain a liquid phase containing well-dispersed nanoparticles and admixtures. Finally, the liquid phase was added to the binder and aggregates and mixing continued for 2 min. After mixing and casting the concrete, a vibrating table was used to ensure good compaction for specimens. Polyethylene sheets were used to cover the surface of specimens for 24 h. Also, it worth mentioning that such procedures were followed for the whole research program except for some different procedures adopted solely for each part of the program.

Four cylindrical (100×200 mm) replicates were prepared from each batch for all tests (Surface Resistivity [SR] (AASHTO TP 95-14, 2014), Bulk Resistivity [BR], Rapid Chloride Penetrability Test [RCPT] (ASTM C1202, 2012), and Mercury Intrusion Porosimetry [MIP]). All the specimens were demolded after 24 h and cured in a standard curing room (maintained at a temperature of 22±2^{o}C and relative humidity of more than 95%) according to ASTM C192 (ASTM C192, 2014) until testing at 28 days.

3.1.3. Tests

3.1.3.1. Rapid Chloride Penetrability Test (RCPT)

The interconnectivity of pore system in concrete specimens was assessed by RCPT according to ASTM C1202 (ASTM C1202, 2012) [Standard Test Method for Electrical Indication of Concrete's Ability to Resist Chloride Ion Penetration]. At 28 days, the surface skin (~3 mm) from the top and bottom of cylindrical specimens was removed to reach a clear surface, and the

adjacent 50 mm thick discs were cut as the test specimens. The discs were air-dried in the laboratory for one hour and then their side surfaces were coated with rapid setting epoxy to reduce moisture evaporation and leakage of solution during testing. Subsequently, the concrete discs were placed in a desiccator under vacuum pressure for three hours. Concurrently, the required amount of water was boiled for de-aeration and allowed to cool down to ambient temperature. After three hours of vacuuming, de-aerated water was allowed to enter into the desiccator while the vacuum pump was still running. Subsequently, for additional one hour, the vacuum pump was operated and then the valve was opened to allow air to flow into the desiccator. The specimens were kept in the desiccator and soaked under water for 18 hours before the test. On the following day, the concrete discs were put in the test cells, where one compartment was filled with 3% NaCl solution (cathode) while the other compartment was filled with 0.3% NaOH solution (anode). During the test period (six hours), 60 V DC was applied to the cell compartments, while the temperature of sodium chloride solution was continuously monitored by a thermocouple. The computer connected to the microprocessor power supply recorded all the data during the entire test in terms of passing charges in Coulombs through concrete to determine the penetrability class according to ASTM C1202 (ASTM C1202, 2012) as shown in Figure 3.2. To calculate the resistivity, the current was recorded after 1 minute to avoid high temperature effects following the guidelines of ASTM C1760 (ASTM C1760, 2012) [Standard Test Method for Bulk Electrical Conductivity of Hardened Concrete]. Equation (3.1) was used to calculate the resistivity in Ω.cm, where V is the applied voltage (V), A is the specimen's cross-sectional area (cm^2), I is the recorded current (A), and L is the specimen's thickness (cm).

$$Resistivity = \frac{VA}{IL} \qquad (Eq.3.1)$$

Since physical observation provides better representation of the penetration of chloride ions into concrete, the physical penetration depth of chloride ions was measured immediately after the completion of the test by spraying 0.1 M $AgNo_3$ solution on the surface of equally split discs. The discs were allowed to set under fluorescent light for about 15 minutes to obtain the whitish precipitate of silver chloride. Five penetration depths (every 20 mm) were measured on each half disc (i.e. 10 readings per specimen) to calculate the average penetration depth for each specimen [Bassuoni et.al 2006].

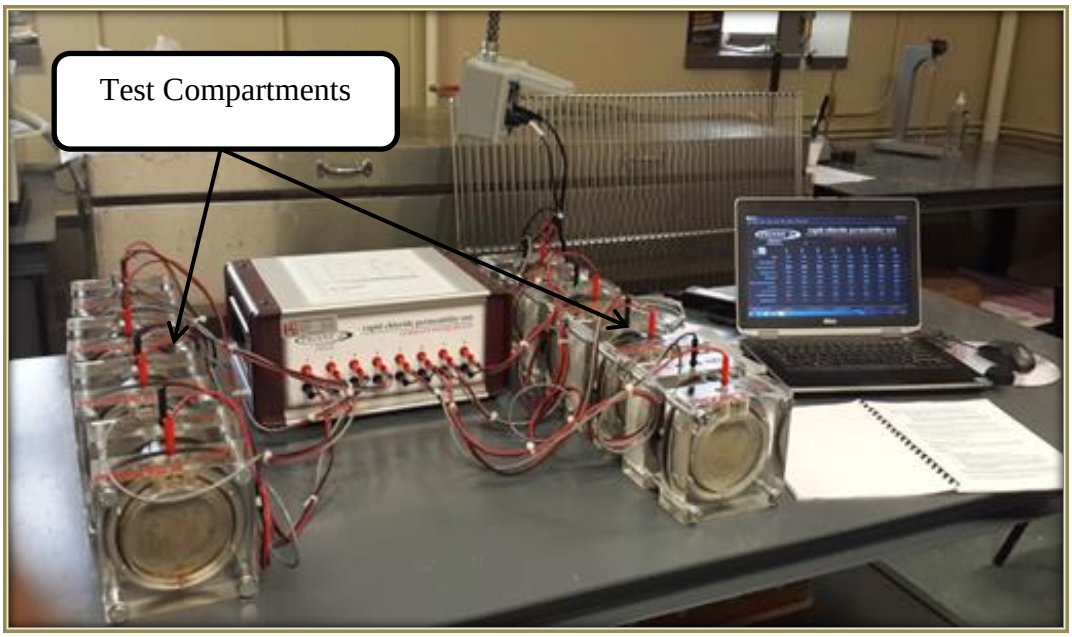

Figure 3.2: RCPT apparatus.

3.1.3.2. Bulk Resistivity (BR)

A two-pin bulk resistance meter (manufactured by NILSSON, Model 400) was used to determine the bulk resistivity (BR) of saturated surface dry concrete cylinders as shown in Figure 3.3. The apparatus consists of a control box, two square titanium plate electrodes (150 × 150 × 3 mm), and two conductor wires to connect the control box to the plates. The specimen was placed

between the electrodes, and an alternating current [AC] (97 Hz) was applied through the specimen by the control box. To ensure appropriate electrical connection between the specimen and the plate electrodes, sponges saturated with a sodium sulfate solution were inserted between the specimen and electrode plates at the top and bottom ends of the specimen. The device measured the electrical resistance by adjusting the ohms dial, located in the control box, until the null indicator was balanced in the middle. The resistance, which is measured in ohms, is the raw output from the apparatus. To calculate the electrical resistivity in Ω.cm, Equation 3.2 was applied, where L is the specimen's length (cm), and A is the specimen's cross-sectional area (cm^2).

$$Bulk\ resistivity = Bulk\ resistance \times \frac{A}{L} \qquad (Eq.3.2)$$

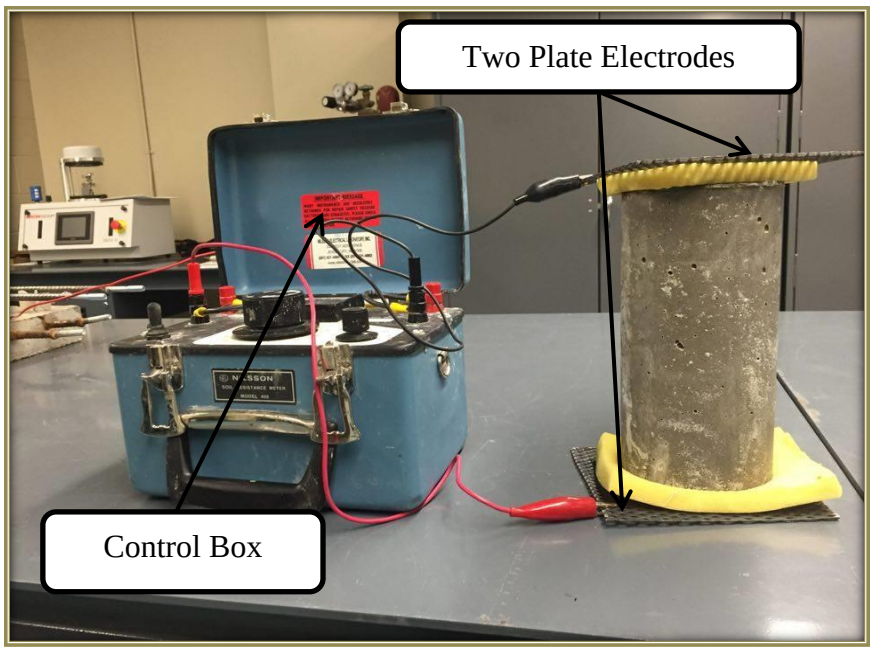

Figure 3.3: 2-pin AC resistance test set-up.

3.1.3.3. Surface Resistivity (SR)

The surface resistivity (SR) was determined by the Wenner four-electrode method following the general guidelines of AASHTO TP 95-14 (AASHTO TP 95-14, 2014) [Standard Method of Test for Surface Resistivity Indication of Concrete's Ability to Resist Chloride Ion Penetration], except that the four electrodes were equally spaced at 38 mm. By placing the four electrodes on the surface of the concrete, the two exterior electrodes apply an AC current (13 Hz), while the two inner electrodes measure the electrical potential created. Subsequently, the value of SR is obtained (in Ω -cm) automatically from the control box which is connected to the four probes by a conductor wire.

For the first part of the program (Electrical Resistivity of Concrete), after removing the sample from the mold, four indelible marks were made on the top finished circular face marking the 0, 90, 180, and 270 degree points of the circumference. At 28 days, the specimens were taken out from the standard curing room and tested while their surfaces were wet. During the test, the air temperature around the specimens shall be maintained in the range of 20 to 25^{o}C, then the Wenner array probe were placed on the longitudinal side of the sample. The measurement was recorded from the display unit after the reading becomes stable, then the sample was rotated from the 0 to 90 degree mark, from 90 to 180 degree mark, and from 180 to 270, and every time the measurement was taken. Then, the average resistivity was calculated. For the second part of the program (Improving the Efficiency of Sacrificial Anodes), The resistivity of slabs was monitored with the time of exposure (after the wetting cycles) by measuring the surface resistivity (SR) rather than the bulk resistivity because of the difficulty in positioning the bulk resistivity set-up on a flat system (such as slabs). This is the reason for commonly using SR set-ups in field applications. The SR was determined by placing the four probes on the surface of the

repair section of the slabs without anode three times parallel to the longitudinal direction of the bars, as shown in Figure 3.4. One measurement was between the two bars, and the other two were beside the steel, then the average surface resistivity was calculated.

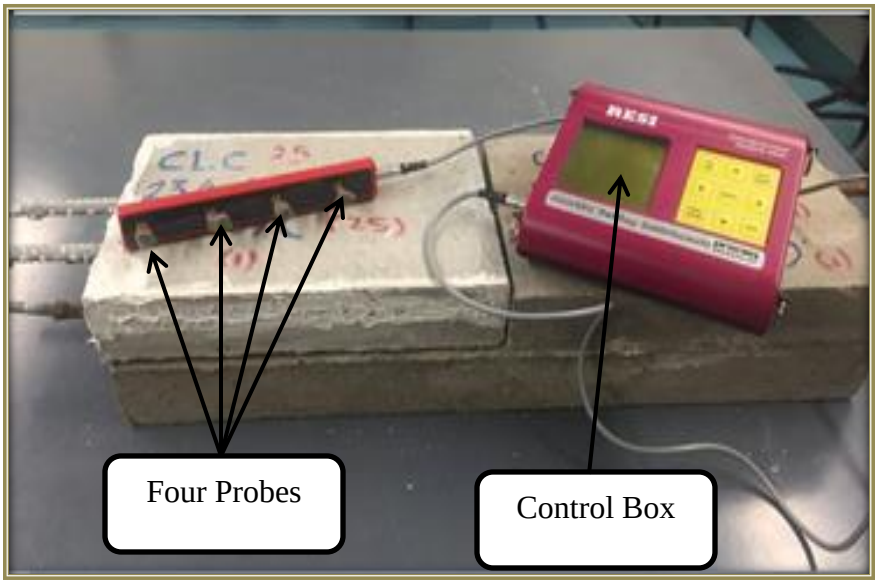

Figure 3.4: Wenner probe array test set-up.

3.1.3.4. Mercury Intrusion Porosimetry (MIP)

Small pea-sized chunks (about 6) taken from at least two concrete cylinders of each mixtures were used as test samples for mercury intrusion porosimetry (MIP) [Figure 3.5]. These chunks were around 4 to 7 mm in size, and were carefully selected so that large aggregates were not included. Preconditioning of samples was done by oven drying at 45±2°C until a constant mass to reduce the potential of drying shrinkage cracks associated with higher temperatures. The apparatus had a pressure range from sub-ambient to 228 MPa. By assuming a cylindrical geometry of pores, a mercury contact angle of 130° and surface tension of 485 dynes/cm, the high pressure limit (228 MPa) yields a pore radius of about 3 nm, implying intrusion of all

capillary pores since the smallest size of capillary pores reported in literature is about 5 nm [Kumar *et al.*, 2003].

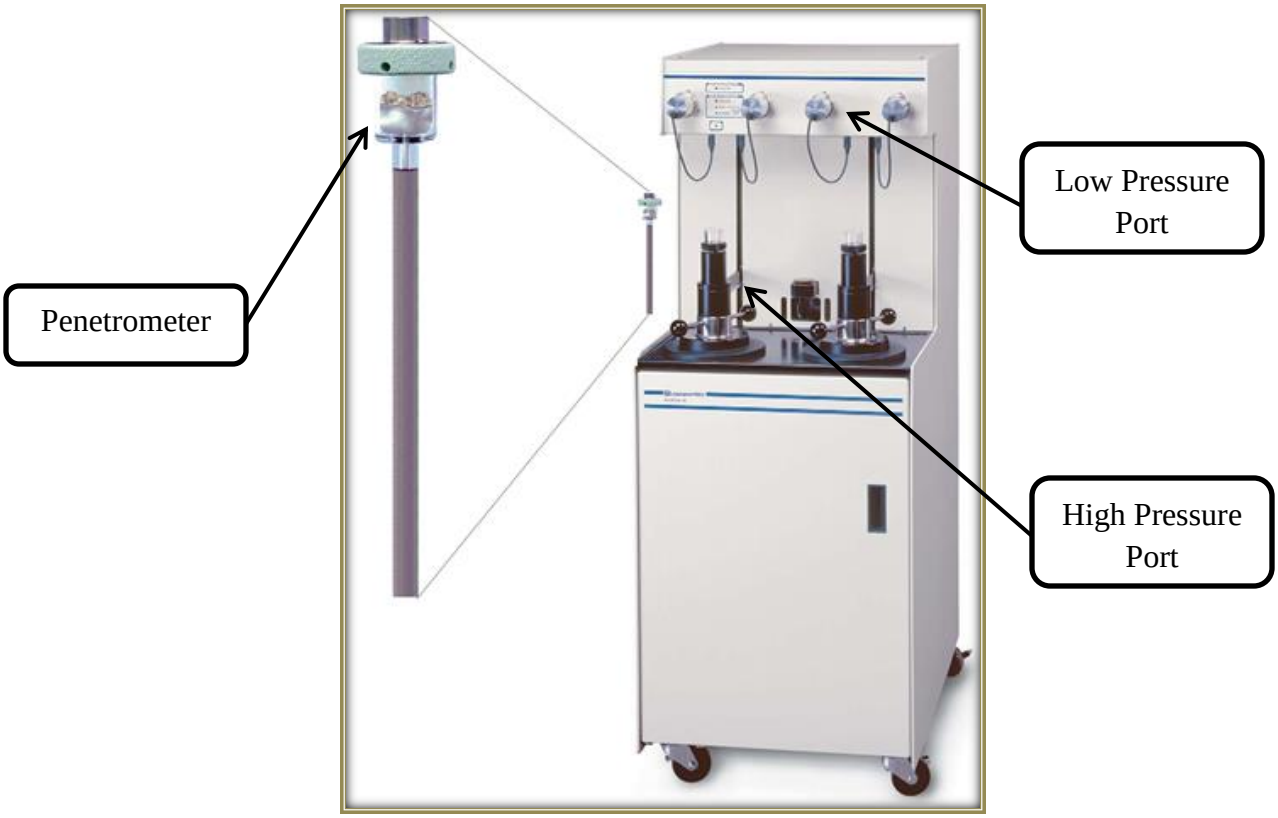

Figure 3.5: MIP apparatus.

3.2. Functionality of Zinc Anodes in Repaired Concrete

3.2.1. Materials and mixtures

In this part of the experimental program, two types of cement were also used: general use (GU) portland cement and Portland limestone cement (PLC), CAN/CSA- A3001 (CSA3001, 2013) specifications to produce various concrete mixtures. Class F fly ash (FA) and silica fume (SF) were used in some (binary and ternary) binders at replacement levels of 30, and 8%, respectively. Also, nano-silica (NS) was used at a dosage of 6% by the total binder content to produce ternary

binder. The solid content of the colloidal is NS 50 % by mass. The chemical and physical properties of these materials are shown in Table 3.1, and the physical characteristics of the nano-silica are shown in Table 3.2. The target flow of fresh mortar was achieved by a high-range water reducing admixture. This HRWRA was added at different dosages (0 to 30 ml per 5.5 kg of mortars) to the mixtures in order to maintain good workability level. Similar to electrical resistivity part, the fine aggregate used in this study was well graded river sand with a specific gravity, fineness modulus and absorption of 2.65, 2.9 and 2%, respectively, and locally available coarse aggregate was used with specific gravity and absorption of 2.65 and 2%, respectively. Also, 5-6 % of fresh air content was fulfilled by incorporating air-entraining admixture according to ASTM C233/C233M (ASTM C233, 2014). For scientific (specific) purposes, sika repair material (Sika Repair 223: cementitious patching mortar), and a colloidal polymer (Sika Latex R: acrylic based, polymer emulsion) were used in this syudy. Only one type of reinforcing bars was used as longitudinal reinforcement: No 10M deformed steel bars. The mechanical properties of the deformed steel bars was obtained from standard tests carried out according to the ASTM A370 (ASTM A370, 2014) [Standard Test Methods and Definitions for Mechanical Testing of Steel Products]. Table 3.4 shows the mechanical properties of the used steel bars. The zinc sacrificial anode (puck shape, Figure 3.6) was used in this program. Atotal of five mixtures (designated as R_i, R_{ii}, R_{iii}, R_{iv} , and R_v) were prepared for this part of the program, four of them were concrete mixtures, while R_v was a mortar mixture. It is worth noting that such mixtures were extracted from the fundemental study implemented earlier in this program (the electrical resistivity of concrete).The proportions of the mixtures are shown in Table 3.5.

Table 3.4: Mechanical properties of the steel bars (provided by manufacturer).

Size	Diameter (mm)	Area (mm^2)	Modulus of Elasticity (GPa)	Yield Strength (MPa)	Ultimate strain
No. 10M	11.3	100	200	400	0.002

Table 3.5: Proportions of mixtures per cubic meter of concrete.

Mixture ID.	Description	Cement (kg)	Fly Ash (kg)	Silica Fume (kg)	Nano Silica (kg)	Nano-Alumina (kg)	w/b	Coarse Agg. (kg)	Fine Agg. (kg)
R_i	GU, single , air	300	--	--	--	--	.5	896	898
R_{ii}	GU, single , air	400	--	--	--	--	0.3	894	897
R_{iii}	GU, binary, SF, air	368	--	32	--	--	0.3	1067	714
R_{iv}	GU, ternary, FA, NA	256	120	--	--	120	0.4	1036	558
R_v	Sika Repair 223 + Sika latex R								

Figure 3.6: Zinc sacrificial anode used in this study.

3.2.2. Procedures

This study has been conducted on duplicate mini-scale slabs (205 mm wide × 610 mm long × 120 mm thick) poured in three sections as shown in Figures 3.7(a)-(b). The bottom half (chloride free concrete) were prepared from normal concrete with a 28-day resistivity of approximately

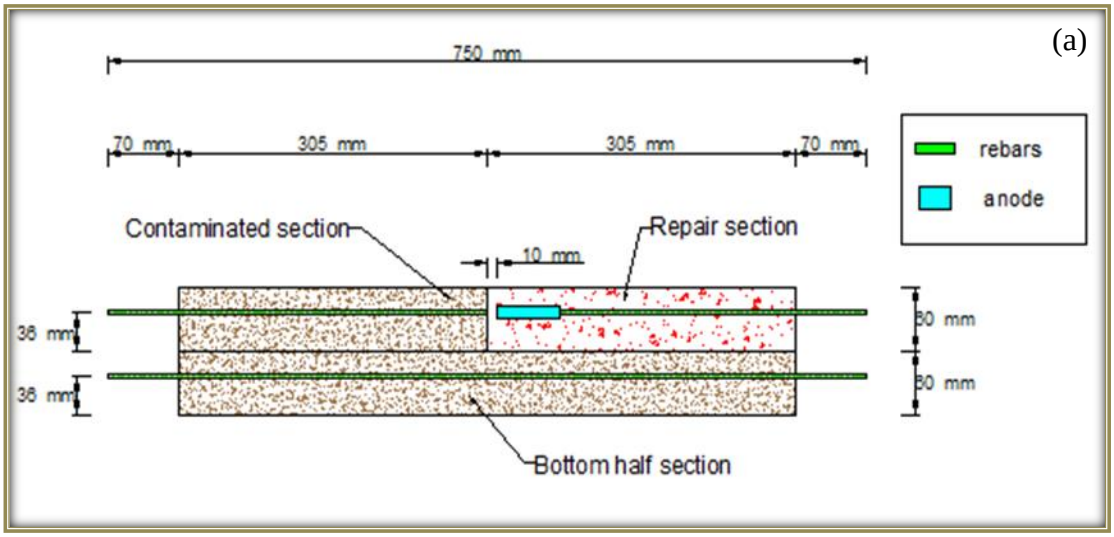

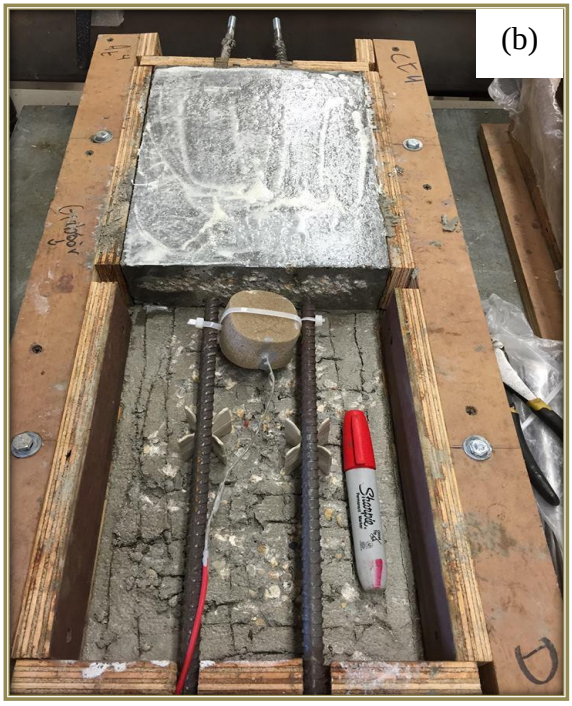

Figure 3.7: A cross-section from a slab specimen with the reinforcement and anode assembly: (a) a schematic diagram, and (b) a real slab.

5,000 Ω -cm (cement content and w/c of 300 kg/m^3 and 0.50, respectively), and it was reinforced with two longitudinal 750 mm 10 M bars. This (parent/old) concrete mixture design is within the typical range of concrete bridge deck slabs built 25-35 years ago (Ramey *et al.*, 1997; Feldman and Bartlett, 2007). The top half was split into two equal sections: one section (old concrete: contaminated with 3% calcium chloride by mass of cement) with a 28-day resistivity of 5,000 Ω-cm, and it was reinforced with two 10 M bars with 375 mm length, whereas the other section (repair patch-chloride free) had a varied resistivity. The reinforcement in the patched part was two 10 M bars with 365 mm length, positioned to leave 10 mm gap from the bar in the adjacent chloride contaminated concrete to ease monitoring the current generated (output) from the anode to each rebar in the assembly through external wiring. All bars protruded outside the formwork by 70 mm, and all protruded portions were epoxy-coated to suppress corrosion to take place from any external source; in other words, coating the protruded portions with epoxy will restrict the corrosion to occur only inside the slab as intended in the design as shown in Figure 3.8. The simulated repair sections in the slabs were prepared with five different concrete mixtures (R_i, R_{ii}, R_{iii}, R_{iv} , and R_v) as shown in Table 3.5 to cover a wide range of bulk electrical resistivity between 5,000 and 100,000 Ω-cm. The zinc anodes (puck shape, Figure 3.6) were mounted in the repair sections at spacing of 25,100, and 250 mm measured from the end of the steel bar. Conforming to ASTM C309 (ASTM C309, 2012) [Standard Specification for Liquid Membrane-Forming Compounds for Curing Concrete], a membrane curing compound was applied to prevent the loss of water from the surface of concrete at early-age and to simulate curing in the field (Figure 3.9). The current in the three sections has been monitored by external wire connections and electrical switches (Figure 3.10) to determine the current in each bar individually. To accelerate the onset of corrosion, the slabs have been exposed to continuous

wetting-drying cycles. Each cycle consisted of ponding (5 to 15 mm) the surface of specimens with fresh water for two weeks at a temperature of 22±2˚C, followed by drying at 22±2˚C and 35±5% RH for two weeks. The specimens have been put in a controlled lab temperature, and a dehumidifier has been used in the drying cycles to obtain the target humidity level. Furthermore, Additional set of slabs were cast in this study, but without zinc anodes (control slabs), to assess the functionality of zinc anodes to control electrochemical corrosion of bars.

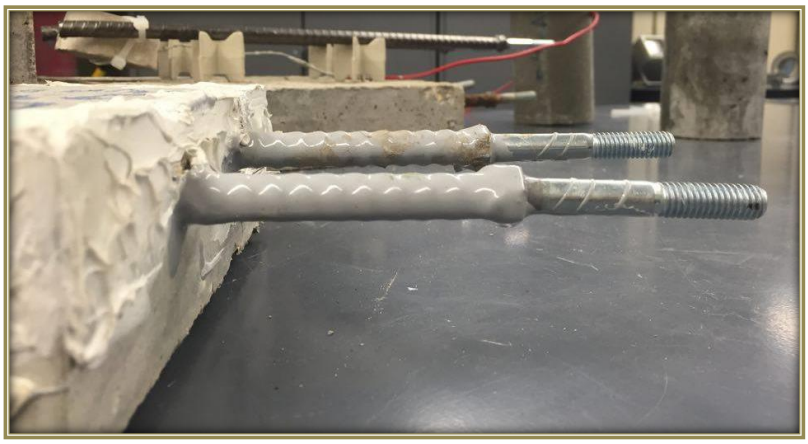

Figure 3.8: Epoxy-coating on protruded ends.

Figure 3.9: Membrane of curing compound applied to the slabs.

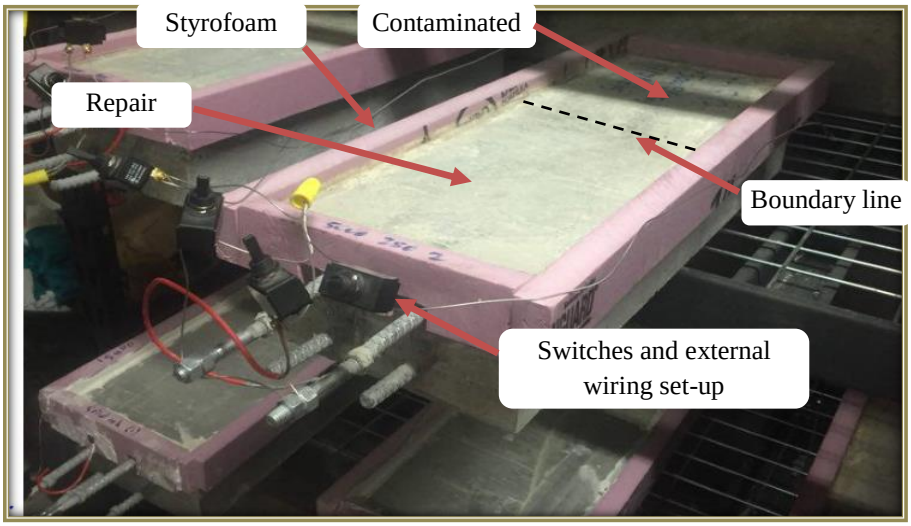

Figure 3.10: Full set-up of a slab specimen.

3.2.3. Tests

The electrical measurements were particularly employed herein to assess the functionality of the zinc anode (the second part of the program).

3.2.3.1. Current Measurements

The current was measured using a precision digital multimeter (Model MAS830B, maximum capacity of 10A) every two weeks (at the end of each exposure cycle). Four multimeters were used simultaneously, where the positive end of the multimeters was connected to the steel bars in each section, and the negative end was connected to the zinc anodes, as shown in Figure 3.11. An instantaneous current measurement was recorded just after disconnection of the anode to minimize the resistance of the multimeter itself. To calculate the current density in mA/m^2, the reading of the current obtained from the multimeter was normalized by the outer surface area of the bars being measured, neglecting the protruded portions coated by epoxy.

Figure 3.11: The multimeters configuration to measure the current.

3.2.3.2. Potential Measurements

The potential of steel bars has been evaluated against portable copper-copper sulfate reference electrode (CSE) in accordance with the technique described in ASTM C876 (ASTM C876, 2009) [Standard Test Method for Corrosion Potentials of Uncoated Reinforcing Steel in Concrete]. Only one multimeter was used, where the positive end of the multimeter was connected to the steel bar that needed to be measured, while the negative end of the multimeter was connected to the reference electrode. The reference electrode was arbitrarily positioned in the middle of the steel bar as shown in Figure 3.12, rather than taking multiple measurements along the steel bar because there is no predefined minimum spacing between measurements stipulated in the

specification. In addition, there was no substantial difference between the measurements along the steel bar, as for example shown in Figure 3.13.

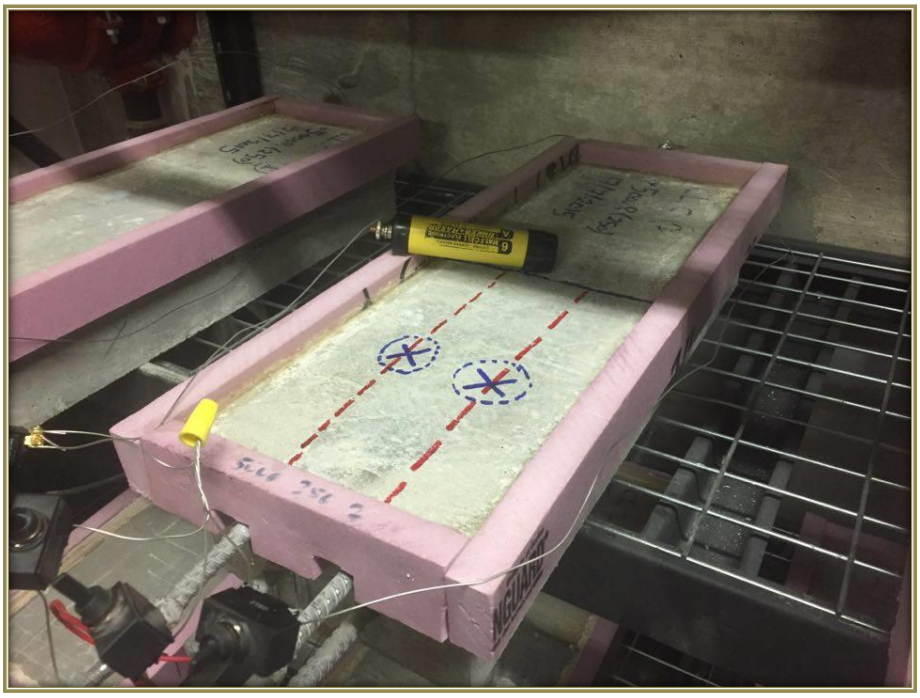

Figure 3.12: Half-cell potential measurement locations.

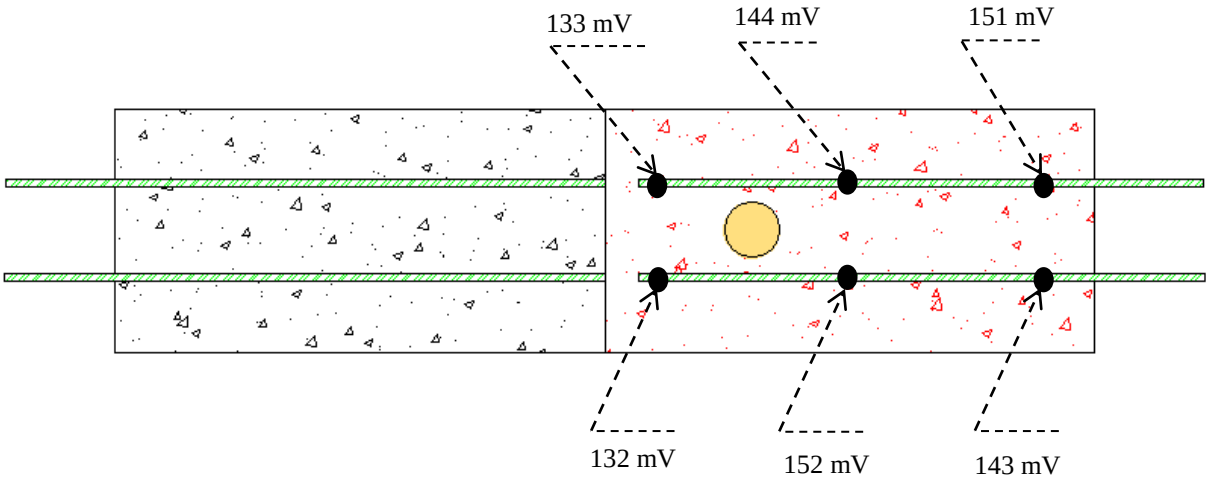

Figure 3.13: Half-cell potential measurements along the steel bars.

3.2.3.4. Depolarization Decay

The "100 mV decay" criterion, used for verifying the protection conditions in RC structures, is based on the measurement of potential decay after switching off the current. The structure is considered protected if the difference between the instant-off potential and the potential measured after 24 hours is higher than 100 mV. This criterion is stipulated by (EN 12696-1, 2000; NACE SP0290, 2007) and was adopted in the present thesis.

Chapter 4 : Results and Discussion for Resistivity, Penetrability and Porosity of Concrete

4.1. Surface and Bulk Resistivity

The average SR of four cylinders measured at 28 days and associated standard error for all the mixtures are shown in Figures 4.1(a)–(c). The standard error (calculated by dividing the standard deviation of data by the square root of the number of replicates) was small (±4.5%) compared to the average results, which indicates the repeatability of SR as a quality indicator for concrete. The SR method could capture the effect of the key mixture design variables on concrete, and the trends were assessed by the analysis of variance (ANOVA) method at a significant level (α) of 0.05 as summarized in Table 4.1. According to Montgomery (2012), exceeding the F_{cr} value of an *F*-distribution density function indicates that the variable tested has a significant effect on the average results. An example of the SR raw data layout and corresponding ANOVA results for the case of w/b are given in Tables 4.2 and 4.3.

The SR results showed that the effect of w/b conformed to the well-documented trend linked to the physical characteristics of the pore structure, and in turn to the electrical conductance of concrete. For example, increasing the w/b from 0.3 to 0.7 led to 64 % reduction in the SR of specimens [Figure 4.1(a)]. Compared to the control mixtures containing GU cement without air-entrainment, the incorporation of an air-entraining agent in similar mixtures appeared to have a mixed effect on the SR results; the same trend was replicated for mixtures containing binary binders (GU and SF) without and with air-entrainment [Figure 4.1(a)]. For example, the results for single binder specimens with air-entrainment (GU0.3+Air to GU0.7+Air) showed

increase and decrease, without a consistent pattern, in the SR values compared to counterparts without air-entrainment. This insignificant effect of air-entrainment was statistically supported by ANVOA for the SR results, as changing the air-content among the GU and GU with SF mixtures yielded *F* values of 0.17 and 0.7, respectively which are smaller than their F_{cr} values of 4.05 and 4.6 (Table 4.1), respectively. It is conceivable that air-entrainment of concrete produces a network of closely spaced bubbles that increases the total porosity of concrete; however, these air-bubbles are disconnected (Wong *et al.*, 2011), and thus they do not seem to enhance the ionic mobility within the cementitious matrix.

Compared to single binder mixtures [Figure 4.1(a)], the addition of different dosages of silica fume and/or fly ash in in binary and ternary binders (GU0.3SF8, GU0.3.SF10, GU0.4SF5, GU0.4FA20, GU0.4FA30, and GU0.4FA30SF5) significantly increased the SR results of concrete at 28 days [Figures 4.1(a)-(b)], which ranged from 17.8 to 58.5 kΩ.cm. For example, increasing the dosage of fly ash from 0 to 30% had an *F* value of 15.1, which is larger than the F_{cr} of 5.0 (Table 4.1). This can be linked to the effect of these SCMs on densifying the pore structure via filler effect, pozolanic reactivity and/or binding of ionic species in the cementitious matrix, thus reducing its conductivity (Caldwell, 1998; Lataste, 2010). Regarding the mixtures with nano-silica (NS), incorporating small dosages of this ultrafine material in binary, ternary, or quaternary binders led to a marked increase in the SR of concrete (Figure 4.1(b), and Table 4.1). The addition of 5 or 6% nano-silica by mass of the binary binder (GU0.4NS5 and GU0.4NS6) led to a significant increase in the SR of specimens by an average factor of 3.6 relative to that of the control specimens (GU0.4), which was 14.5 kΩ.cm. Relative to silica fume, the smaller particle size of nano-silica (about 35 nm) provides a huge surface area (80000 m^2/kg) which vigorously speeds up the rate of cement hydration; in addition, nano-silica can contribute

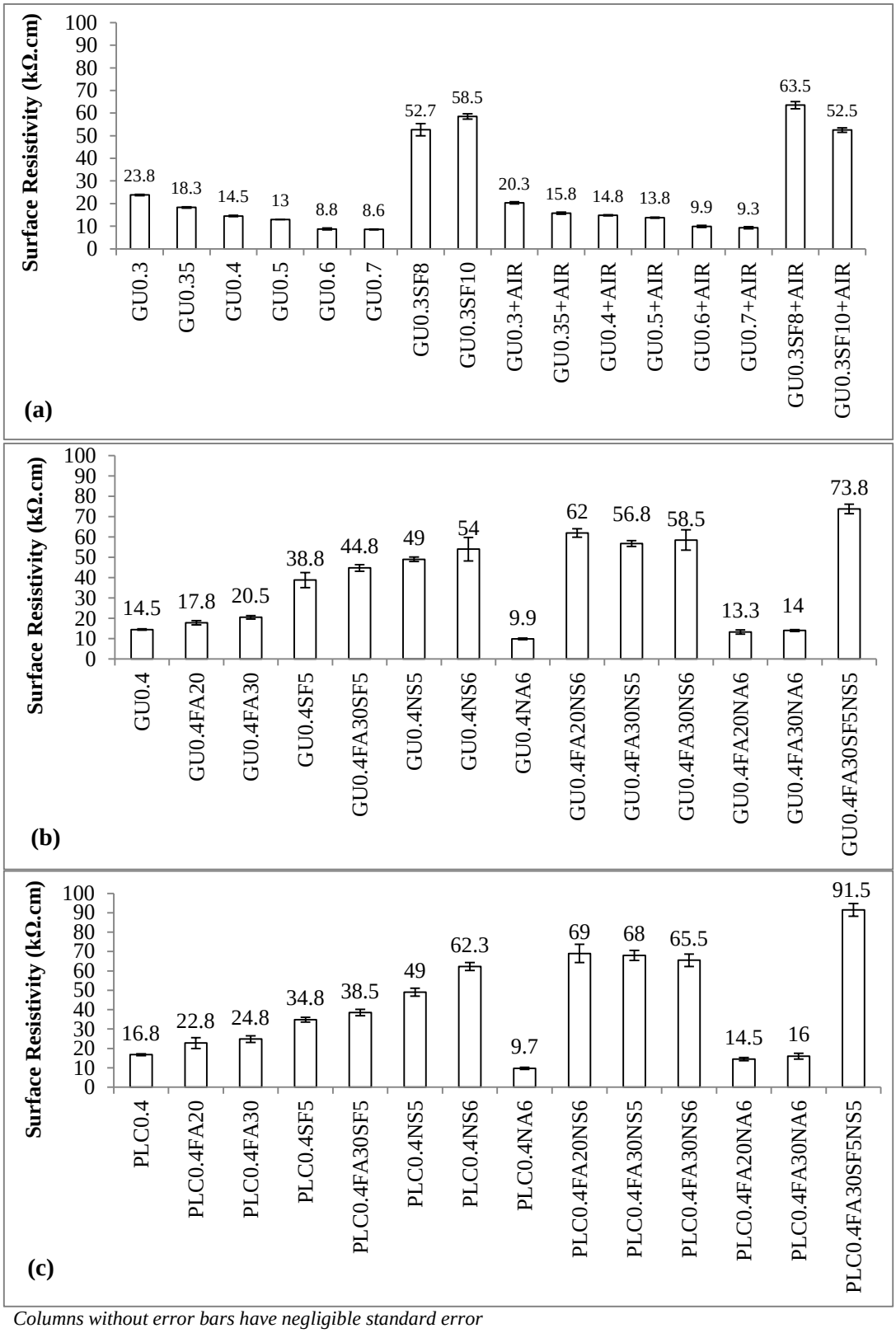

Columns without error bars have negligible standard error

Figure 4.1: The average SR of concrete specimens considering the effect of (a) w/b and air-entrainment, (b) SCMs, and (c) type of cement.

Table 4.1: Summary of the ANOVA for the SR, BR, and penetrability results.

Test	Variable	F	F_{cr}	Effect
SR	w/b	499.9	2.77	Significant
	Air-entrainment (GU)	0.169	4.06	Insignificant
	Air-entrainment (GU + SF)	0.71	4.6	Insignificant
	Fly ash	15.1	4.96	Significant
	Silica fume	42.6	5.98	Significant
	Nano-silica	72.5	4.96	Significant
	Nano-alumina	85.78	5.98	Significant
	PLC	0.69	3.93	Insignificant
BR	w/b	475.7	2.77	Significant
	Air-entrainment (GU only)	0.82	4.06	Insignificant
	Air-entrainment (GU + SF)	0.27	4.6	Insignificant
	Fly ash	16.44	4.96	Significant
	Silica fume	81.62	5.98	Significant
	Nano-silica	418.6	4.96	Significant
	Nano-alumina	240.2	5.98	Significant
	PLC	0.61	3.93	Insignificant
RCPT (penetrability)	w/b	914.5	2.3	Significant
	Air-entrainment (GU only)	0.62	3.88	Insignificant
	Air-entrainment (GU + SF)	2.81	3.96	Insignificant
	Fly ash	71.2	4.01	Significant
	Silica fume	157.9	4.1	Significant
	Nano-silica	199	4	Significant
	Nano-alumina	84.6	4.1	Significant
	PLC	1.71	3.86	Insignificant

Table 4.2: The SR results (kΩ.cm) of four replicates showing the effect of w/b.

	w/b					
	0.3	**0.35**	**0.4**	**0.5**	**0.6**	**0.7**
Cylinder 1	23	18	14	13	9.2	8.6
Cylinder 2	24	18	15	13	9.2	9.2
Cylinder 3	24	18	14	13	7.6	8.3
Cylinder 4	24	19	15	13	9.2	8.6

Table 4.3: The ANOVA results for the data shown in Table 4.2.

Source of Variation	**SS**	**df**	**MS**	**F**	**Fcr**
Between Groups	673.2	5	134.6	499.9	2.77
Within Groups	4.85	18	0.269		
Total	678.1	23			

SS: sum of squares, df: degrees of freedom, and MS: mean square.

physical filler and pozzolanic effects to the cementitious matrix, which together may lead to densifying the cementitious matrix and increasing its resistivity (Belkowitz *et al.,* 2014). Correspondingly, incorporation of only 5 or 6% nano-silica with fly ash and GU cement led to notable improvement in the SR of concrete at 28 days. For example, the SR of specimens from mixture GU0.4FA30NS6 was about three times higher than that of the corresponding specimens without nano-silica (GU0.4FA30), which was 20.5 kΩ.cm. Furthermore, specimens prepared from the quaternary binder (GU, fly ash, silica fume, and nano-silica; GU0.4FA30SF5NS6) had the highest SR of about 73.8 kΩ.cm among the specimens prepared with the GU cement. In contrast to the behaviour of nano-silica, the SR trends showed that the incorporation of nano-alumina had adverse effects on the SR of concrete, irrespective of the type of binder (binary, or ternary). For instance, the SR of the control mixture GU0.4 was 14.5 kΩ.cm, but addition of 6% nano-alumina (GU0.4NA6) led to 33% reduction in the SR value. This may allude to a coarse and continuous pore structure originating from an agglomeration effect (inconsistent dispersion of particles), due to a relatively high dosage of ultrafine particles (specific surface of 160000 m^2/g) (Bassuoni and Rahman, 2016). The latter argument is substantiated by the RCPT and MIP results discussed later in the text.

All the single, binary, ternary, and quaternary mixtures with a w/b of 0.4 were reproduced with PLC instead of GU cement, and the average SR results are shown in Figure 4.1(c). Generally, the inclusion of PLC instead of GU cement led to an increase (in the range of 9% to 28%) in the SR of PLC specimens compared to that of the corresponding specimens prepared with GU cement (Figure 4.1(b)). This might be ascribed to the higher fineness of the PLC (460 m^2/kg) in comparison to the GU cement (390 m^2/kg) due to intergrinding limestone powder with clinker, which can improve the hydration process and microstructural evolution of concrete

(Voglis *et al.,* 2005). Limestone particles may act as nucleation sites for the hydration products (Tennis *et al.,* 2011), and the reaction between limestone and alumina phases in clinker may produce additional hydration products of calcium carboaluminate (Ramezanianpour and Hooton, 2014). In addition, the filler effect resulting from the continuous particle size distribution of PLC may yield better particle packing in the matrix (Barrett *et al.,* 2013). However, this trend was invalid for some mixtures due to the predominant effect of SCMs and nanoparticles (e.g. PLC0.4FA30SF5 and PLC0.4NS5, respectively vs. GU0.4FA30SF5 and GU0.4NS5). Thus, the overall effect of using PLC instead of GU for all mixtures did not significantly affect the SR results (Table 4.1). Again, these trends were substantiated by the penetrability and MIP results discussed in the next section.

The average values of BR and standard error of four cylinders for all mixtures measured at 28 days are shown in Figures 4.2(a)–(c). BR of concrete may reflect the quality of pore structure because it is a volumetric property which indicates the ability to transport electrical charges trough interconnected pore space. Likewise, it depends on the concentration and mobility of ionic species in the pore solution. Reducing the w/b and/or incorporating SCMs such as fly ash or silica fume had a significant effect (Table 4.1) on increasing the BR of concrete due to reducing the pore sizes and connectivity in the cementitious matrix; in addition, SCMs decrease the ionic concentration in the pore solution because of binding ionic species to the matrix (Lataste, 2010). Again, unlike nano-alumina, adding nano-silica probably enhanced pore structure refinement and the binding of ionic species, resulting in increased BR of specimens. Overall, all the aforementioned SR trends were replicated in the BR results. Consistently, specimens with high BR had high SR and vice versa. For example, specimens prepared from the quaternary binder with PLC (PLC0.4FA30SF5NS5) showed the highest BR of 45.2 kΩ.cm

(Figure 4.2(c)), corresponding to the highest SR value of 91.5 kΩ.cm (Figure 4.1(c)). The average ratio of SR to BR of concrete was about 2.33, which is in good agreement with previous studies (Morris *et al.,* 1996; Sengul and Gjørv, 2009; Spragg *et al.,* 2012; Ghosh and Tran, 2014), which reported a ratio ranging between 1.86 to 2.66. Unlike the current study, these studies did not investigate effects of air-entrainment, nanoparticles and PLC on resistivity of concrete. Therefore, it might be reasonable to state that a ratio of SR to BR of 2.33 is generally acceptable for concrete.

The relationship between SR and BR of concrete, for the range of the mixture designs tested herein, is shown in Figure 4.3. A power relationship between both parameters was obtained, with a coefficient of determination (R^2) of 0.96, indicating a strong association between the two datasets, except for marginal differences. These differences may be attributed to the so-called "polarization phenomenon" which induces an electric field opposite in direction to the electric field applied to measure the SR, and thus exaggerating the results of SR for concrete specimens relative to their true values (Steen *et al.,* 1998; Cao and Chung, 2004; Du Plooy *et al.,* 2013) . This phenomenon depends mainly on the configuration of the SR test-setup, and it has been reported that using point probes worsen the polarization problem, due to non-uniform distribution of ions (concentration of ions underneath the probes) within layers parallel to the probes (Steen *et al.,* 1998).

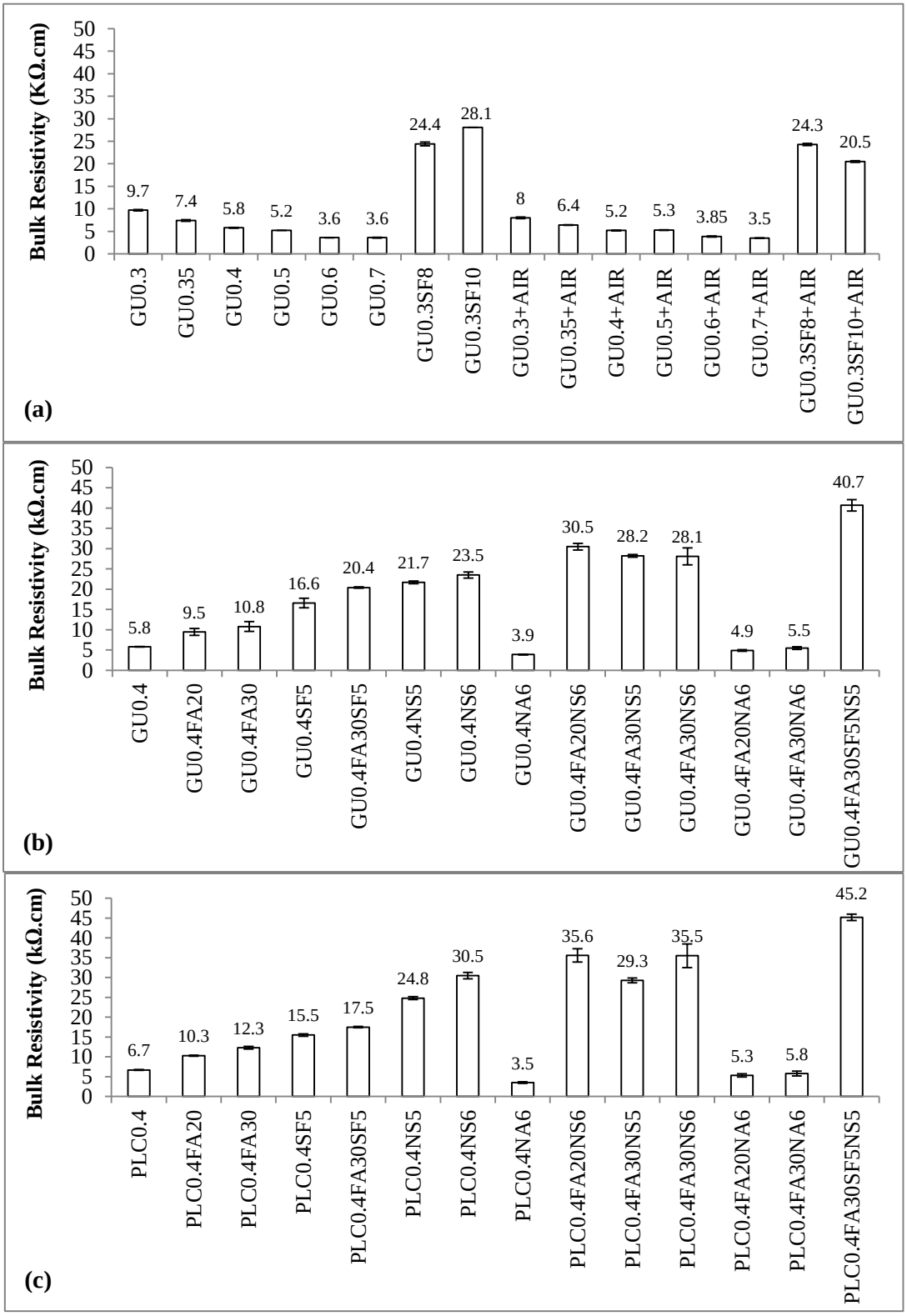

Columns without error bars have negligible standard error

Figure 4.2: The average BR of concrete specimens considering the effect of (a) w/b and air-entrainment, (b) SCMs, and (c) type of cement

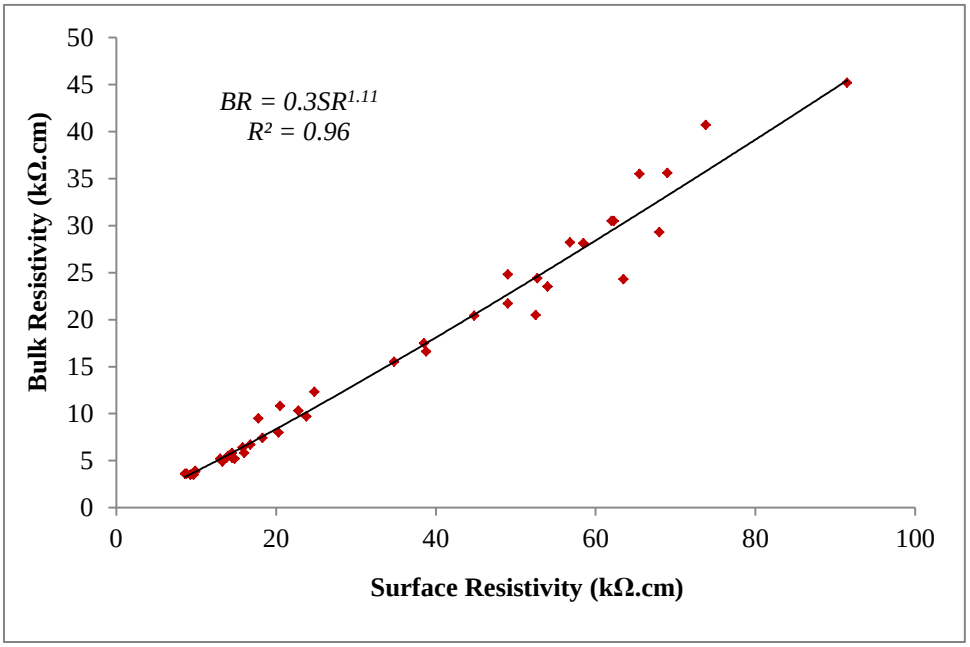

Figure 4.3: Correlation between surface and bulk resistivity of concrete.

4.2. Penetrability

The average penetration depths from RCPT and apparent porosity from MIP are listed in Table 4.4. All the aforementioned trends in the resistivity tests regarding w/b, air-entrainment, SCMs and type of cement were generally replicated (including statistical significance; Table 4.1) by the penetration depth, which reflects the physical features of microstructure of concrete. For example, the average penetration depths for the mixtures prepared with w/b of 0.3 and 0.7 were 9.4 and 50 mm, respectively, since the higher water content increased the porosity from 10.12 to 22.35 %. Incorporating an air-entraining agent in concrete increased the apparent porosity of hardened concrete by a maximum of 2.5%; however, this did not necessarily lead to increasing the penetration depth of chloride ions, but in some cases this parameter decreased. This might be ascribed to the fact that the existence of discrete air-bubbles in the matrix can lead to a tortuous pore network (Mehta and Monteiro, 2014) which can discount the migration of chloride ions into

concrete. Thus, similar to the resistivity trends, air-entrainment had an insignificant effect on the penetration depth results as changing the air content among the GU and GU with SF mixtures yielded *F* values of 0.62 and 2.81, respectively which are smaller than the F_{cr} values of 3.88 and 3.96 (Table 4.1).

Generally, it can be noted that the incorporation of different types of SCMs such as silica fume and/or fly ash with different dosages had a significant effect (Table 4.1) on reducing the penetration depth and porosity of specimens. For instance, adding 30 % fly ash and/or 5% silica fume in binary and ternary binders (GU0.4FA30, GU0.4SF5, and GU0.4FA30SF5) led to 49, 70, and 61% reduction in the penetration depth of specimens, respectively compared to that of the corresponding specimens prepared with GU cement only, which was 17.6 mm; this corresponded to 11, 20, and 8% reduction in the apparent porosity, which highlights the role of SCMs in refining and densifying the pore structure of the matrix and thus reducing its penetrability.

Moreover, when using an ultrafine pozzolan such as nano-silica in the binder, the significant specific surface area of the particles leads to speeding up the rate of hydration and pozzolanic reactions, resulting in refined microstructure. For example, using the same dosage (5%) of nano-silica (specific surface of 80000 m^2/kg) compared to silica fume (specific surface of 20000 m^2/kg) in binary mixtures (GU0.4NS5 and GU0.4SF5) reduced the penetration depth and porosity by 21% and 5%, respectively. Correspondingly, specimens prepared from the quaternary binder incorporating nano-silica (GU0.4FA30SF5NS5) showed approximately 72% and 13% reduction in the penetration depth and porosity of specimens, respectively when compared to control specimens (GU0.4).

Table 4.4: Parameters obtained from RCPT and MIP tests.

Mixture ID.	Average Penetration Depth (mm)	Migration Coefficient ($\times 10^{-12} m^2/s$)	Average Porosity (%)
GU0.3	9.4 [0.51][a]	8.62	10.12
GU0.35	12.7 [0.61]	12	9.97
GU0.4	17.6 [0.94]	17.27	13.9
GU0.5	28.9 [0.8]	29.31	18.6
GU0.6	50 [0]	53.4	21.6
GU0.7	50 [0]	53.09	22.35
GU0.3SF8	6.5 [1.12]	5.66	9.15
GU0.3SF10	6.2 [0.76]	5.37	8.72
GU0.3 +AIR	7.4 [0.76]	6.63	11.73
GU0.35 +AIR	12.9 [0.88]	12.01	12.54
GU0.4 +AIR	27.8 [0.68]	28.21	14.82
GU0.5 +AIR	28.3 [1.77]	29.59	19.96
GU0.6+AIR	50 [0]	53.4	22.33
GU0.7 +AIR	50 [0]	54.22	23.70
GU0.3SF8 +AIR	4.8 [0.48]	4.06	9.41
GU0.3SF10 +AIR	3.8 [0.37]	3.13	8.99
GU0.4FA20	11 [0.64]	10.16	15.05
GU0.4FA30	9 [0.57]	8.16	12.36
GU0.4SF5	5.3 [0.39]	4.9	11.12
GU0.4FA30SF5	6.8 [0.96]	5.98	12.76
GU0.4NS5	4.2 [0.60]	4.5	10.56
GU0.4NS6	5 [0.6]	4.24	10.47
GU0.4NA6	29 [0.97]	46.23	19.62
GU0.4FA20NS6	6 [0.73]	5.16	10.91

Table 4.4 (Cont'd): Parameters obtained from RCPT and MIP tests.

Mixture ID.	Average Penetration Depth (mm)	Migration Coefficient ($\times 10^{-12} m^2/s$)	Average Porosity (%)
GU0.4FA30NS5	3.5 [0.34]	2.85	12.52
GU0.4FA30NS6	8 [0.64]	7.06	11.82
GU0.4FA20NA6	37 [0.82]	38.7	20.62
GU0.4FA30NA6	33 [0.75]	34.09	20.3
GU0.4FA30SF5NS5	5 [1.1]	4.24	12.15
PLC0.4	10.1 [1.27]	9.48	13.56
PLC0.4FA20	11.4 [1.14]	10.47	14.75
PLC0.4FA30	12.6 [3.96]	11.61	15.21
PLC0.4SF5	5 [0.45]	4.29	10.26
PLC0.4FA30SF5	6.8 [0.85]	5.97	11.29
PLC0.4NS5	4.0 [1.06]	3.86	11.52
PLC0.4NS6	7 [0.81]	6.6	11.6
PLC0.4NA6	34 [1.36]	45.56	19.54
PLC0.4FA20NS6	4.8 [0.38]	4.04	10.379
PLC0.4FA30NS5	3.2 [0.37]	2.57	11.62
PLC0.4FA30NS6	6.2 [0.53]	5.35	10.99
PLC0.4FA20NA6	28.1 [0.62]	28.59	18.51
PLC0.4FA30NA6	25.4 [1.47]	25.52	18.76
PLC0.4FA30SF5NS5	4.5 [0.78]	3.77	12.58

[a]*Standard error is shown between brackets*

This indicates that adding SCMs with variable sizes and reactivates was efficient in refining the pore structure of concrete and enhancing its discontinuity relative to the control specimens. However, it is worth noting that the physical features of this quaternary binder and in turn the penetration depth of its specimens are for example comparable to that of specimens from

binary binders (e.g. GU0.4SF5 and GU 0.4NS5) [Table 4.4], but the resistivity values were much higher for this quaternary binder [Figures 4.1(b) and 4.2(b)]. This is originating from the effect of electrolysis bias, which entails that quaternary binders were much better in binding ionic species in the pore solution of the cementitious matrix, and thus reducing its conductivity. However, this did not correspond to extreme refinement of the pore structure of concrete (i.e. significant reduction in physical penetrability) relative to concrete prepared from binary or ternary binders (depending on the specific combinations of SCMs).

In contrast to the effect of nano-silica at reducing the porosity and in turn the penetration depth of specimens, incorporating nano-alumina in concrete, regardless of the type of binder (binary or ternary), yielded a noticeable increase in the porosity and penetrability. For example, compared to the binary specimens containing GU cement and 6% nano-silica (GU0.4NS6) which had a penetration depth of 5 mm (porosity of 10.5%), the incorporation of nano-alumina in concrete at the same dosage and w/b (GU0.4NA6) led to significantly increasing the penetration depth to 29 mm (porosity of 19.6%) as depicted in Figure 4.4.

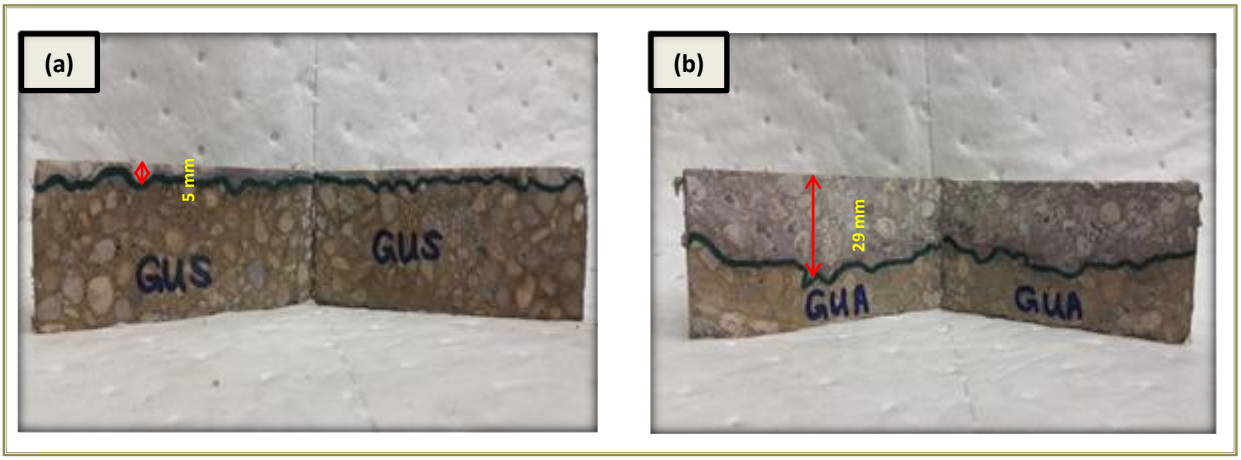

Figure.4.4: Whitish color showing the chloride penetration depth in specimens prepared from mixtures: (a) GU0.4NS6, and (b) GU0.4NA6.

This explains the lower resistivity values for specimens incorporating nano-alumina, due to the agglomeration effect that led to a continuous microstructure (total porosity of 18 to 20%, Table 4.4). Similar to the resistivity trends, ANOVA (Table 4.1) for the penetration depth results showed that replacing the GU cement with PLC had *F* value of 1.71, which was less than the critical value (F_{cr}) of 3.86, indicating that the effect of this parameter was statistically insignificant. For example, the results of the penetration depth for specimens prepared from the quaternary binder, but with different types of cement (GU0.4FA30SF5NS6 and PLC0.4FA30SF5NS6) showed that the difference in the values between both groups of specimens was negligible, which highlights the predominant role of SCMs, irrespective of the type of cement (GU or PLC).

As mentioned previously, an alternative measurement (chloride penetration depth) from RCPT, which better correlates to the physical characteristics of the pore structure of concrete was employed in this study to alleviate and capture biases induced by pore solution conductivity that influence resistivity results. The association of the physical penetration depth of specimens with their total porosity can be noted in Figure 4.5.

As discussed in a previous example, comparing the results of two different mixtures such as GU0.4NS5 and GU0.4FA30SF5NS5 emphasizes the applicability of using the penetration depth to indicate the true quality of microstructure of concrete; while the SR for such mixtures was 49 and 74 kΩ.cm, respectively, the penetration depths for these specimens were comparable (4.2 and 5 mm, respectively) due to similar porosity (11 and 12%, respectively). For further improvement of this relationship between penetrability and porosity, the chloride migration coefficient of concrete was calculated on the basis of the penetration depth from Eq. 4.1 (NT BUILD 492-99, 1990) in order to discount effects of high heat and different testing durations on

ionic mobility within specimens (Bassuoni *et al.*, 2006), which particularly affected specimens with high w/b.

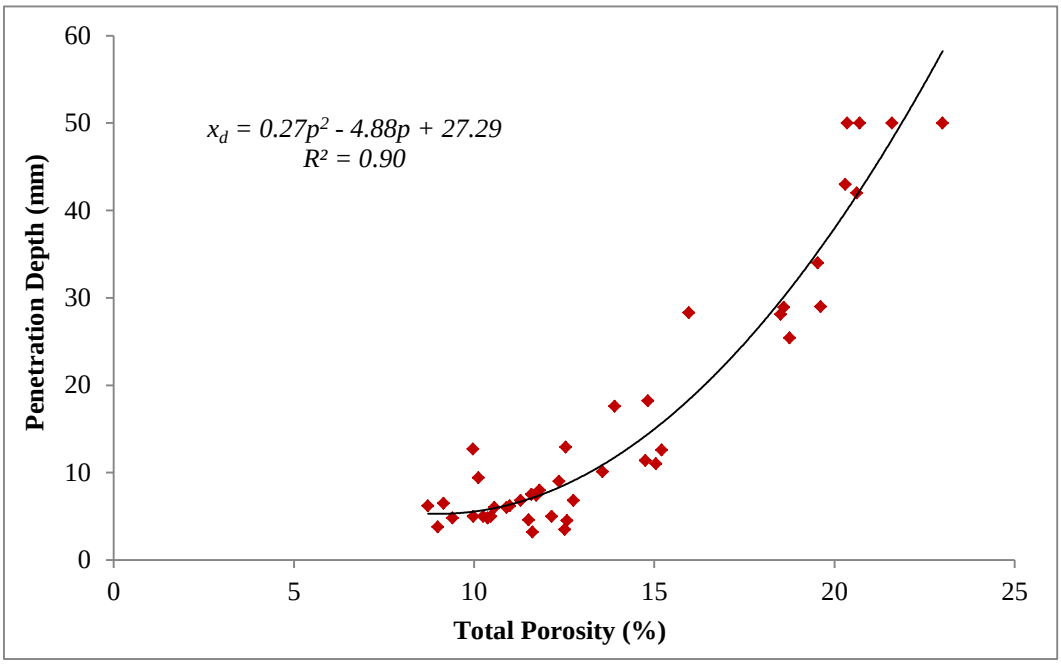

Figure 4.5: Correlation between total porosity and penetration depth of concrete.

. This equation accounts for the duration of the test and the temperature range in the anolyte solution.

$$D = \frac{0.0239(273+T)l}{(V-2)t}\left(x_d - .0238\sqrt{\frac{(273+T)l\,x_d}{(V-2)}}\right) \qquad (Eq.\,4.1)$$

where, D is the non-steady-state chloride migration coefficient ($\times 10^{-12}$ m^2/s), V is the applied voltage (V), T is the average value of initial and final temperatures in the anolyte solution (°C), l is the thickness of the specimen (mm), x_d is the average value of penetration depth (mm), and t is the time (h).

The relationship between the migration coefficient and porosity of specimens for the range of the mixture designs tested herein is shown in Figure 4.6. This relationship could be

described by a second degree polynomial relationship obtained by curve fitting with a coefficient of determination (R^2) of 0.93, indicating a strong association between the two datasets. Bassuoni *et al.* (2006) reported a similar relationship between the migration coefficient and total porosity of concrete on a different range of mixture designs incorporating corrosion inhibitors, which affect the ionic concentration of pore solution, without changing the physical features of pore structure.

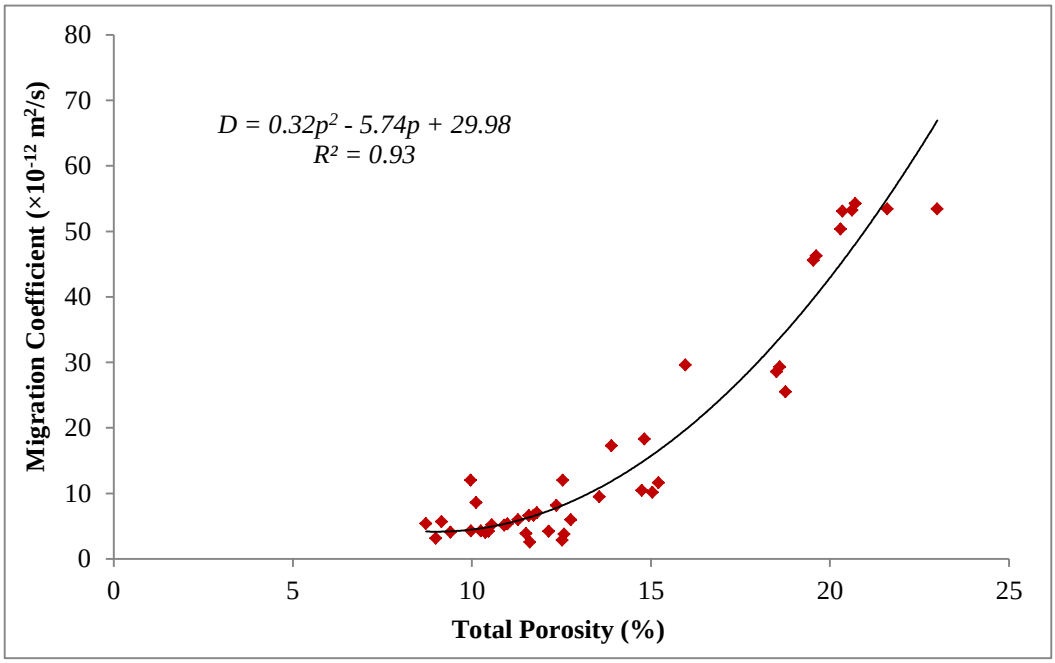

Figure 4.6: Correlation between total porosity and migration coefficient of concrete.

4.3. Relationship among Resistivity, Penetrability and Porosity

The trends discussed in the resistivity and penetrability sections suggest that a tripartite relationship exists among SR, migration coefficient (penetrability) and porosity of concrete as depicted in the nomogram shown in Figure 4.7. Since the SR technique is more suitable (and quicker) for field applications, the tripartite relationship focused on correlating SR (rather than BR) to penetrability and porosity of concrete. The nomogram consists of two parts: the top part

represents the relationship between the SR and migration coefficient for the range of the mixtures tested herein, and the bottom part represents the correlation between the porosity and migration coefficient (discussed in the penetrability section) for the same range of mixtures. For the top part, an inversely power relationship between SR and migration coefficient with an R^2 of 0.85 was obtained for the wide range of concrete mixture designs tested herein; concrete with higher resistivity had lower migration coefficient and vice versa, which is in good agreement with previous studies (Sengul, 2014; Liu *et al.,* 2015). The non-linearity of this relationship might be linked to the dependence of SR on the concentration of all ionic species in the pore solution of cementitious matrix, while the migration coefficient is mainly affected by the concentration of chloride ions penetrating into concrete. Therefore, based on the SR value of concrete, its migration coefficient and porosity (physical penetrability) can be obtained from the nomogram, where the effect of electrolysis bias is discounted. Resistivity is a simple, fast and robust technique that can be easily applied on field or laboratory concrete; if it is used in conjunction with the nomogram shown in Figure 4.7, the physical characteristics of pore structure of concrete can be projected. While resistivity is an electrical property that indicates ionic mobility within the pore network of concrete, which for example controls the rate of corrosion propagation of embedded reinforcement, the migration coefficient and porosity express the ease and rate of ingress of chloride ions and fluids into concrete, which are relevant to key durability issues of concrete such as corrosion initiation, freezing-thawing damage and chemical attack. Based on the previous discussion about the effects of mixture design variables (w/b, air-entrainment, SCMs, type of cement) implemented in this study on the resistivity and penetrability of concrete and correlations established herein, this nomogram can be segmented

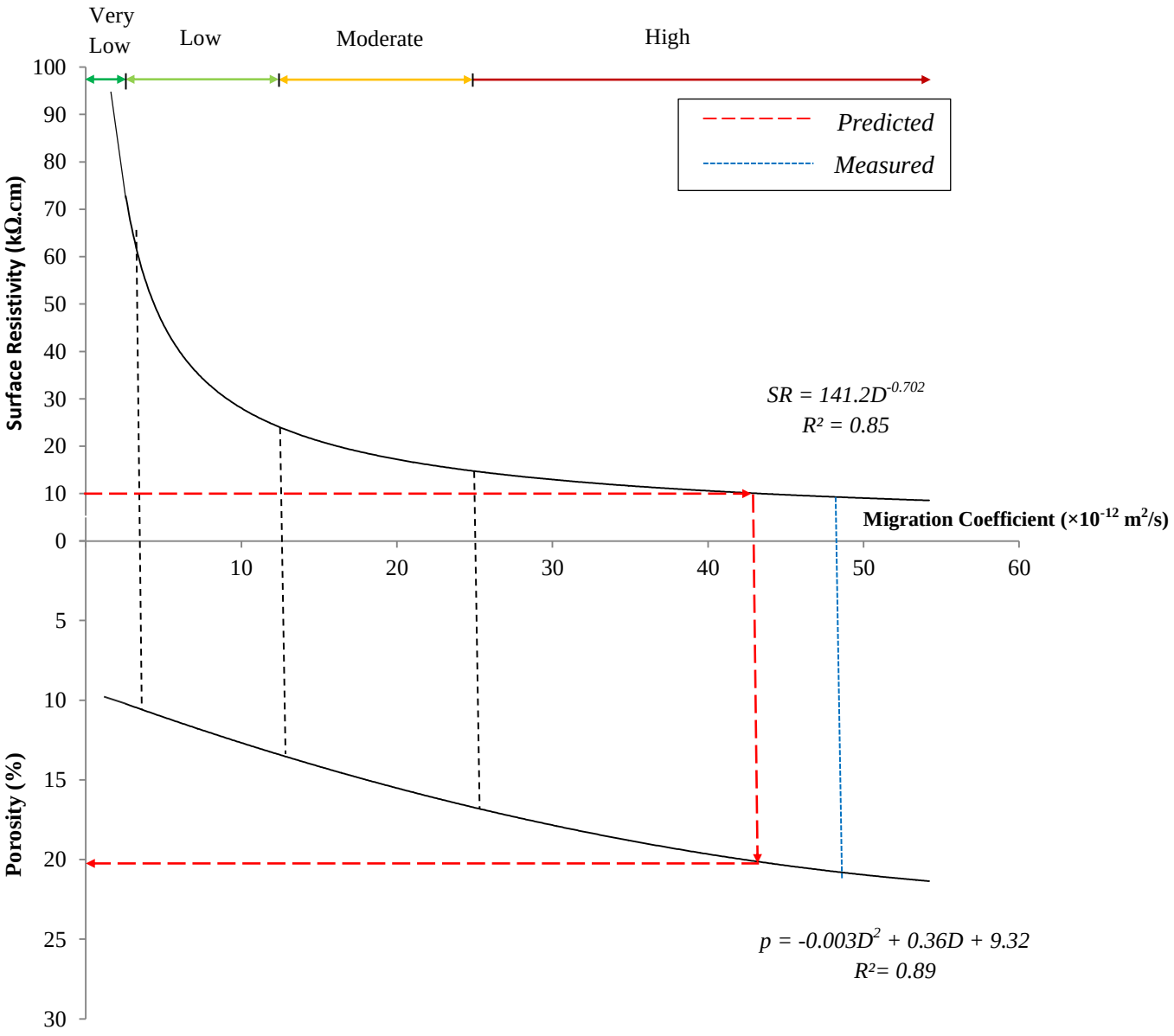

Figure 4.7: Tripartite relationship (nomogram) among migration coefficient, surface resistivity and porosity of concrete.

into four regions corresponding to the penetrability classifications listed in Table 4.5. This proposed classification collectively categorizes concrete based on its SR, migration coefficient and porosity. For example, it can be used by transportation agencies to project the overall quality of concrete based on multiple performance criteria rather than using one indicator, which only

reflects a single property or affected by shortcomings such as electrolysis bias. Examples for use of this nomogram and classification table for the quality inspection and condition assessment of newly constructed and aging concrete pavement are given in the next section.

4.4. Exemplar Application of the Nomogram

The proposed nomogram and classification table were applied to five field cores extracted from newly constructed and aging pavement sections in Winnipeg, Canada to gauge their reliability and practicality for evaluating the condition of field concrete. The cores were extracted at or in the vicinity of transverse joints, as such regions are typically critical and vulnerable to

Table 4.5: Proposed penetrability classes based on surface resistivity, migration coefficient and porosity of concrete.

Penetrability Classification	**Surface Resistivity (kΩ.cm)**	**Migration Coefficient ($\times 10^{-12}$ m^2/s)**	**Porosity (%)**
High	< 15	> 25	> 16.5
Moderate	15 – 25	12 – 25	13.5 – 16.5
Low	25 – 65	3 – 12	10.5 – 13.5
Very Low	> 65	< 3	< 10.5

deterioration. For jointed plain concrete pavement, City of Winnipeg (COW) specifies a ready mix concrete with target performance of 35 MPa and meeting a class of exposure C-2 (plain concrete subjected to chlorides and freezing-thawing) according to CSA A23.1 (CSA A23.1, 2014). The binder typically comprises General Use (GU) portland cement and fly ash (Class F), and the w/b is in the range of 0.35 to 0.40. The COW construction specifications for jointed plain concrete pavements (CW 3310-R15, 2014) permit replacement of GU cement with up to 15% Class F fly ash. A chemical air-entraining admixture complying with ASTM C260 (ASTM

C260, 2010) is used in concrete to achieve a fresh air content of 5 to 7%. After casting, concrete pavement is covered by a curing compound made of high-grade hydrocarbon resins in a water-based emulsion conforming to ASTM C309 (ASTM C309, 2012) Types 1, 2 and 1-D, Class B.

SR, RCPT and MIP tests were conducted on the field cores in conformance to the same procedures/conditions described earlier in the methodology section. The field core designations were selected according to the age of the cores, where 'O' stands for aging/old concrete (20 years), "R" stands for recently constructed concrete (one year), and (N) stands for newly constructed concrete (28 days). Based on the measured SR, the migration coefficient, porosity and penetrability class of the field cores were predicted from the nomogram and classification table, and compared to the measured ones, as listed in Table 4.6. An example for determining these values from the nomogram (red lines), compared to the experimental values (blue line) is shown in Figure 4.7 for an SR of 10 kΩ.cm (Core O2). From Table 4.6, it can be noted that the coefficient of migration and porosity values for field cores predicted from the nomogram are close to the experimental ones. Due to the inherent heterogeneity of concrete and uncertainty of a multitude of factors including materials proportions, exposure conditions, and error ranges in the experimental methods used to establish the nomogram, it would be unrealistic to draw a reliable comparison based on the crisp (deterministic) values of the predicted and measured migration coefficients and porosities. Alternatively, such comparison should be made based on matching ranges/zones of penetrability classification in which the concrete are located, which account for variability of results and uncertainty. In this application example, all the predicted penetrability classes mesh with the ones projected by the experimental values, i.e. they lie within the same range or penetrability zone, despite some differences in the crisp values of migration coefficient and porosity (Table 4.6). In addition, the nomogram has correctly classified aging concrete (O1,

O2), which has been in service for 20 years under conditions of freezing-thawing and de-icing salts, in the high penetrability classification, while the newer concrete (N1, N2 and R) has been reasonably classified in the moderate to low penetrability zones. This transition from moderate (N1 and N2 at 28 days) to low (R at one year) conforms to the well-documented effect of Type F fly ash, which is a slow reactivity pozzolanic material that densify the microstructure of concrete with age (Mehta and Monteiro, 2014). This penetrability classification has informatively assisted the COW to undertake full depth repair in the pavement sections of O1 and O2, and ensure the quality of concrete in the new pavement sections represented by (R, N1 and N2). It is worth noting that such a tripartite relationship exists irrespective of the age of concrete at the time of testing (e.g. 20 years, or 28 days). In other words, at any given SR range, there are corresponding ranges of migration coefficient and porosity, from which the penetrability class of concrete can be obtained.

Table 4.6: Measured vs. predicted penetrability classification of field cores.

Field Cores	**Surface Resistivity (kΩ.cm)**	**Measured**			**Predicted**		
		Migration Coefficient ($\times 10^{-12}$ m^2/s)	**Porosity (%)**	**Location in Nomogram**	**Migration Coefficient ($\times 10^{-12}$ m^2/s)**	**Porosity (%)**	**Penetrability Classification**
O1	13	38.2	20.1	High	30	17.5	High
O2	10	48.7	21.7	High	44	19.3	High
R	28	7.6	13	Low	10	12.6	Low
N1	22	17.9	12.3	Moderate	13.8	13.7	Moderate
N2	23	18.2	12.8	Moderate	13.2	13.6	Moderate

Chapter 5 : Results and Discussion for Functionality of Zinc Anodes in Repaired Concrete

5.1. Resistivity

The average surface resistivity (SR) of duplicate slabs without anodes for the repair patches measured at the end of each wetting cycle up to 12 months are listed in Table 5.1. A conversion factor of an average value of 2.33 has been applied according to the results previously discussed in Chapter 4 to obtain the bulk resistivity (BR) from the SR measurements to monitor the change of resistivity over time for the repair sections (Table 5.1). The results conform to the well-documented trend of the effect of the w/b and SCMs on the physical characteristics of the pore structure of concrete, and in turn its electrical resistivity. For example, increasing the w/b from 0.3 (R_{ii}) to 0.5 (R_i) led to a marked decrease (30%) in the BR due to the higher porosity and enhanced pore continuity of the cementitious matrix, as discussed in Chapter 4. Compared to the single binder mixture (R_{ii}; w/b = 0.3), the addition of 8% silica fume in mixture R_{iii} led to a significant increase in the BR of about 37.5 % owing to the densification of the pore structure by the pozolanic reactivity of silica fume, producing more cement gel and blocking the pore channels for ions to go through, in addition to binding ionic species in the cementitious matrix, i.e. reducing the conductivity of the matrix (Lataste, 2010). Furthermore, the results of the high resistivity concrete tested herein (R_{iv}) highlight the predominant role of ultrafine pozzolans such as nano-silica in significantly refining and densifying the pore structure of the matrix, and thus reducing its penetrability and electrical resistivity, espeically at early-age. The increasing values of resistivity with time (Table 5.1) for all the mixtures are attributed to the progression of the hydration process in the repair patches, especially with the exposure regime adopted in this

study, which comprised wetting cycles with pure water stimulating renewed curing of concrete (in addition to aggravating the corrosion of bars). It is well-documented that during the hydration process, the capillary pores are gradually filled up with hydration products forming denser microstructure, so the connectivity of the matrix is reduced. Consequently, both ions and current transport are discounted, which correspondingly increase the electrical resistivity of concrete. Such process can be further enhanced by the incorporation of SCMs, as discussed earlier, which is evident in mixtures R_{iii} and R_{iv}, or the through the use of polymeric modifiers (non-conductive organic compounds enhancing the tortuosity of pore structure) as shown by the very high resistivity values of mixture R_v.

Table 5.1: Surface and bulk resistivity of the repair patch of slabs without anodes at one and twelve months.

Resistivity Category	**Surface Resistivity (kΩ.cm)**			**Bulk Resistivity (kΩ.cm)**		
	1 Month	12 Month	Average	1 Month	12 Month	Average
R_i	13	38	25	5	15	10
R_{ii}	24	52	38	9	20	14.5
R_{iii}	53	73	63	23	32	28
R_{iv}	90	--[*]	--	35	62[**]	48.5
R_v	--	--	--	98[**]	120[**]	109

[*] R_{iv} reached the maximum capacity of the apparatus (99 kΩ.cm) after 3 months.
[**] Obtained directly from concrete cylinders used for the intial readings at one month.

5.2. Total Current

The current density, which reflects the change of the total current originating from the anode normalized by the surface area of the steel bars with time at different anode spacing (25, 100, and 250 mm) are shown in Figures 5.1(a)-(c). The total current from the anode (without normalization) was almost equal to the summation of the currents in the individual bars embedded in the three sections; this verified that the anode's current had been well distributed among the three sections without significant losses. Since the trends of current measurements

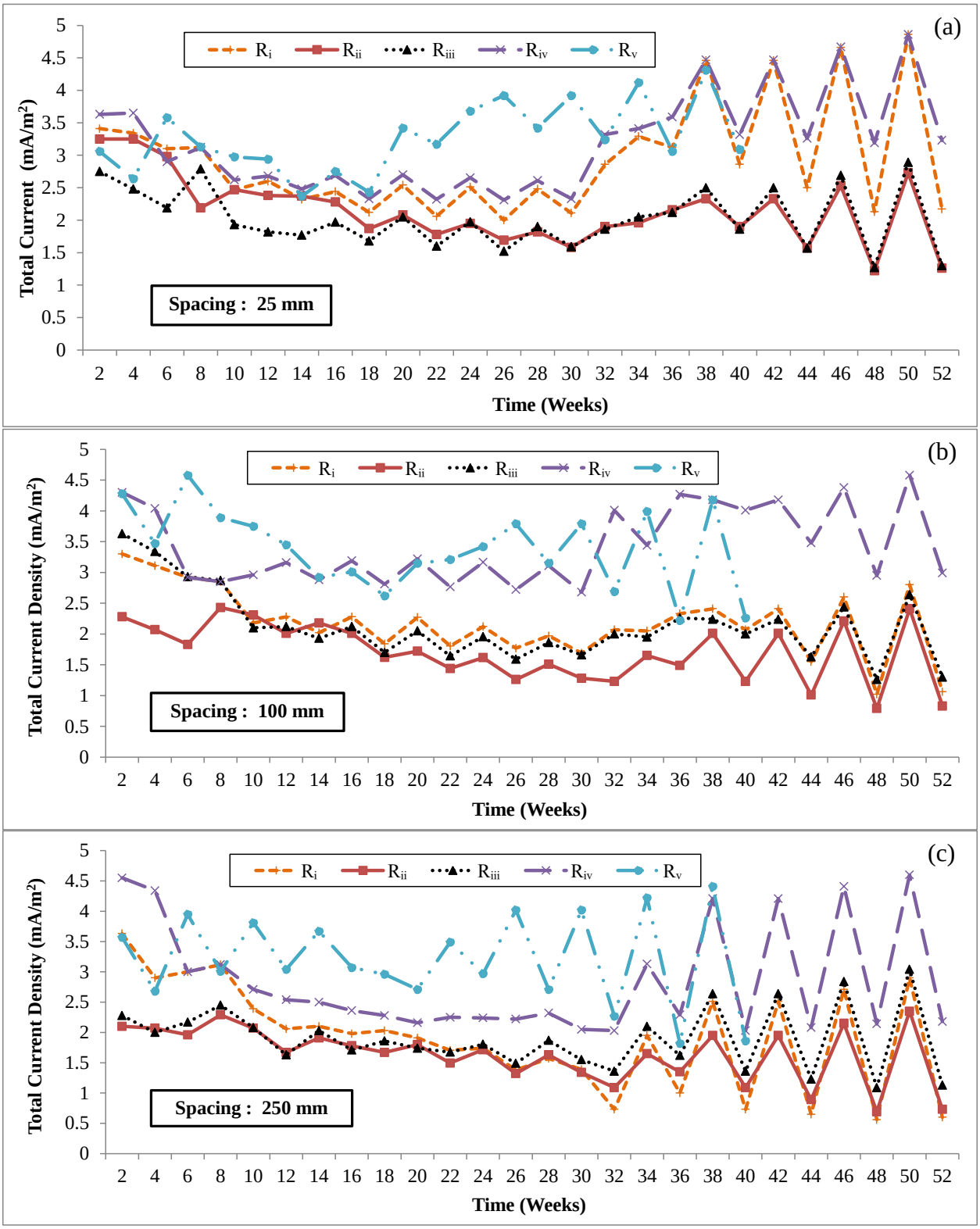

Figure 5.1: Change in the current density of the zinc anodes in the repair sections mounted at a spacing of: (a) 25 mm, (b) 100 mm, and (c) 250 mm.

were almost similar at all anode's spacing, only the currents in the R_{iii} slabs at 25 mm spacing are shown in this section (Figure 5.2) as an example, and the current measurements for the other resistivity and spacing values are shown in Appendix A. The current density increased and reached its peaks when the slabs were wet, which could be explained by the ease of mobility of ionic species through the pore structure with moisture ingress. In the beginning of exposure, the maturity of the concrete was still low, resulting in high current densities (2 to 4.5 mA/m^2) for all resistivity classes and anode spacing. However, during the drying cycles, these values decreased with time due to the development of microstructure (i.e. higher maturity), and increasing anode-to-steel resistance associated with loss of water to the surrounding environment (Sagues and Powers, 1994), which directly affected the density of the current generated from the anode. On the other hand, during the wetting cycles, the current densities showed an increase after 32 weeks in comparison to the values at drying cycles due to increasing the fraction of the anode surface in direct contact with the electrolyte solution upon wetting, resulting in an increase in current delivery.

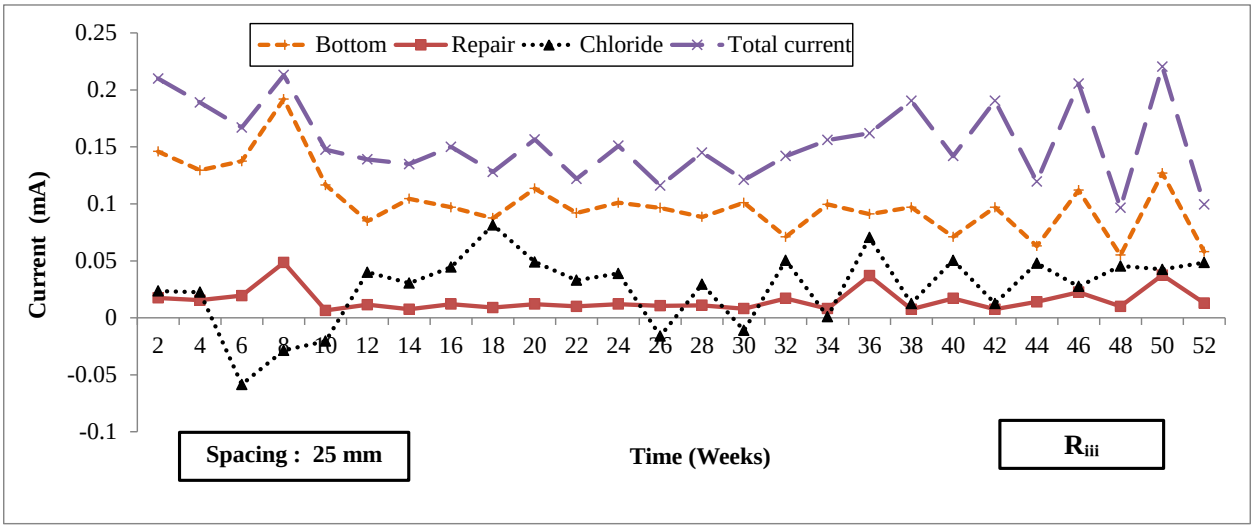

Figure 5.2: Change in the current over time in the three sections of concrete slabs and the total current from the zinc anodes (R_{iii}; spacing of 25 mm).

Eventually, the current from the zinc anodes has remained above the level (0.2 to 2 mA/m^2) believed to be adequate for cathodic prevention, which alludes to the functionality of zinc anodes up to 52 weeks even in high resistivity concrete (up to 100,000 Ω-cm).

The current trends were assessed by the analysis of variance (ANOVA) method at a significance level (α) of 0.05, as shown in Table 5.2. According to Montgomery (2012), exceeding the F_{cr} value of an *F*-distribution density function indicates that the variable tested has a significant effect on the average results. The significant effect of resistivity of concrete was statistically supported by ANVOA for the total current results over 52 weeks, since changing the electrical resistivity of the repair section at a spacing of 25 mm yielded *F* value of 14.2, which was greater than the F_{cr} of 5.2. The trends of the current measurements [Figures 5.1(a)-(c)] were mixed with the resistivity of the repair sections (Table 5.1). In some case, repair concrete with higher resistivity had lower current density and vice versa. For example, increasing the resistivity of the repair sections, in which the anodes were embedded at a spacing of 25 mm, from 5000 to 25,000 Ω-cm led to a reduction of 29% in the total current density of the zinc anode after 52 weeks. This may be attributed to restricted migration of the ionic current through the electrolyte solution in capillary pores. However, due to the effect of the anode spacing, these trends changed for the 100 and 250 mm spacing. For example, increasing the resistivity of the repair section at spacing of 100 and 250 mm from 5000 to 25,000 Ω-cm showed approximately 18 and 47% increase in the total current density, respectively, over 52 weeks.

It is worth mentioning that this trend was invalid for the high resistivity repair concrete (R_{iv} and R_{v}). Actually, increasing the resistivity class of repair concrete to 50,000 (R_{iv}) and 100,000 (R_v) Ω-cm led to an inverse effect since the total current density generally increased with time, irrespective of the spacing of the anode, as depicted in Figures 5.1(a)-(c). This might

be attributed to the distribution of the current among all bars embedded in the slabs. For example, a comparison between R_{ii} and R_v slabs in terms of the current distributed from the anode to all steel bars in the three sections (bottom, chloride contaminated, and repair) is shown in Figures 5.3(a)-(b) at a spacing of 25 mm. This figure indicates marginal differences between the R_{ii} and R_v slabs, except for the current flowing to the bars embedded in the chloride contaminated section. For the R_{ii} slab, this current remained mostly negative over the time of exposure.

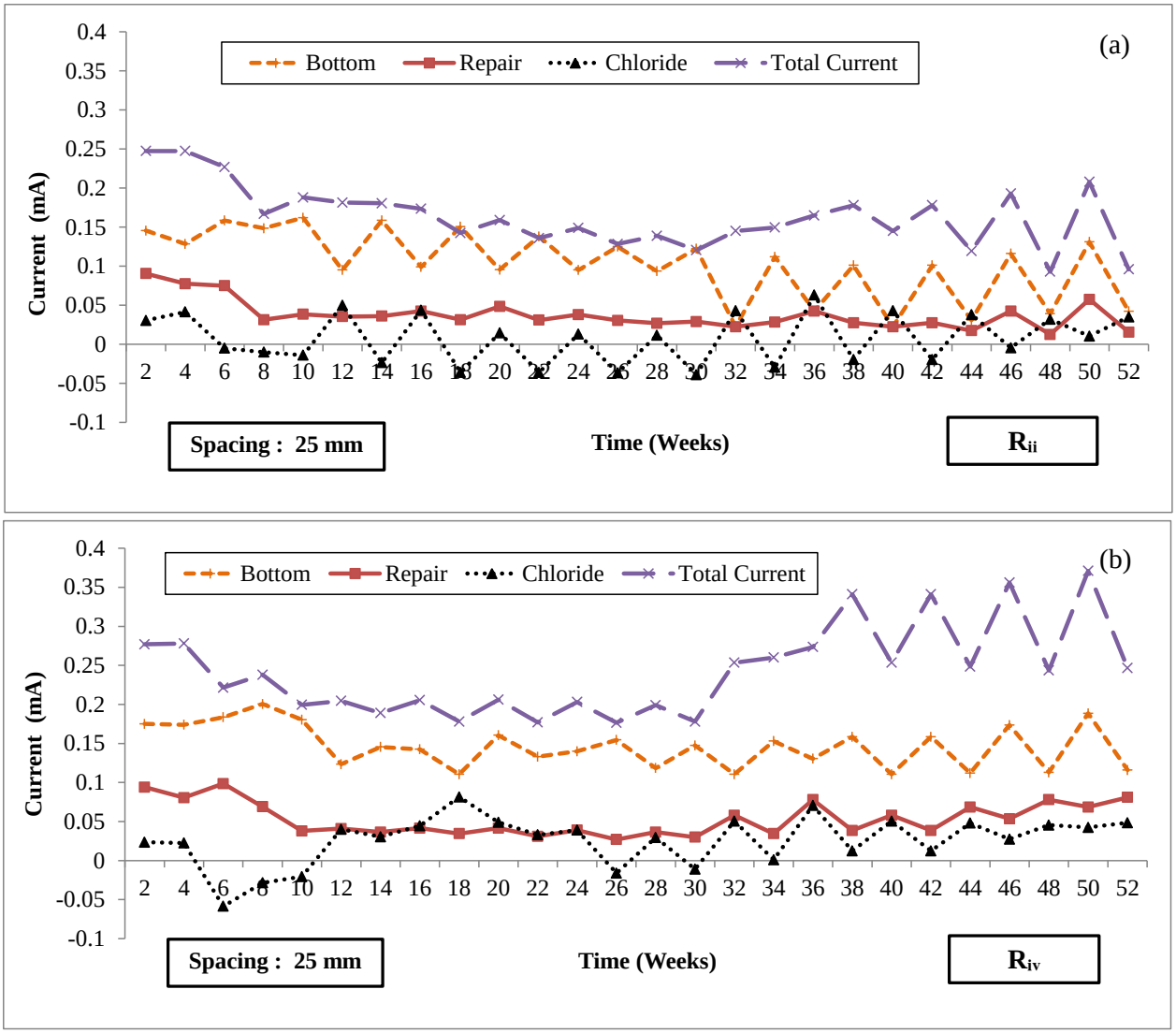

Figure 5.3: Comparison of the distribution of the current originating from the zinc anode to steel bars embedded in three different sections for: (a) R_{ii}, and (b) R_{iv} slabs.

A negative current indicates an opposite direction of electron flow (Giorgini, 2014), i.e. the steel bars in this section were not receiving current from the anode. For clarification, schematic diagram of a cross section from a slab specimen with anode is presented in Figure 5.4 to illustrate the proposed current flow paths in each slab. Figure 5.4 shows the typical case expected for the current path in slabs with anode, flowing from the sacrificial anode to the three sections as reflected by the positive current sign. Also, it shows the direction of the negative current originating from the chloride contaminated section to the other sections (blue colored arrow), which may oppose the path of the main current from the anode, and thus discount the intensity of the total current generated from the zinc anode, as proposed in Figure 5.4.

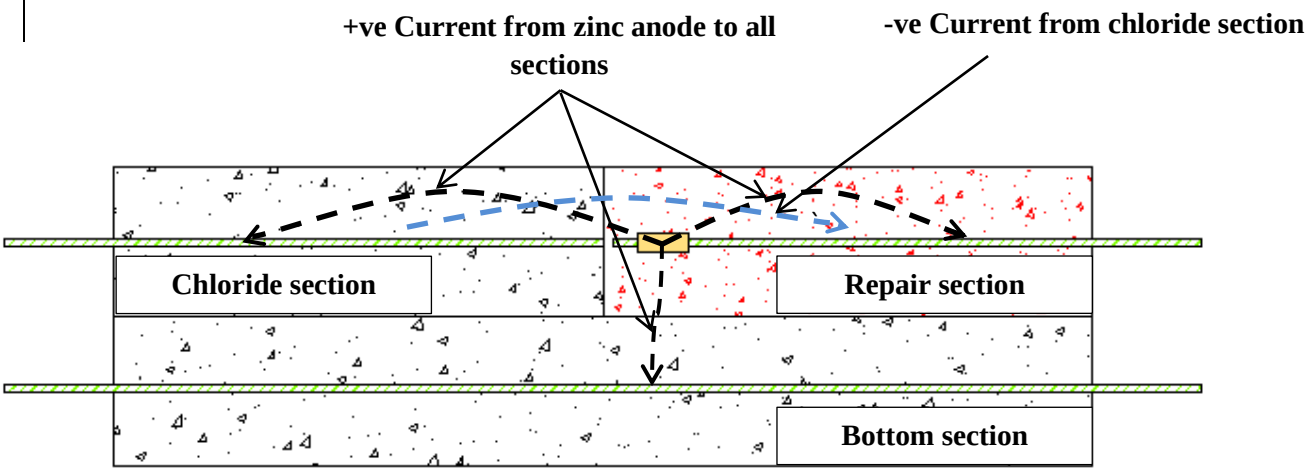

Figure 5.4: Schematic diagrams of a cross section for a slab specimen with anode showing the typical current flow from the anode to all bars and the negative current from the chloride contaminated section.

In the slabs without anode, it was found that changing the resistivity class of the repair section had a direct effect on the corrosion cells formed between the chloride contaminated section (behaved as an anode), and the other sections (behaved as cathode). As depicted in

Figure 5.5, increasing the resistivity of the repair section from 5,000 to 100,000 Ω.cm consistently led to reducing/restricting the corrosion cells (negative current) flowing from the chloride contaminated section. This may be ascribed to the test set-up adopted in this study, where the existence of any high resistivity material in such system will directly affect the current circulating inside the slab since it is a closed circuit. Therefore, the current fed by the anode and received by bars located in the bottom section in the high resistivity slabs (R_{iv}) was higher than that in the bottom section of the low resistivity (R_{ii}) slabs. This is substantiated by the trend obtained in Figure 5.3(a)-(b), where the bars located in the low resistivity concrete (R_{ii}) were more affected by the macro-cell corrosion formed between the bars in the chloride contaminated section and the ones embedded in the other sections, which led to reducing the intensity of the total current generated from the anode.

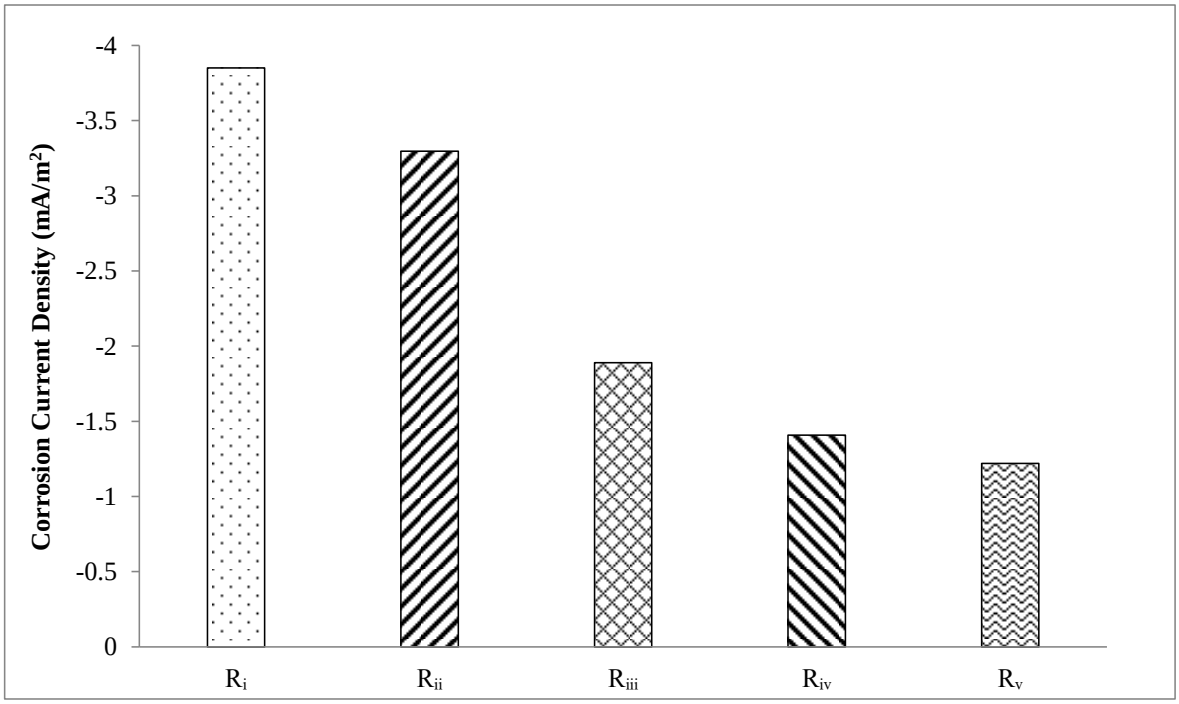

Figure 5.5: Average current of slabs without anode generated from the anodic region (chloride contaminated section) to other sections.

For the lowest resistivity class (R_i), increasing the spacing of the zinc anodes to 250 mm led to a reduction in the total current density [Figures 5.6(a)-(e)], which might be ascribed to the longer distance that ionic current would migrate to protect the most susceptible location to corrosion (boundary line). However, for the resistivity classes, this trend diminished due to the convergence of currents at similar magnitudes, especially during the wetting cycles (Figure 5.6). This was statistically supported by the ANOVA for the total current results over 52 weeks, as changing the spacing from 25 to 250 mm of R_{ii} slabs yielded *F* value of 4.7, which was less than the F_{cr} of 9.6, indicating that the effect of this parameter was statistically insignificant.

Table 5.2: ANOVA for the average values of the total current density results over 52 weeks.

Parameter	**Variable**	**F**	**F_{cr}**	**Effect**
Total Current Density	Resistivity of the repair section at a spacing of:			
	25 mm	14.2	5.2	Significant
	100 mm	7.5	5.2	Significant
	250 mm	17.4	5.2	Significant
	Spacing of zinc anode of:			
	R_i slabs	7.1	9.6	Insignifica
	R_{ii} slabs	4.7	9.6	Insignifica
	R_{iii} slabs	0.39	9.6	Insignifica
	R_{iv} slabs	0.94	9.6	Insignifica
	R_v slabs	0.21	9.6	Insignifica

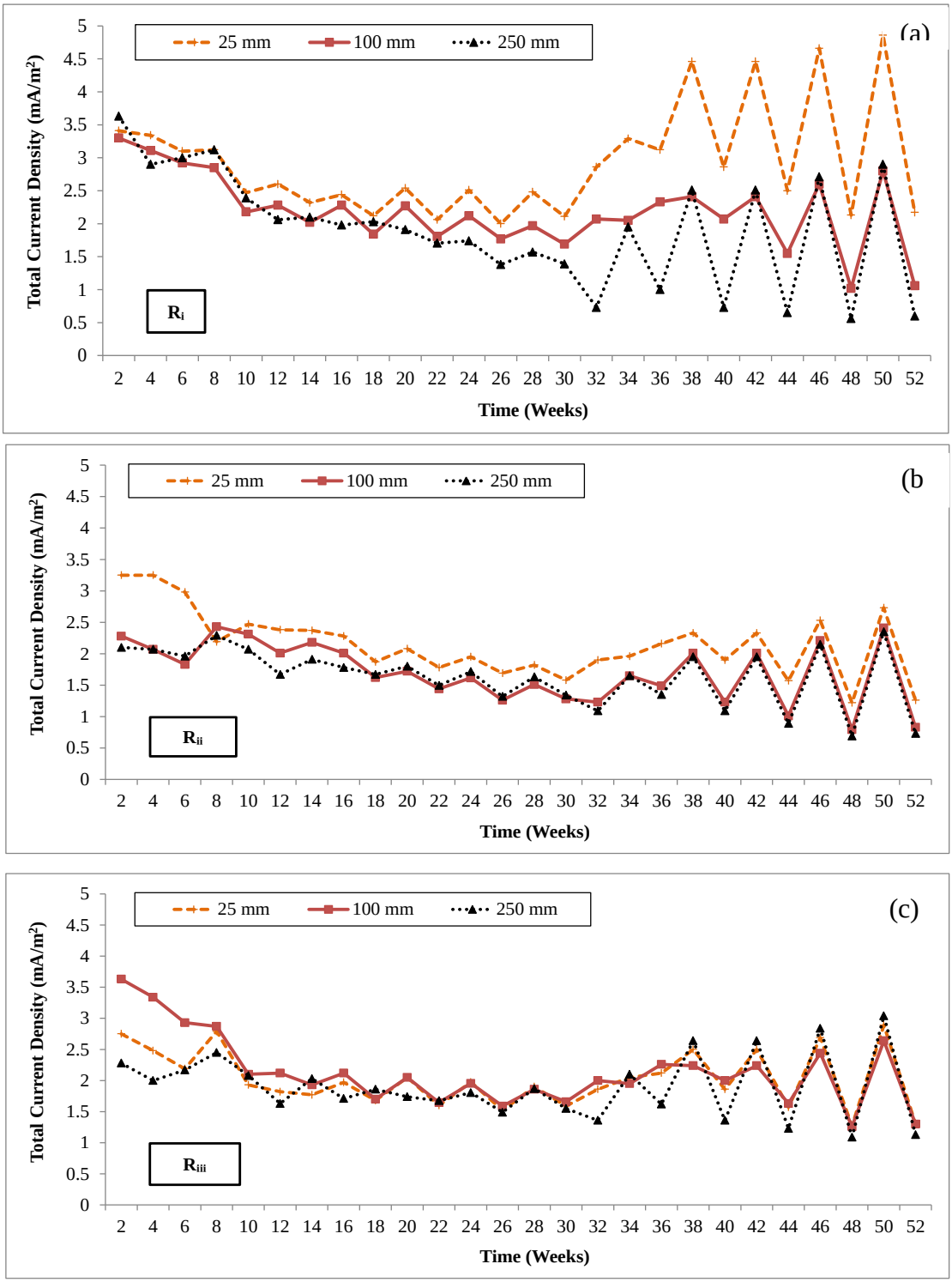

Figure 5.6: Change in the current density of the zinc anodes considering the effect of changing the spacing of the anode: (a) R_i, (b) R_{ii}, (c) R_{iii}, (d) R_{iv} and (e) R_v slabs.

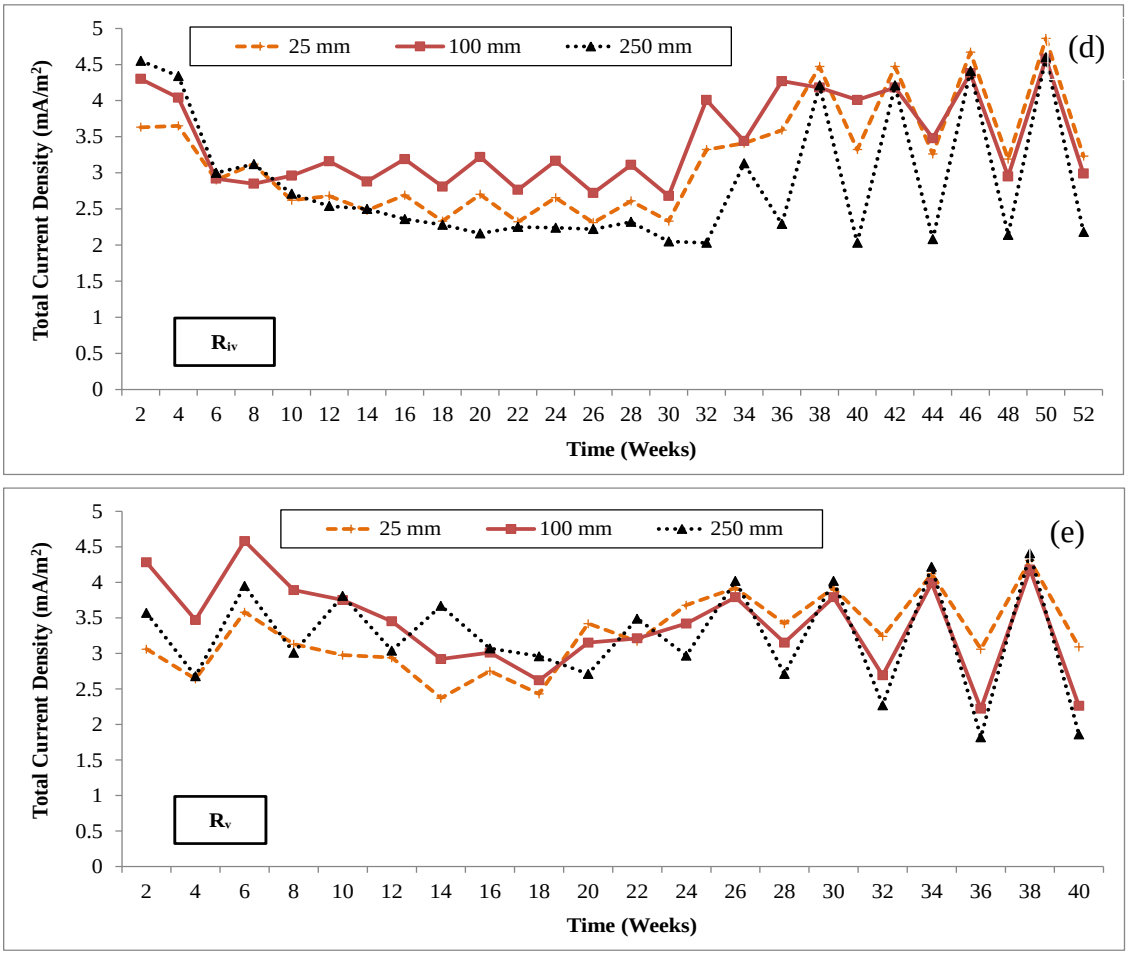

Figure 5.6 (Cont'd): Change in the current density of the zinc anodes considering the effect of changing the spacing of the anode: (a) R_i, (b) R_{ii}, (c) R_{iii}, (d) R_{iv} and (e) R_v slabs.

5.3. Half-Cell Potential

The change of potentials for the bars in the repair and chloride contaminated sections of the control (without anodes) R_i, R_{ii}, R_{iii}, R_{iv}, and R_v slabs with time are shown Figures 5.7(a)-(b). For these slabs, the bars in the repair sections showed potential readings starting at -296, -248, -236, -184, and -255, and ended with -128, -59, -143, -47, and -214 mV vs CSE, respectively. As expected, the average of these ranges are -212, -154, -189, -116, and -234, respectively, which were remained mostly higher (more positive) than -200 mV vs CSE [Figure 5.7(a)], indicating that the likelihood of corrosion activity of steel bars in the repair sections was less than 10%,

according to the potential thresholds stipulated in the ASTM C876 (2009). The potentials for all resistivity classes showed a progressively ascending trend with time owing to the continual hydration of concrete as reflected by the increase in resistivity with time (Table 5.1). Also, the significant effect of changing the resistivity was shown by ANOVA for the potentials

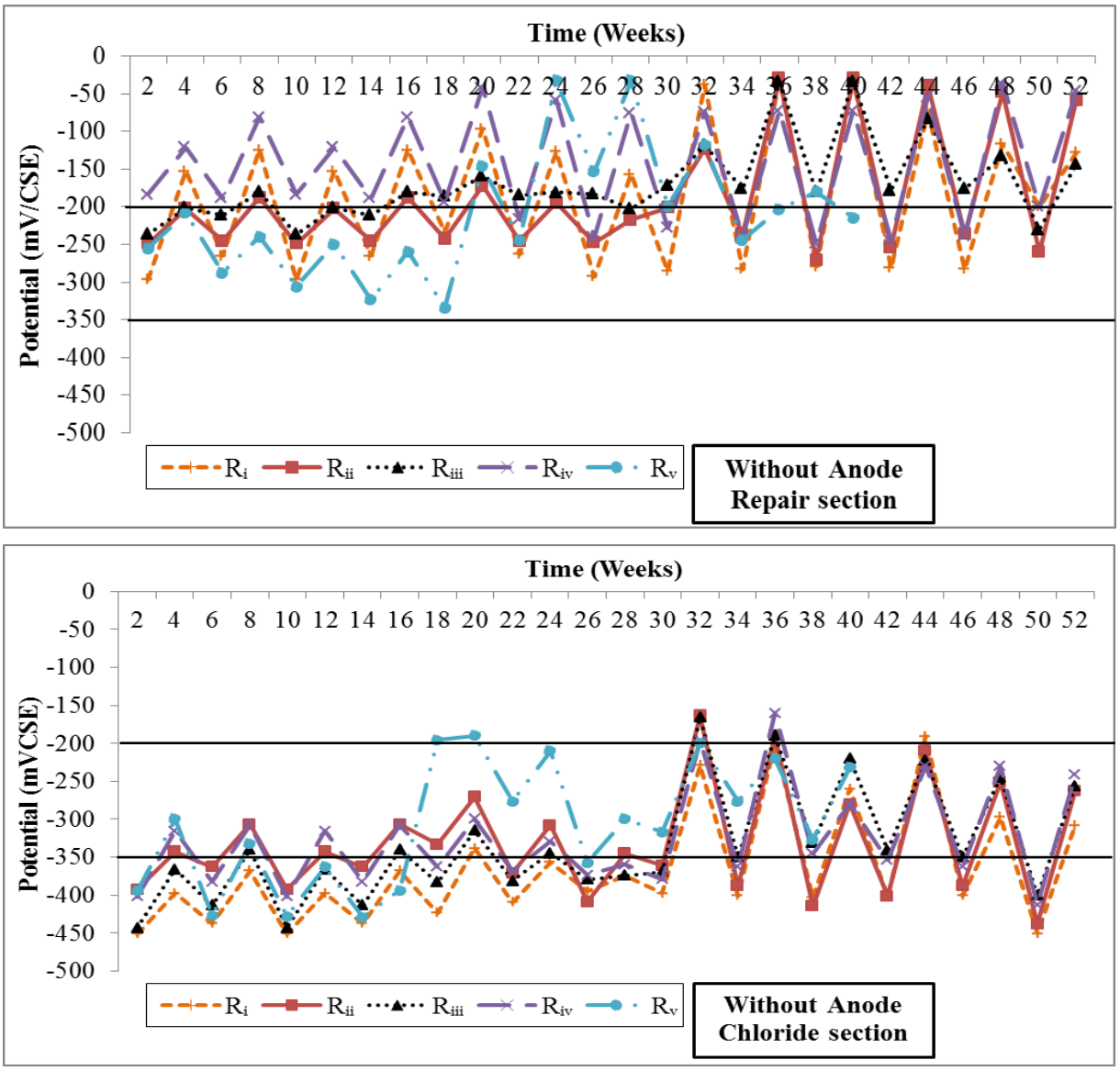

Figure 5.7: Average potential of steel bars in slabs without anodes: (a) repair, and (b) chloride contaminated sections.

results of the repair section in the slabs without anodes, as changing the resistivity of the repair patch from R_i to R_{iv} yielded *F* value of 5.7, which was greater than F_{cr} of 3.1 (Table 5.3).

On the other hand, the bars in the chloride contaminated sections [Figure 5.7(b)] yielded more negative values than that of the corresponding ones in the repair sections. It should be emphasized that the contaminated sections in all slabs were prepared from normal concrete with a 28-day resistivity of approximately 5,000 Ω-cm, and it seems that changing the resistivity of the repair sections did not significantly affect the corrosion activity in the contaminated sections as the trends were generally comparable in Figure 5.7(b). Increasing the resistivity of the repair patches from R_i to R_{iv} had an *F* value of 2.5, which was less than the F_{cr} of 3.1 (Table 5.3), indicating insignificant differences among the potential results of the chloride contaminated sections for slabs without anodes. In the first 22 weeks of exposure, the average potential measurements in the contaminated sections were mostly more negative than -350 mV vs CSE for all resistivity values. Thus, as expected, the likelihood of corrosion activity in this section was high [more than 90% according to ASTM C876 (2009)]. However, the potentials measurements, after 22 weeks, showed an increase with time towards the range where the corrosion activity is uncertain [between -200 and -350 mV vs CSE according to ASTM C876 (2009)] due to the increase of resistivity of concrete with time. Because of the differences in potentials between the repair and chloride contaminated sections, the boundary zone might be susceptible to the incipient anode phenomenon (halo effect) as intended in the design of the test set-up.

To assess the functionality of the zinc anodes to control the electrochemical corrosion of bars, the potential measurements after 52 weeks of the chloride contaminated and repair sections

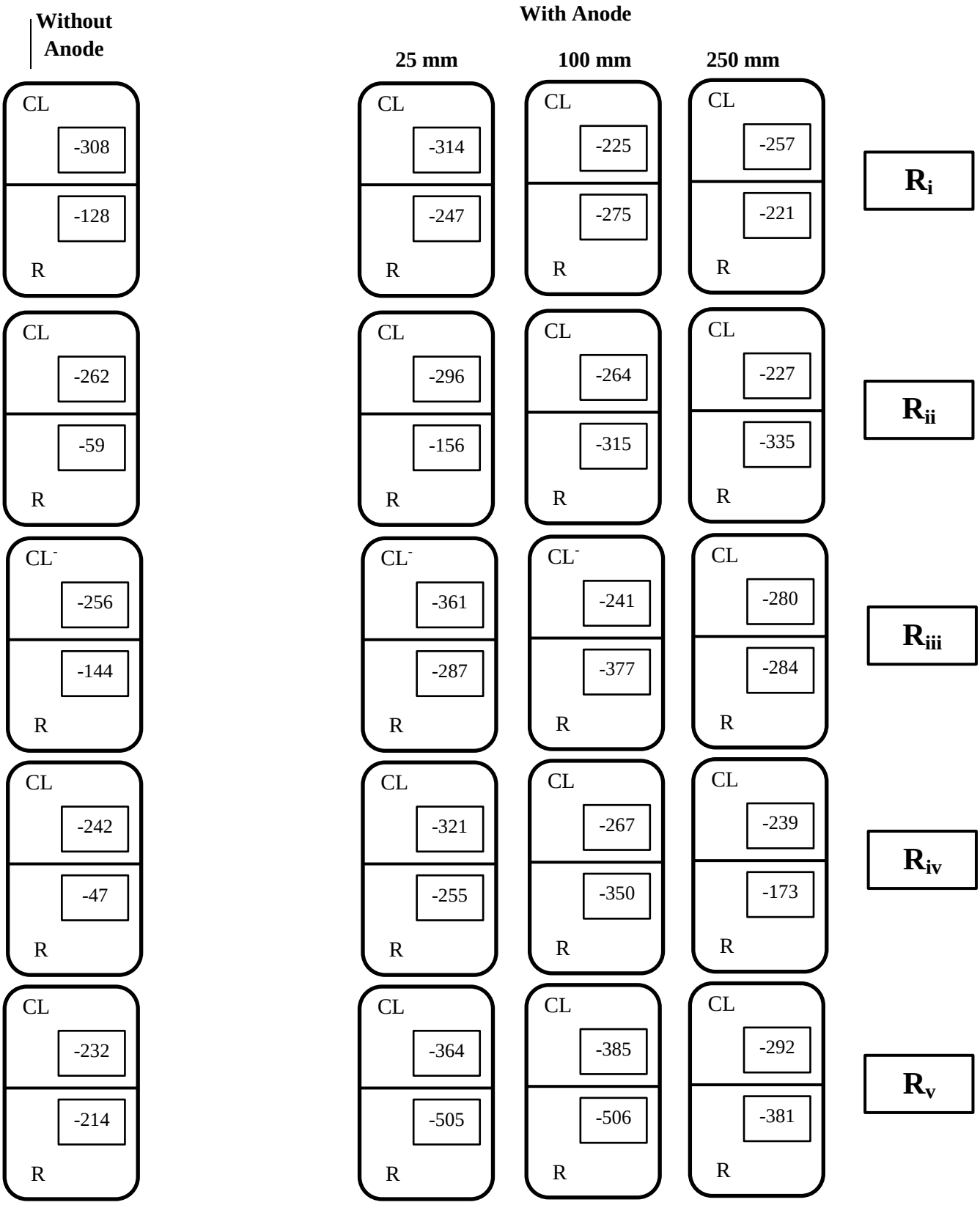

Figure 5.8: The potential of steel bars in slabs without and with anodes for the chloride contaminated and repair sections. (R: repair section, CL: chloride contaminated section)

for the slabs without and with anodes at different resistivity and anode spacing are shown in Figure 5.8. However, the data showed inconsistent potentials between the chloride contaminated and repair sections for the slabs with anodes. It was expected that the repair section should yield

Table 5.3: ANOVA for the potential results over 52 weeks.

Parameter	Variable	F	F_{cr}	Effect
Potential of Repair Section (Without Anode)	Resistivity of the repair section	5.7	3.1	Significant
Potential of Chloride Contaminated Section (Without Anode)	Resistivity of the repair section	2.5	3.1	Insignificant
Potential of slabs without anode	Installing the anode in the repair section at a spacing of:			
	25 mm	15.5	5.3	Significant
	100 mm	7.2	5.3	Significant
	250 mm	7.8	5.3	Significant
Potential of slabs with anode	Resistivity of the repair section at a spacing of:			
	25 mm	17.4	3.1	Significant
	100 mm	40.4	3.1	Significant
	250 mm	5.4	3.1	Significant
	Spacing of zinc anode of:			
	R_i slabs	12.7	4.3	Significant
	R_{ii} slabs	16	4.3	Significant
	R_{iii} slabs	5.2	4.3	Significant
	R_{iv} slabs	7.4	4.3	Significant
	R_v slabs	33.4	4.3	Significant

more negative potentials compared to the chloride contaminated section in the same slab, which was not always the case herein. This might be attributed to the size limitation of the slab configuration, where both sections were affected by the spatial range of the zinc anode resulting in such mixed trends. Thus, a comparison of the average potential for the whole slabs without and with anodes at each resistivity class and spacing may alleviate such an effect, as shown in Figure 5.9. Irrespective of the anode spacing, the data showed that the slabs with anodes yielded more negative potentials in comparison to that of counterpart slabs without anodes, which were -218, -161, -200, -144, and -223 mV vs CSE for the R_i, R_{ii}, R_{iii}, R_{iv}, and R_v slabs, respectively.

The ANOVA results revealed significant differences among the potential measurements for the slabs without and with anodes, irrespective of the resistivity class. For example, installing the anode at a spacing of 25 mm had F value of 15.5 compared to F_{cr} of 5.3 (Table 5.3). This may be ascribed to the polarizing current flowing to the steel from the anode inducing a negative shift in the potential from the original potential in slabs without anode, which links to the total current trends in Figures 1(a)-(c).

In Figure 5.9, it can be observed that increasing the spacing of anode from the end of the bar was accompanied by a consistent reduction in the average potential of steel bars. For example, changing the spacing of the anode in the repair patch from 25 to 250 mm for the R_i, R_{ii}, R_{iii}, R_{iv}, and R_v slabs led to reducing the potentials of steel bars by 14, 7, 13, 28, and 24%, respectively. This can be linked to the polarising current generated from the anode, as observed in Figure 5.6.

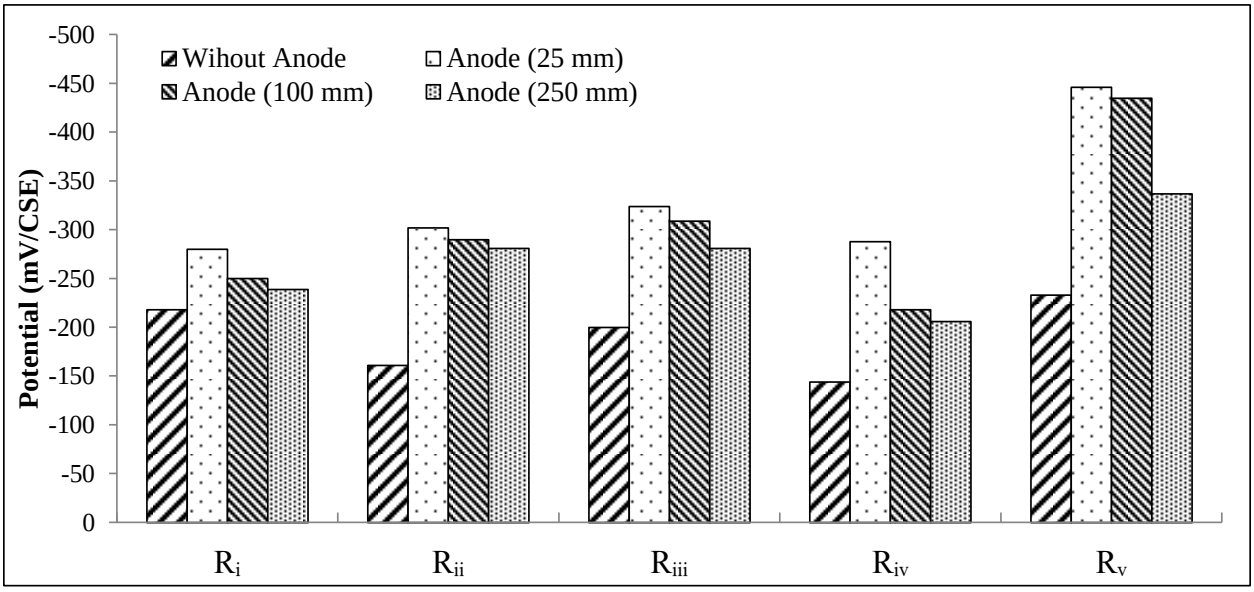

Figure 5.9: Average potentials of steel bars in slabs without and with zinc anodes.

Moreover, these data were evaluated by ANOVA to investigate the statistical significance of changing the resistivity of the repair patch and spacing of the zinc anodes on the potential

measurements for the slabs with anode, as listed in Table 3. For example, changing the resistivity of the repair patch, at a spacing of 100, from R_i to R_{iv} had an *F* value of 40.4, which was larger than the F_{cr} of 3.1 (Table 5.3), indicating the significant effect of this parameter. In addition, increasing the spacing of the anode from 25 mm to 250 mm, at R_i and R_{iii} slabs, yielded an *F* value of 12.7 and 5.2 compared to F_{cr} of 4.3 (Table 5.3), highlighting the significant effect of changing the location of the anodes.

The effectiveness of the cathodic prevention system employed herein was also evaluated by carrying out a depolarization test by disconnecting the anode for a period of 24 h. Slabs from all resistivity classes had a consistent trend in this test. Thus, only the depolarization results of R_{ii} slabs are presented in this section as an example. Figure 5.10 shows the instant off potentials of all steel bars measured immediately after disconnection of the zinc anodes and the potential values measured after 24 h over 52 weeks. The remaining results of this test are shown in Appendix B. According to the commonly used criterion of 100 mV decay (EN 12696-1, 2000), the structure is considered protected if the difference between the instant-off potential and the potential measured after 24 h is higher than 100 mV. Shutting down the anode which was spaced at 25, 100, and 250 mm inside the R_{ii} slabs for 24 h yielded a decay of about -760, -681, and -680 mV, respectively, after 52 weeks. This trend substantiated that the steel bars had been cathodically polarized over the exposure period, irrespective of the location of the anodes inside the repair patch, as reflected by the considerable depolarization shifts after 24 h, as depicted in Figure 5.10.

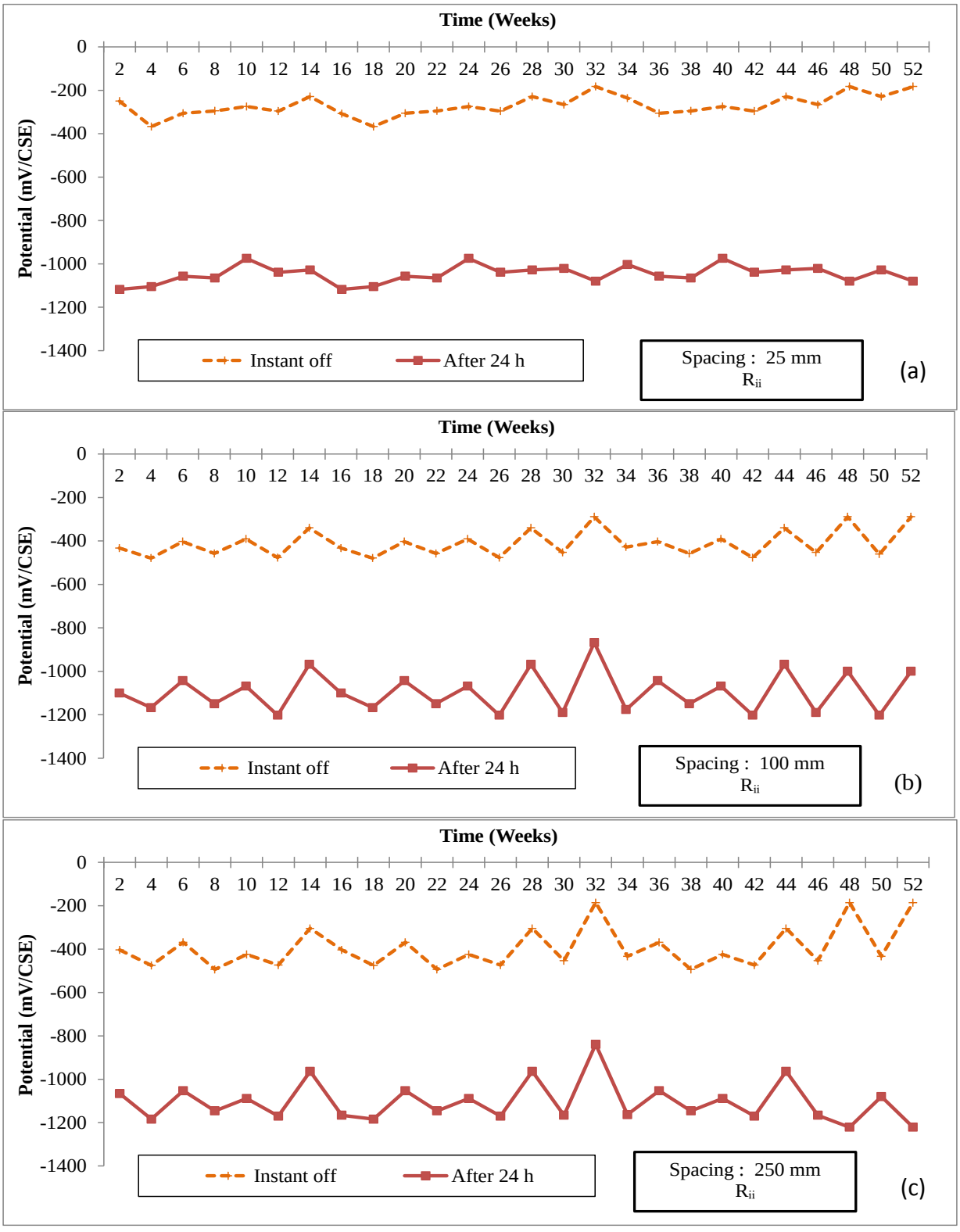

Figure 5.10: Potential distribution of steel in concrete during a depolarization test carried out for Rii slabs at different spacing: (a) 25 mm, (b) 100 mm, and (c) 250 mm.

Chapter 6 : Summary, Conclusions and Recommendations

6.1. Summary

In this thesis, two experimental studies were conducted. The first one aimed at establishing a tripartite relationship (nomogram) among the surface resistivity (SR), migration coefficient, and porosity of concrete. This facilitated the analysis of the second study, which aimed at exploring the effect of concrete resistivity on the efficiency of zinc anodes at mitigating patch accelerated corrosion (halo effect).

To establish the tripartite relationship, forty three concrete mixtures were prepared with various proportions of SCMs such as silica fume and fly ash (Class F) with or without the incorporation of different dosages of nanoparticles (6% nano-silica or nano-alumina) by mass of the total binder content at different w/b ranging from 0.3 to 0.7. The tests in this part of research included RCPT, SR, BR, and MIP. For evaluating the functionality of zinc anodes in repaired concrete, small-scale slabs were cast in three sections to simulate the patch repair configuration in the field. The bottom section was made of chloride free concrete, while the top section was split into two equal halves: one part (old concrete) contaminated with 3% calcium chloride by mass of cement, and the other part (repair patch-chloride free) had variable resistivity (between 5,000 and 100,000 Ω-cm). The assessment criteria were based on several electrical measurements such as the current density, potential, and 100-mv depolarization decay. The conclusions from both experimental parts are provided in the subsequent sections.

6.1.1. Conclusions of the tripartite relationship of resistivity, penetrability and porosity of concrete

Considering the materials, mixture designs and testing methods implemented in the present thesis, the following conclusions can be drawn:

- The overall results of resistivity (surface and bulk) and penetrability (migration coefficient and porosity) highlighted the role of key mixture design parameters (w/b and SCMs) in controlling the quality of concrete.
- A strong relationship between SR and BR (R^2 = 0.96) was obtained for a wide range of concrete mixture designs, which validates the notion that the BR of concrete can be predicted from its surface resistivity that better suits field applications.
- The efficacy of using the migration coefficient parameter from RCPT was substantiated. This parameter better correlates to the porosity of concrete (R^2 = 0.93) due to discounting electrolysis and joule effects from the results.
- A tripartite relationship (nomogram) among SR, migration coefficient and porosity of concrete was established, and an associated penetrability classification of concrete was proposed; hence, the relative condition and physical penetrability of concrete can be rapidly projected by means of a quick indicator such as SR.
- The efficacy of the nomogram and proposed classification was shown for field cores extracted from newly constructed and aging concrete pavement as the predicted penetrability classifications matched the ones projected by the experimental measurements. This application suggested that the tripartite relationship exists irrespective of the age of concrete, i.e. at any given SR range, there are corresponding

ranges of migration coefficient and porosity, from which the penetrability class of concrete can be obtained.

- Indeed, the tripartite relationship and penetrability classification developed herein are versatile and can be further improved/refined with the appearance of future data linking the electrical properties of concrete to its physical penetrability and microstructure.

6.1.2. Conclusions of the functionality of zinc anodes in repaired concrete

Considering the test-setup, resistivity of the repair sections, testing methods, and exposure period implemented in the current thesis, the following conclusions can be drawn:

- The results of resistivity of concrete conformed to the well-documented trends of the effects of w/b and SCMs. In addition to the effect of continual hydration with time, reduction of w/b from 0.5 to 0.3 and incorporation of 8% silica fume led to increasing the resistivity of the repair sections due densification of the pore structure, in addition to binding ionic species into the cementitious matrix in the case of silica fume. Moreover, the results of the high resistivity concrete tested herein (R_{iv}) highlight the predominant role of ultrafine pozzolans such as nano-silica in significantly refining and densifying the pore structure of the matrix.
- The slab configuration designed in the current study was capable of stimulating the incipient anode phenomenon (halo effect) as reflected by the differences in the average potentials between the repair and chloride contaminated sections, irrespective of the resistivity value of the repair section.
- The results showed that the total current density originating from the anode has been well distributed over the bars in all sections and remained above the acceptable level (0.2 to 2

mA/m^2) to prevent corrosion which alludes to the functionality of zinc anodes up to 52 weeks even in high resistivity concrete (up to 100,000 Ω-cm).

- The trends of the total current density to evaluate the influence of changing the location of the zinc anode diminished due to the convergence of currents at similar magnitudes, especially during the wetting cycles, except for the lowest resistivity class (R_i) as substantiated by the ANOVA results indicating that the effect of this parameter was statistically insignificant.
- Irrespective of the anode spacing, the results indicate that the slabs with anodes yielded more negative potential measurements in comparison to the corresponding slabs without anodes, as a result of the polarizing current flowing to the steel from the anodes.
- The results of the depolarization test (100 mV decay) showed that the steel bars had been cathodically polarized over the exposure period, irrespective of the location of the anodes inside the repair patch, as reflected by the considerable depolarization shifts after 24 h.

6.2. Recommendations for Future Work

The results and discussion presented in this thesis provide useful insights for the extension of this research work. The following are recommendations for further investigations:

- The nomogram relationships developed in this thesis can be further enhanced by increasing the population of concrete mixture designs, which may include other supplementary cementitious materials (e.g. metakaolin) and polymeric substances.
- The nomogram relationships can be further validated by testing field concrete from various structures in Winnipeg and elsewhere.

- The effect of normalizing the concrete resistivity measurements by the resistivity of the pore solution needs to be assessed to improve the nomogram relationships, if applicable.
- The time of exposure for the three-part slabs tested herein should be extended with continual monitoring of the currents and potentials to explore the effect of the variables tested on the functionality of zinc anodes over longer-term.
- The functionality of zinc anodes can be further assessed by studying the effect of other variables such as the addition of corrosion inhibitors into repair concrete and/or applying different coatings to reinforcement.

.

References

AASHTO TP 95 (2014). "Standard Method of Test for Surface Resistivity Indication of Concrete's Ability to Resist Chloride Ion Penetration." *American Association of State Highway and Transportation Officials*, Washington, DC.

ACI Committee E706, ACI RAP Bulletin-8 (2010). "Installation of Embedded Galvanic Anodes." *American Concrete Institute*, Farmington Hills, MI, 7 p.

Ahmad, S. (2014). "An Experimental Study on Correlation between Concrete Resistivity and Reinforcement Corrosion Rate." *Anti-Corrosion Methods and Materials*, 61(3), 158–165.

Andrade, C., and Alonso, C. (1996). "Corrosion Rate Monitoring in the Laboratory and on-Site." *Construction and Building Materials*, 10(5), 315–28.

Andrade, C., Prieto, M., Tanner, P., Tavares F., and Andrea, R. (2013). "Testing and Modelling Chloride Penetration into Concrete." *Construction and Building Materials*, 39, 9–18.

ASTM A370 (2014). "Standard Test Methods and Definitions for Mechanical Testing of Steel Products." *American Society for Testing and Materials*, ASTM International, West Conshohocken, PA, 1(1), 50.

ASTM C1202 (2012). "Standard Test Method for Electrical Indication of Concrete's Ability to Resist Chloride Ion Penetration." *Annual Book of ASTM Standards*, West Conshohocken, PA, USA.

ASTM C1543 (2010). "Standard Test Method for Determining the Penetration of Chloride Ion into Concrete by Ponding." *Annual Book of ASTM Standards*, West Conshohocken, PA, USA.

ASTM C1760 (2012). "Standard Test Method for Bulk Electrical Conductivity of Hardened Concrete." *Annual Book of ASTM Standards*, West Conshohocken, PA, USA.

ASTM C233 (2014). "Standard Test Method for Air-Entraining Admixtures for Concrete." *Annual Book of ASTM Standards*, West Conshohocken, PA, USA.

ASTM C260 (2010). "Standard Specification for Air-Entraining Admixtures for Concrete." *Annual Book of ASTM Standards,*, ASTM International, West Conshohocken, PA, USA.

ASTM C309 (2012). "Standard Specification for Liquid Membrane-Forming Compounds for Curing Concrete." *Annual Book of ASTM Standards,*, ASTM International, West Conshohocken, PA, USA.

ASTM C494 (2012). "Standard Specification for Chemical Admixtures for Concrete." *Annual Book of ASTM Standards*, West Conshohocken, PA, USA.

ASTM C876 (2009). "Standard Test Method for Corrosion Potentials of Uncoated Reinforcing Steel in Concrete." *Annual Book of ASTM Standards*, Philadelphia, Sec. 4, 4.02.

Bargaheiser, K., and Butalia, T. S. (2007). "Prevention of Corrosion in Concrete Using Fly Ash Concrete Mixes." *Concrete Technology Forum*, Dallas,Texas.

Barrett, T. J., Sun, H., and Weiss, W. J. (2013). "Performance of Portland Limestone Cements: Cements Designed to Be More Sustainable That Include up to 15% Limestone Addition." *Joint Transportation Research Program,* Indiana Department of Transportation and Purdue University, West Lafayette, Indiana, 2013.

Bassuoni, M. T., and Rahman, M. M. (2016). "Response of Concrete to Accelerated Physical Salt Attack Exposure." *Cement and Concrete Research*, 79, 395–408.

Bassuoni, M.T., Nehdi, M.L., and Greenough, T.R. (2006). "Enhancing the Reliability of Evaluating Chloride Ingress in Concrete Using the ASTM C 1202 Rapid Chloride Penetrability Test." *Journal of ASTM International*, 3(3), 13 p.

Belkowitz, J.S., Belkowitz, W. B., Nawrocki, K., and Fisher, F. T. (2014). "Impact of Nanosilica Size and Surface Area on Concrete Properties." *ACI Materials Journal,* 11(3), 419–428.

Bentur, A., Diamond, S., and Berke, N. S. (1997). "Steel Corrosion in Concrete: Fundamentals and Civil Engineering Practice.*"* E and FN Spon, London, UK.

Bertolini, L., Gastaldi, M., Pedeferri, M., and Redaelli, E. (2002). "Prevention of Steel Corrosion in Concrete Exposed to Seawater with Submerged Sacrificial Anodes." *Corrosion Science*, 44, 1497-1513.

Bertolini, L., Elsener, B., Pedeferri, P., and Polder, R. (2004). "Corrosion of Steel in Concrete: Prevention, Diagnosis, Repair." Wiley, Weinheim, Germany.

British Standards Institution, BS EN ISO: 12696 (2012). "Cathodic Protection of Steel in Concrete." BSI, London.

BS EN-12390 (2000). "Depth of Penetration of Water under Pressure." British Standards Institution.

Caldwell, R. J. (1998). "Effect of Supplementary Cementing Materials on the Specific Conductivity of Pore Solution and its Implications on the Rapid Chloride Permeability Test (AASHTO T277 and ASTM C1202) Results." *ACI Material Journal*, 95(4), 389–394.

CAN/CSA A23.1 (2014). "Concrete Materials and Methods of Concrete Construction." *Canadian Standards Association*, Mississauga, Ontario, Canada.

CAN/CSA-A3001 (2013). "Cementitious Materials for Use in Concrete, *Canadian Standards Association*." CSA, Mississauga, Ontario, Canada.

Cao, J., and Chung, D. D. L. (2004). "Electric Polarization and Depolarization in Cement-Based Materials, Studied by Apparent Electrical Resistance Measurement." *Cement and Concrete Research*, 34, 481–485.

Chini, A. R., Muszynski, L. C., and Hicks, J. (2003). "Determination of Acceptance Permeability Characteristics for Performance-Related Sepecifications for Portland Cement Concrete." *BC 354-41 Final Report*, Florida Department of Transportation, Tallahassee, FL, 165 p.

Christensen, B. J., Coverdale, R. T., Olson, R. A., Ford, S. J., Garboczi, E. J., Jennings, H. M. (1994). "Impedance Spectroscopy of Hydrating Cement Based Materials: Measurement, Interpretation, and Application." *Journal of American Ceramic Society*, 77(11), 2789–2804.

Christodoulou, C. C., Goodier, S., Austin, J., and Glass, G. K. (2013). "Diagnosing the Cause of Incipient Anodes in Repaired Reinforced Concrete Structures." *Corrosion Science*, 69, 123–129.

Chung DDL. (2003). "Damage in Cement-Based Materials Studied by electrical Resistance Measurement." *Measurement Science and Technology*, (42), 1–40.

CW 3310-R15 (2014). "Portland Cement Concrete Pavement Works." *Public Works Department, City of Winnipeg*, MB, Canada.

Du Plooy, R., Palma Lopes, S., Villain, G.,and Dérobert, X. (2013). "Development of a Multi-Ring Resistivity Cell and Multi-Electrode Resistivity Probe for Investigation of Cover Concrete Condition." *NDT and E International*, 54, 27–36.

Feldman, L. R. and Bartlett, F. M. (2007). "Bond Stresses along Plain Steel Reinforcing Bars in Pullout Specimens." *ACI Structural Journal*, 104(6), 685–692.

Ferreira, RM., Jalali, S. (2010). "NDT Measurements for the Prediction of 28-day Compressive Strength." *NDT and E International*, 43(2), 55–61.

FM 5-578 (2004). "Florida Method of Test for Concrete Resistivity as an Electrical Indicator of its Permeability." Florida Department of Transportation, Tallahassee, Florida, 1–4.

Frankel, G. S. (1998). "Pitting Corrosion of Metals. Journal of the Electrochemical Society." 145(6), 2186-2198.

Ghosh, P., and Tran, Q. (2015). "Influence of Parameters on Surface Resistivity of Concrete." *Cement and Concrete Composites*, 62, 134–145.

Ghosh, P., Tran, Q. (2014). "Correlation Between Bulk and Surface Resistivity of Concrete." *International Journal of Concrete Structures and Materials*, 9(1), 119–132.

Giorgini, R. (2014). "Issues Using Potential Decay Techniques to Assess a Cathodic Protection System of Steel in Concrete Caused by Macrocell Corrosion." *Concrete Solutions*, 189 -197.

González, J. a., Miranda JM., Feliu, S. (2004). "Considerations on Reproducibility of Potential and Corrosion Rate Measurements in Reinforced Concrete." *Corrosion Science*, 46, 2467–2485.

Gowers, K.R., and Millard, S.G. (1999). "Measurement of Concrete Resistivity for Assessment of Corrosion Severity of Steel Using Wenner Technique." *ACI Materials Journal*, 96(5), 536-541.

Hansson, C. M., Poursaee, A., and Laurent, A. (2006). "Macrocell and Microcell Corrosion of Steel in Ordinary Portland Cement and High Performance Concretes." *Cement and Concrete Research*, 36(11), 2098–2102.

Hornbostel K., Larsen CK., and Geiker MR. (2013). "Relationship Between Concrete Resistivity and Corrosion Rate – A Literature Review." *Cement and Concrete Composite*, 39, 60–72.

Lataste, J. (2010) "Electrical resistivity for the evaluation of reinforced concrete structures" In: Maierhofer C, Reinhardt H-W and Dobmann G, editors, Non-Destructive Evaluation of Reinforced Concrete Structures, Woodhead Publishing Series in Civil and Structural Engineering, 2, 243-275.

Layssi, H., Ghods, P., Alizadeh, R., and Salehi, M. (2015). "Electrical Resistivity of Concrete." *Concrete International*, 37(5), 41-46.

Liu, Y., Francisco, P., and Mario, P. (2015). "Determination of Chloride Diffusion Coefficients in Concrete by Electrical Resistivity Method." *ACI Material Journal*, 112(5), 631–640.

Mehta, P. K., and Monteiro, P. J. M. (2014). "Concrete: Structure, Properties, and Materials, Fourth Edition." Prentice Hall, Englewoods Cliffs, NJ.

Montgomery, D. (2012). "Design and Analysis of Experiments." Eighth Edition, John Wiley and Sons, Hoboken, NJ, USA.

Morris, W., Moreno, E. I., and Sagüés, A. A. (1996). "Practical Evaluation of Resistivity of Concrete in Test Cylinders Using a Wenner Array Probe." *Cement and Concrete Research*, 26(12), 1779–1787.

NACE SP0290 (2007). "Impressed Current Cathodic Protection of Reinforcing Steel in Atmospherically Exposed Concrete Structures." *NACE International*, Houston, TX.

Neville, A. (1995)., "Chloride Attack of Reinforced Concrete: an Overview." *Materials and Structures*, 28(2), 63–70.

NT BUILD 492 (1999). "Chloride Migration Coefficient from Nonsteady-State Migration Experiments." *NORDTEST*, Finland.

Oladis T. de Rincdn, Matilde F. de Romero, Aleida R. de Carruyo, Miguel Sdnchez, and Josd Bravo (1997). "Performance of Sacrificial Anodes to Protect the Splash Zone of Concrete Piles." *Materials and structures*, 30, 556-560.

Otieno, M. B., Alexander, M. G., and Beushausen, H. D., (2010). "Suitability of Various Measurement Techniques for Assessing Corrosion in Cracked Concrete." *ACI Materials Journal*, 107(5), 481–489.

Page, C. L., and Sergi, G. (2000). "Development in Cathodic Protection Applied to Reinforced Concrete." *Journal of Materials in Civil Engineering*, 12 (1), 8–15.

Page, C. L., and Treadaway, K.W.J. (1982). "Aspects of the Electrochemistry of Steel in Concrete." *Nature*, 297, 109–115.

Pedeferri, P. (1996). "Cathodic Protection and Cathodic Prevention." *Construction and Building Materials*, 10(5), 391–402.

Polder, R. (2001). "Test methods for on-site measurement of resistivity of concrete—A RILEM TC-154 technical recommendation." *Construction and Building Materials*, 15(3), 125–131.

Ramey, G., Pittman, D. W., Greg, W., and Carden, A. (1997). "Use of Shrinkage Compensating Cement in Bridge Decks." *Final Report on Highway Research Center Research Project,* Department of Civil Engineering, Auburn University.

Ramezanianpour, A. A., Pilvar, A., Mahdikhani, M., and Moodi, F. (2011). "Practical Evaluation of Relationship between Concrete Resistivity, Water Penetration, Rapid Chloride Penetration and Compressive Strength." *Construction and Building Materials*, 25(5), 2472–2479.

Ramezanianpour, A. M., and Hooton, R. D. (2014). "A Study on Hydration, Compressive Strength, and Porosity of Portland-limestone Cement Mixes Containing SCMs." *Cement and Concrete Composite,* 51, 1–13.

Riding, K. A., Poole, J. L., Schindler, A. K., Juenger, M. C. G., and Folliard, K. J. (2008). "Simplified Concrete Resistivity and Rapid Chloride Permeability Test Method." *ACI Material Journal*, 105, 390–394.

Ryan, E., Burdette, E., Ankabrandt, R., Nidiffer, R., and Buchanan, B. (2014). "Comparison of Two Methods to Assess the Resistance of Concrete to Chloride ion Penetration." *Journal of Materials in Civil Engineering*, 26(4), 698–704.

Sagüés, A.A., and Powers, R.G. (1994). "Sprayed Zinc Galvanic Anodes for Concrete Marine Bridge Substructures." *National Research Council*, Washington DC, SHRP-S-405.

Savas, B. Z. (1999). "Effects of Microstructure on Durability of Concrete." Raleigh, NC: North Carolina State University Department of Civil Engineering.

Sengul O., Gjørv OE. (2009). "Effect of Embedded Steel on Electrical Resistivity Measurements on Concrete Structures." *ACI Material Journal*, 106(1), 11–18.

Sengul, O. (2014). "Use of Electrical Resistivity as an Indicator for Durability." *Construction and Building Materials*, 73, 434–441.

Sergi, G. (2011). "Ten-year Results of Galvanic Sacrificial Anodes in Steel Reinforced Concrete." Materials and Corrosion, 61(2), 98-104.

Spragg, R.P., Castro, J., Nantung, T., Paredes, M., and Weiss, J. (2012). "Variability Analysis of the Bulk Resistivity Measured Using Concrete Cylinders." Advances in Civil Engineering Materials, 1(1), 1–17.

Stanish, K., Hooton, R.D., and Thomas, M.D.A. (2000). "Evaluation of Four Short-Term Methods for Determining Chloride Penetrability in Concrete." in: M.S. Khan (Ed.), ACI SP-191, Water –Cement Ratio and Other Durability Parameters—Techniques for Determination, ACI, Farmington Hills, MI, 2000, 191, 81-98.

Stanish, K.D., Hooton, R.D., and Thomas, M.D.A. (1997). "Testing the Chloride Penetration Resistance of Concrete: A Literature Review." (FHWA Contract DTFH61-97-R-00022: Prediction of Chloride Penetration in Concrete). Toronto, ON, Canada: University of Toronto Department of Civil Engineering.

Steen, B., Wuytens, B., Vervoort, a., Gemert, D. (1998). "Evaluation of Mineral Building Materials: Problems Related to Resistivity Methods." *Materials and Structures*, 31, 126–132.

Tennis, P. D., Thomas, M. D. A., and Weiss, W. J. (2011). "State-of-the-Art Report on Use of Limestone in Cements at Levels of up to 15%." Skokie, Illinois, USA: Portland Cement Association, 74 p.

Voglis, N., Kakali, G., Chaniotakis, E., and Tsivilis, S. (2005). "Portland-Limestone Cements. Their Properties and Hydration Compared to Those of Other Composite Cements." *Cement and Concrete Composite,* 27, 191–96.

Wanga Z., Zeng Q., Wanga L., Yao Y., and Li, K. (2013). "Characterizing Blended Cement Pastes under Cyclic Freeze–Thaw Actions by Electrical Resistivity." *Construction and Building Materials, (*44), 477–86.

Wee, T. H., Suryavanshi, A. K., and Tin, S. S. (2000). "Evaluation of Rapid Chloride Permeability Test (RCPT) Results for Concrete Containing Mineral Admixtures." *ACI Material Journal*,. 97(2), 221–232.

Whiting DA., and Nagi, MA. (2003). "Electrical Resistivity of Concrete – A Literature Review." Skokie (Illinois), Portland Cemente Association.

Whitmore, D., and Abbott, S. (2003). "Embedded Galvanic Anodes Increase Sustainability of Reinforced Concrete Structures." *Annual Conference of the Transportation Association of Canada*, St. John's, Newfoundland and Labrador, 10 p.

Whitmore, D. Ball, C. (2005). "Galvanic Protection for Reinforced Concrete Structures." *Concrete Repair Bulletin*, International Concrete Repair Institute, 4 p.

Whitmore, D. Ball, C. (2009). "Embedded Galvanic Anodes For Targeted Protection In Reinforced Concrete Structures." *Concrete Repair Bulletin*, International Concrete Repair Institute, Coffs Harbour, AU, 8 p.

Wong, H. S., Pappas, A. M., Zimmerman, R. W., and Buenfeld, N., R. (2011). "Effect of Entrained Air Voids on the Microstructure and Mass Transport Properties of Concrete." *Cement and Concrete Research*, 41(10), 1067–77.

Zaccardi, Villagran Y.A., Fullea, Garcia, Huelamo, P. A.A., Maio Di. (2009). "Influence of Temperature and Humidity on Portland Cement Mortar Resistivity Monitored with Inner Sensors." *Materials and Corrosion*, 60, 294–299.

Zhao, T., Zhou, Z., Zhu, J., and Feng N. (1998). "An Alternating Test Method for Concrete Permeability." *Cement and Conrete Research.*, 28(1), 7–12.

Appendix A : Change in the Current

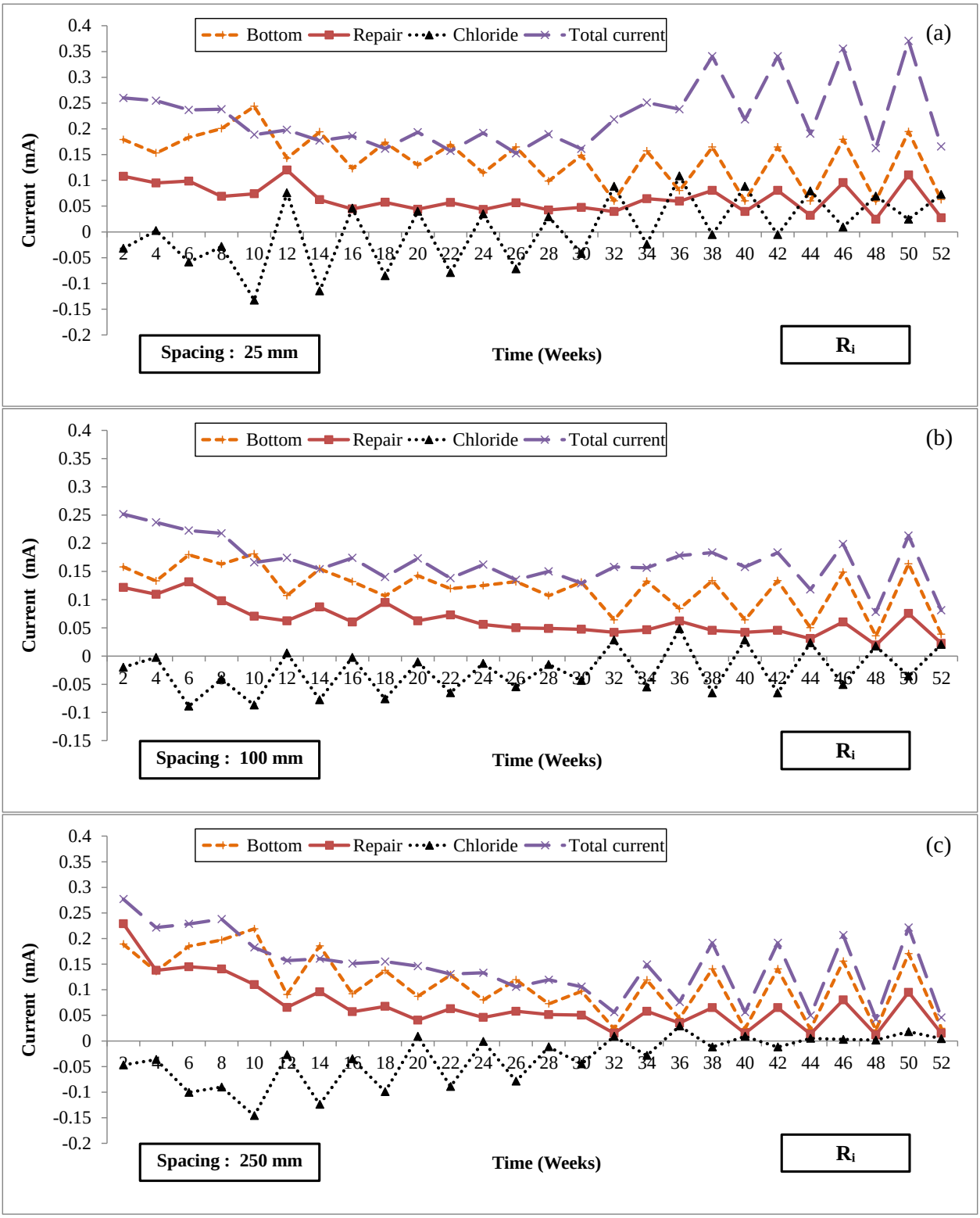

Figure A.1: Change in the current over time in the three sections of concrete slabs and the total current from the zinc anodes for R_i slab at a spacing of: (a) 25 mm (b) 100 mm, and 250 mm.

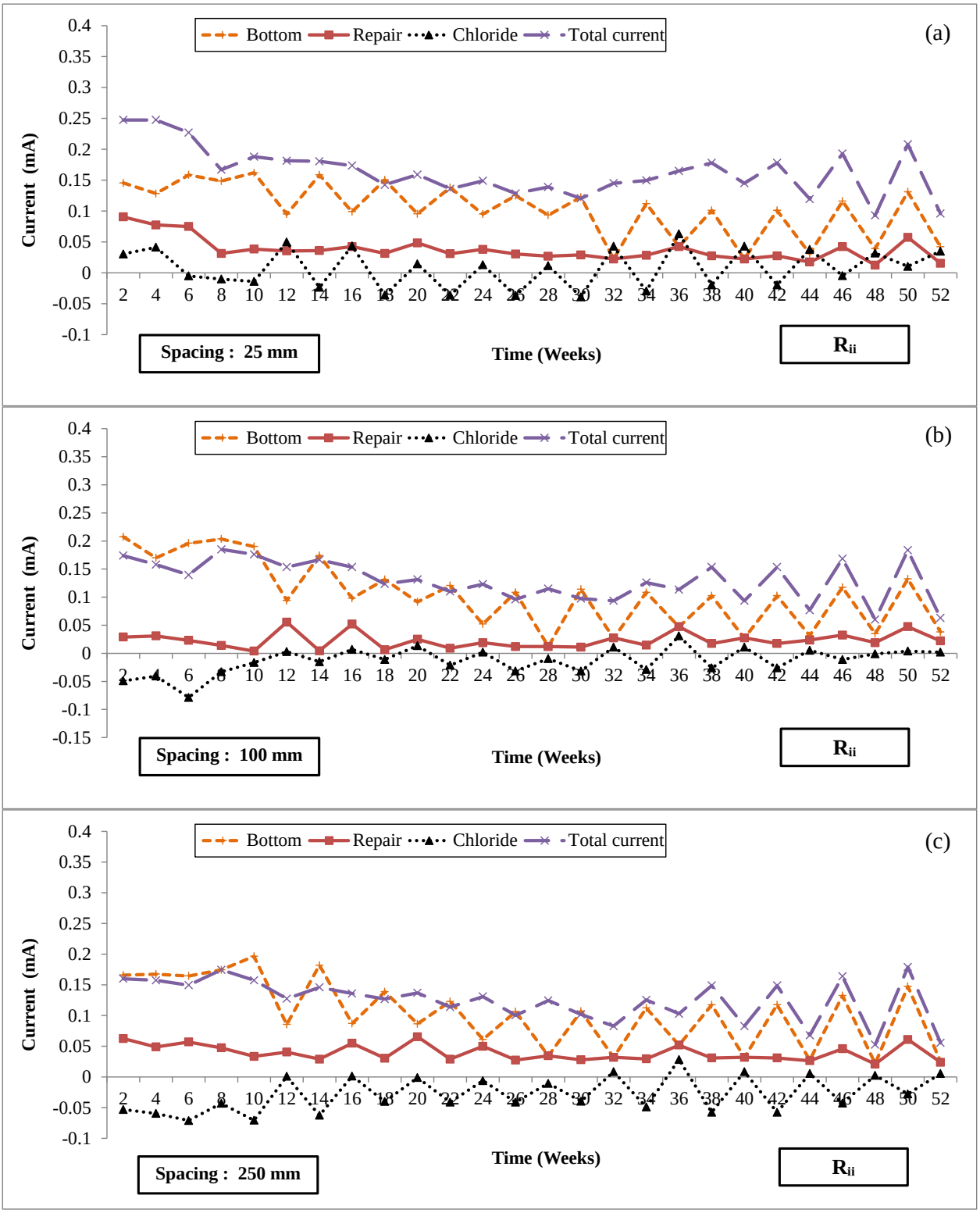

Figure A.2: Change in the current over time in the three sections of concrete slabs and the total current from the zinc anodes for R_{ii} slab at a spacing of: (a) 25 mm (b) 100 mm, and 250 mm.

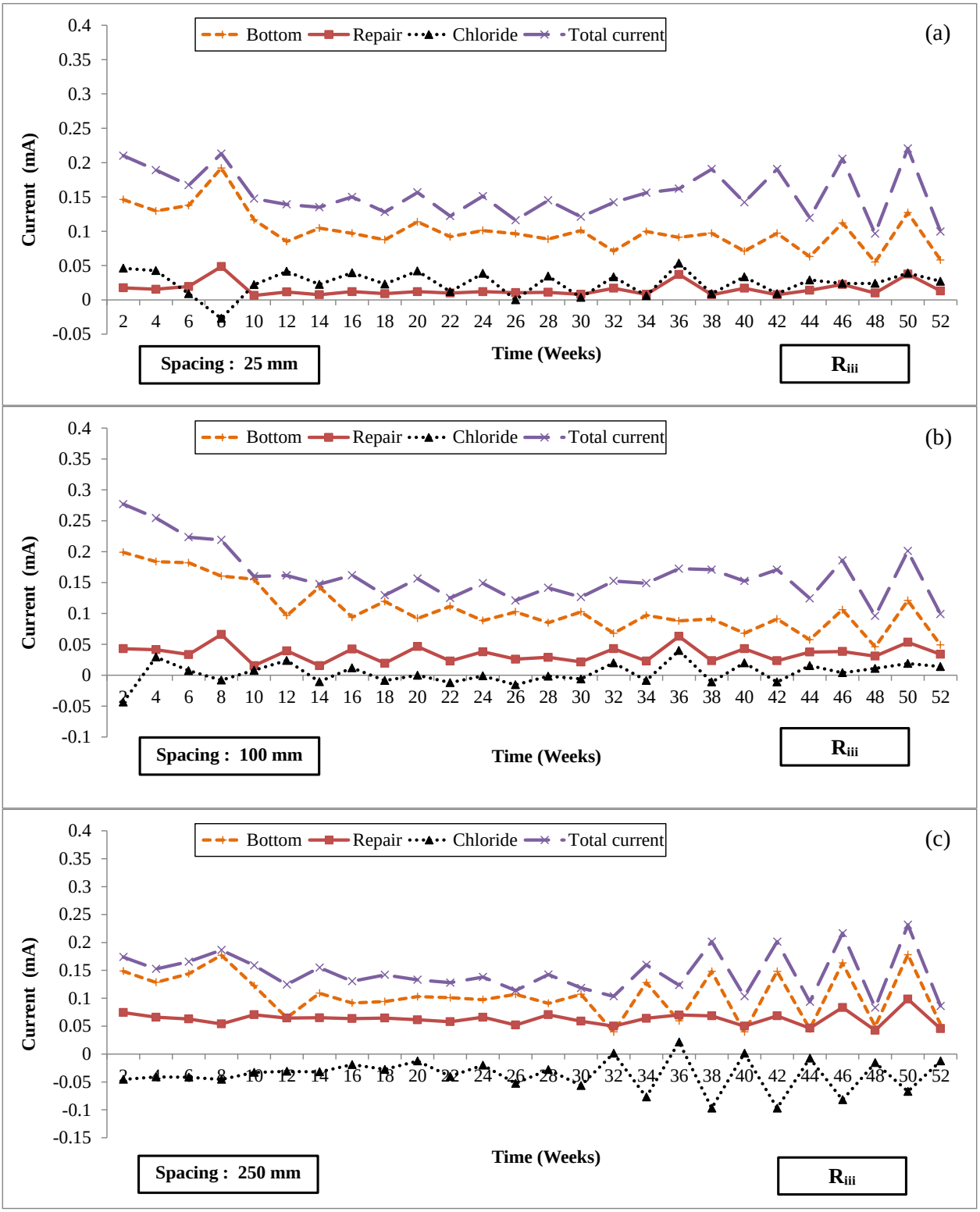

Figure A.3: Change in the current over time in the three sections of concrete slabs and the total current from the zinc anodes for R_{iii} slab at a spacing of: (a) 25 mm (b) 100 mm, and 250 mm.

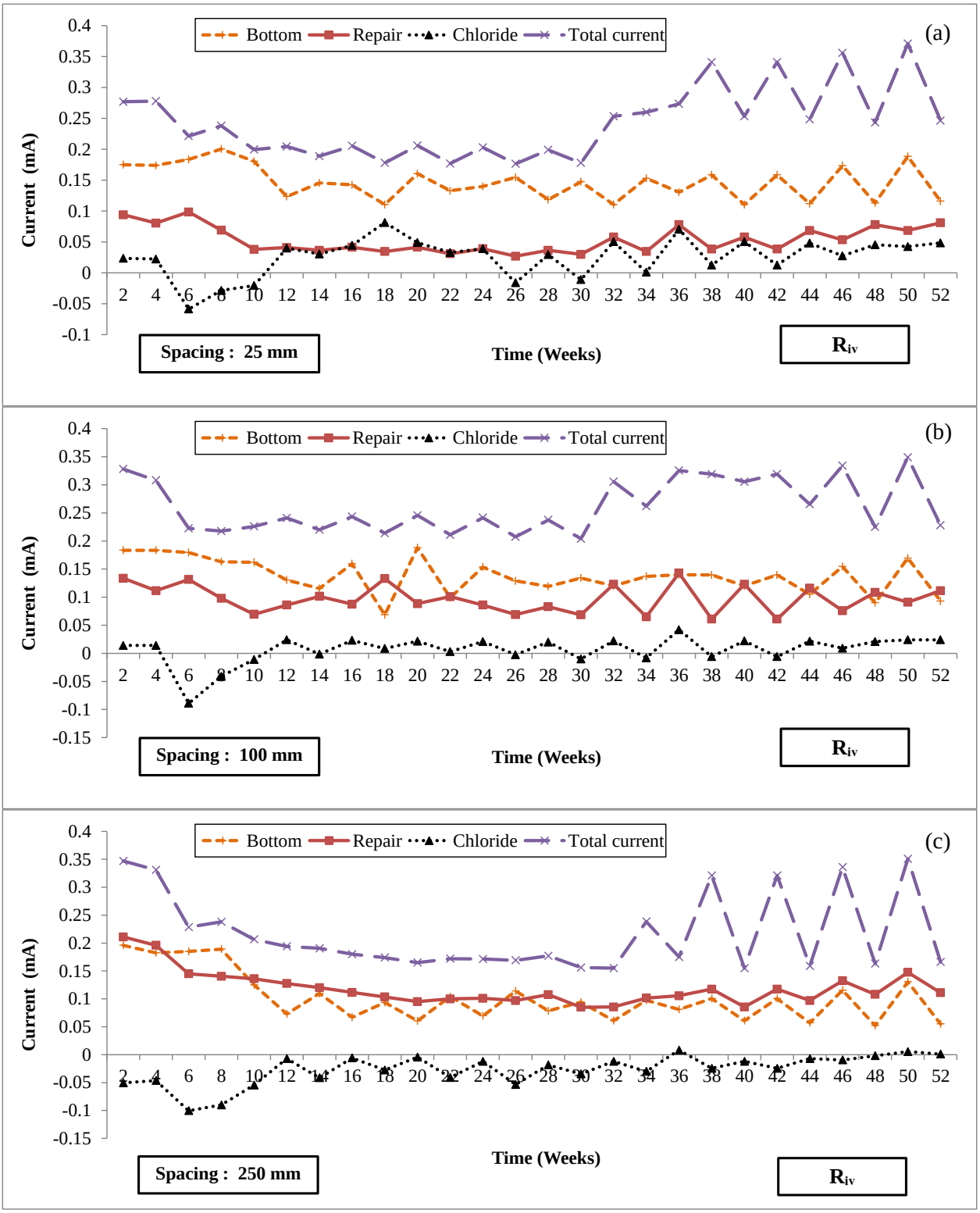

Figure A.4: Change in the current over time in the three sections of concrete slabs and the total current from the zinc anodes for R_{iv} slab at a spacing of: (a) 25 mm (b) 100 mm, and 250 mm.

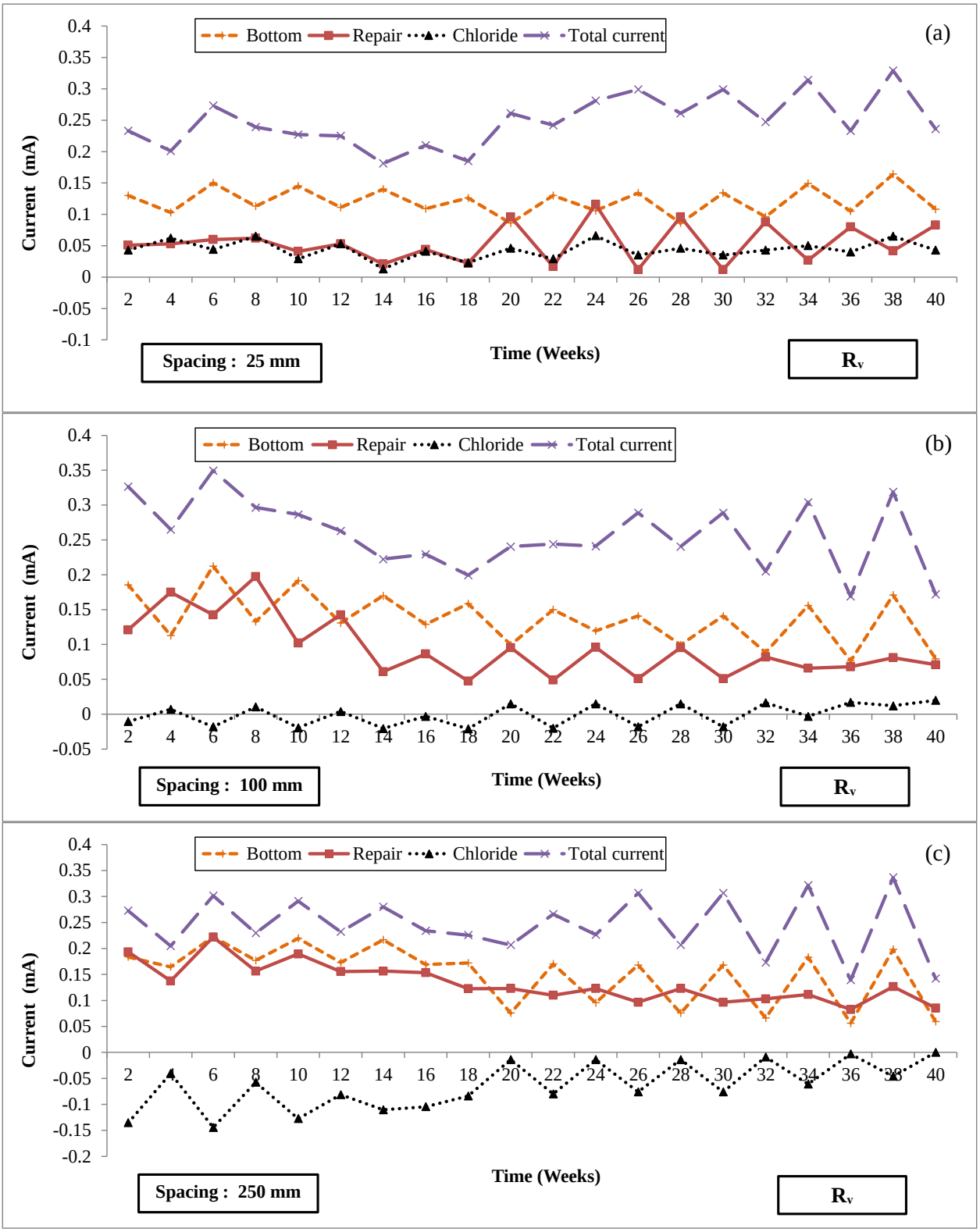

Figure A.5: Change in the current over time in the three sections of concrete slabs and the total current from the zinc anodes for R_v slab at a spacing of: (a) 25 mm (b) 100 mm, and 250 mm.

Appendix B : 100 mV Depolarization Decay

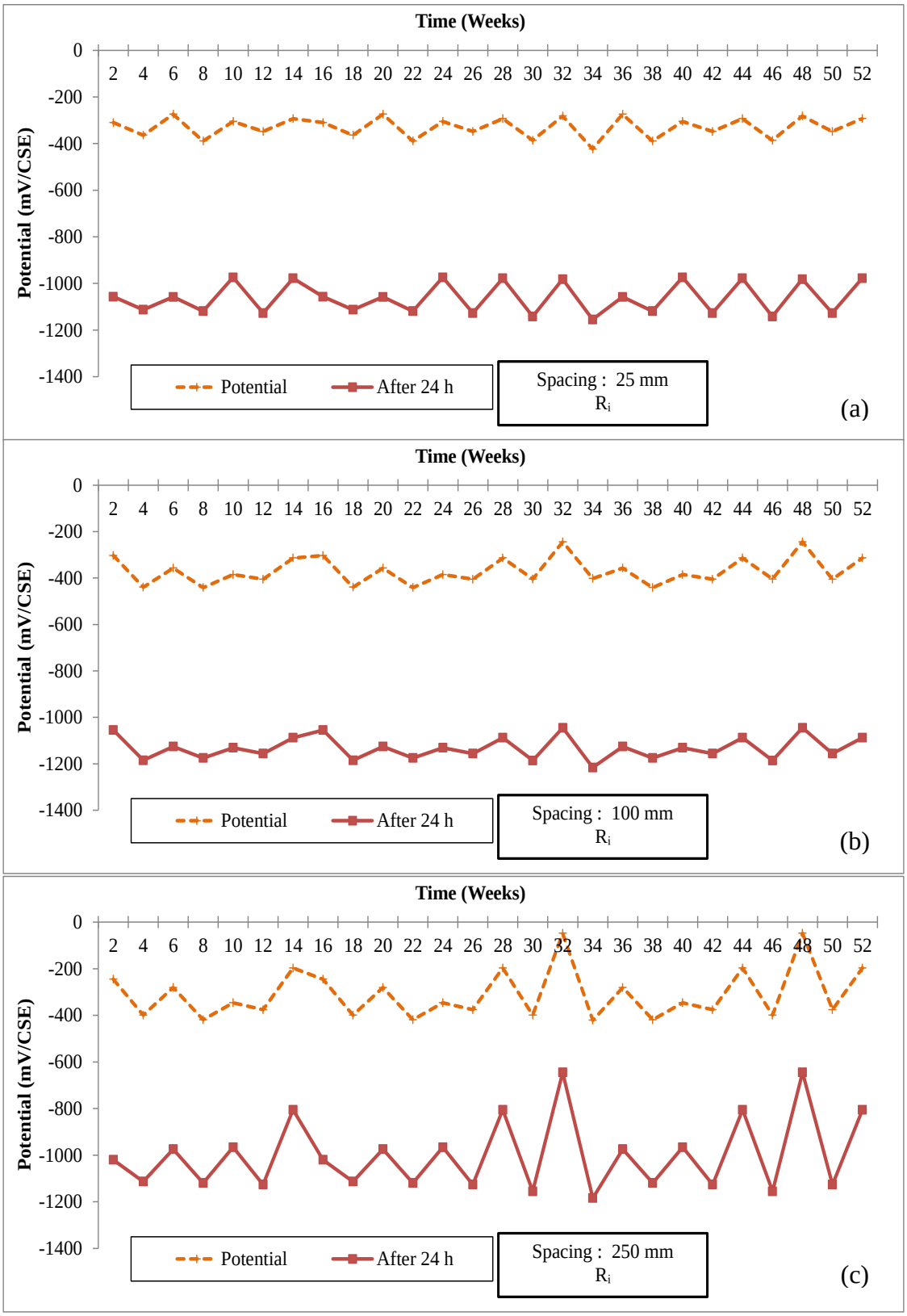

Figure B.1: Potential distribution of steel in concrete during a depolarization test carried out for R_i slabs at different spacing: (a) 25 mm, (b) 100 mm, and (c) 250 mm.

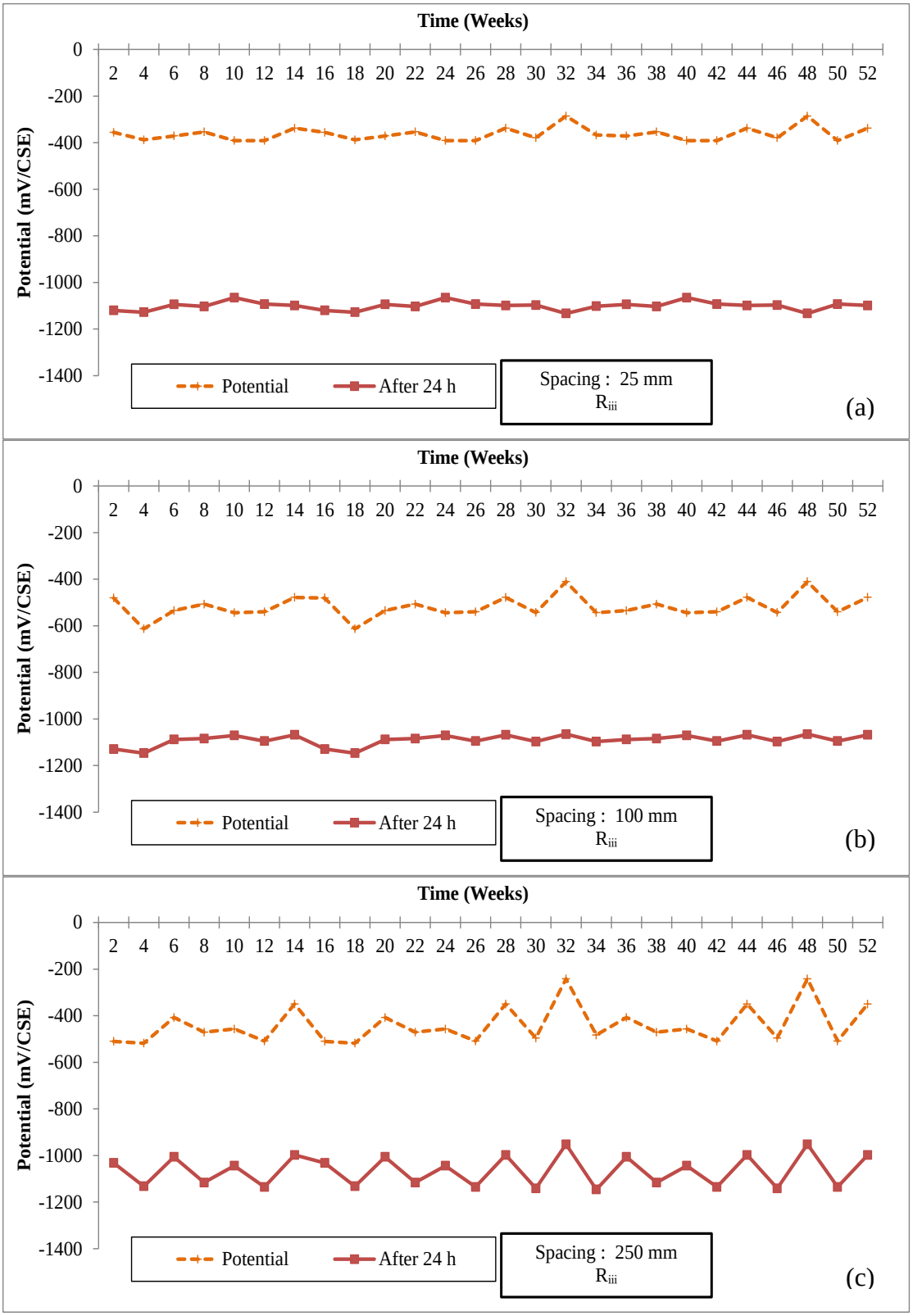

Figure B.2: Potential distribution of steel in concrete during a depolarization test carried out for R_{iii} slabs at different spacing: (a) 25 mm, (b) 100 mm, and (c) 250 mm.

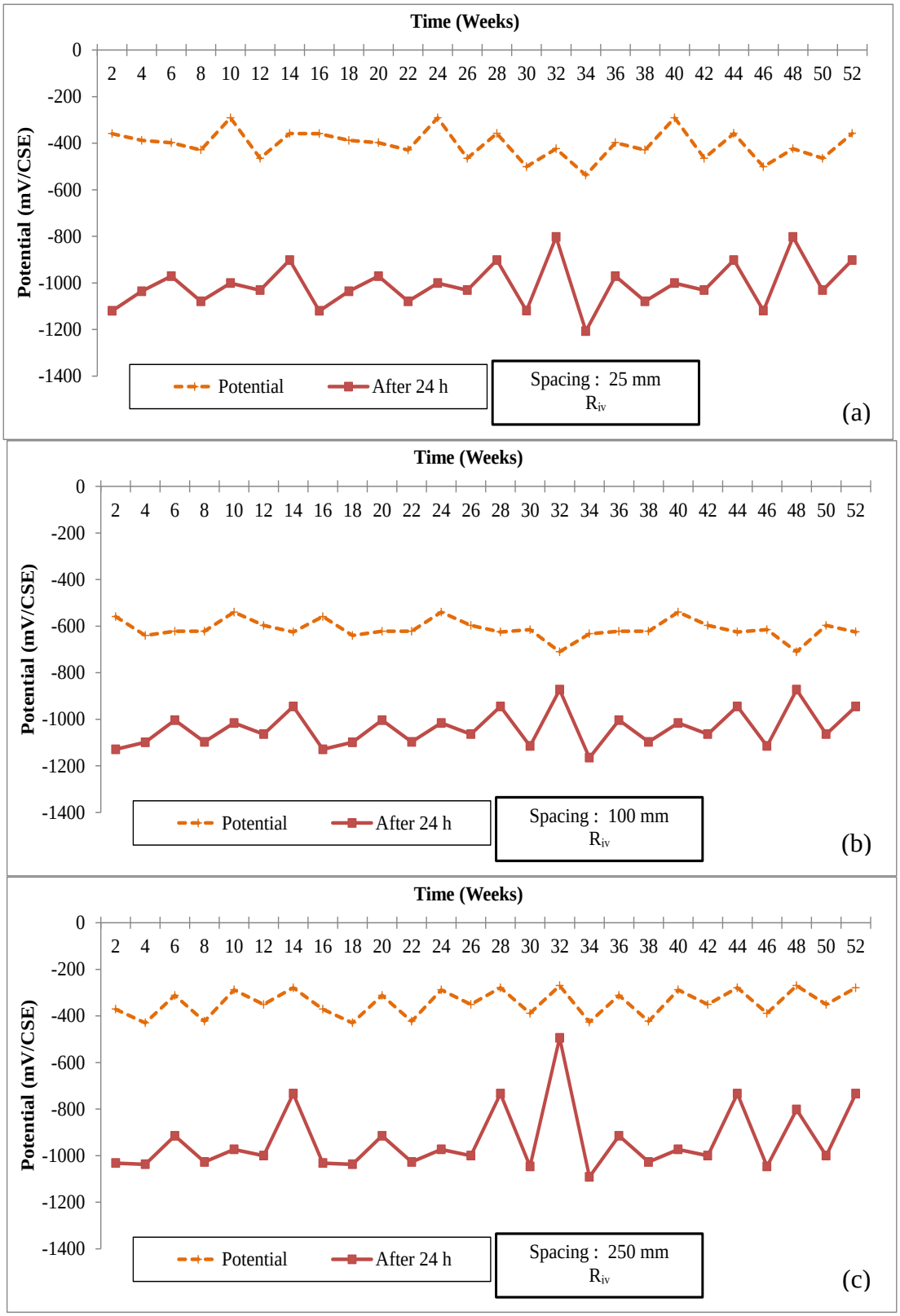

Figure B.3: Potential distribution of steel in concrete during a depolarization test carried out for R_{iv} slabs at different spacing: (a) 25 mm, (b) 100 mm, and (c) 250 mm.

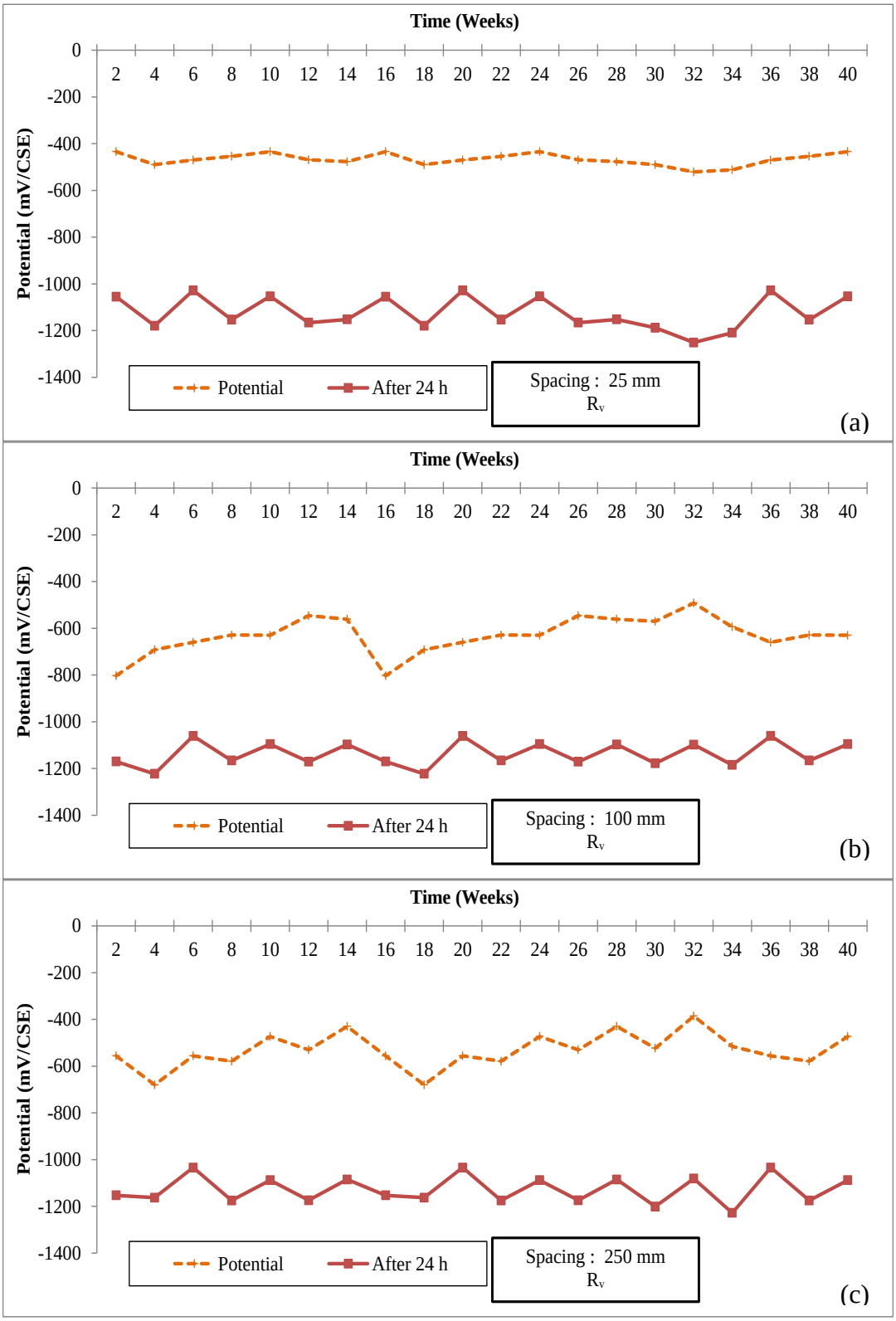

Figure B.4: Potential distribution of steel in concrete during a depolarization test carried out for R_v slabs at different spacing: (a) 25 mm, (b) 100 mm, and (c) 250 mm.